Technische Universität München
Fakultät für Physik

Abschlussarbeit im Masterstudiengang Physik

Characterization of the Particle Identification of the Belle II Detector with Bhabha Radiation and First Measurement of $\sin(2\phi_1)$ and Δm_d Using Belle II Data

Justin Skorupa

01. February 2021

Max-Planck-Institut für Physik

Erstgutachter (Themensteller): Prof. A. Caldwell
Zweitgutachter: Dr. B. Grube

Contents

Chapter 1

Introduction

The Standard Model of Particle Physics (SM) describes the elementary particles and their interactions. The elementary particles are pointlike and contain no substructure. The observed matter in the universe consists of fermions (spin 1/2 particles) which are divided into two groups: quarks and leptons. Quarks carry color and electroweak charge. They are categorized as up and down-type quark according to their electric charge of 2/3 and $-1/3$, respectively. Leptons only carry electroweak charge. Charged leptons (e^-, μ^- and τ^-) have an electric charge of -1 and neutral leptons (ν_e, ν_μ and ν_τ) have an electric charge of 0. Leptons and quarks are divided into three generations. The particles in each generation have the same spin and electric charge as their counterparts in the other generations, but different masses and lifetimes. Three (strong, electromagnetic and weak) of the four known forces in the universes are described by the SM (gravity being the fourth). In the SM, interactions between charged particles are described via exchange of gauge bosons (spin 1 particles). The strong forces is mediated by color charged gluons, the electromagnetic force by photons and the weak force by $W^\pm$, Z^0 bosons [3], [4]. The final elementary particle in the SM is the Higgs boson. The existence of the Higgs boson is implied by the Higgs mechanism that generates the mass of the elementary particles. In Fig. 1.1 the particle content of the SM is shown. Each of the different types of quarks has an associated flavor quantum number (up, down, charm, strange, top, bottom). This quantum number is conserved by the electromagnetic and strong force but violated by the weak force. Up- and down-type quarks can be transformed into each other via the exchange of $W^\pm$ bosons [5]. The coupling strength of $W^\pm$ bosons to pairs of up- and down-type quarks is described by the Cabibbo–Kobayashi–Maskawa matrix (CKM matrix). The CKM matrix V_{CKM} is a unitary matrix that relates the quark mass and flavor eigenstates

$$\begin{bmatrix} d' \\ s' \\ b' \end{bmatrix} = V_{\mathrm{CKM}} \begin{bmatrix} d \\ s \\ b \end{bmatrix}, \tag{1.1}$$

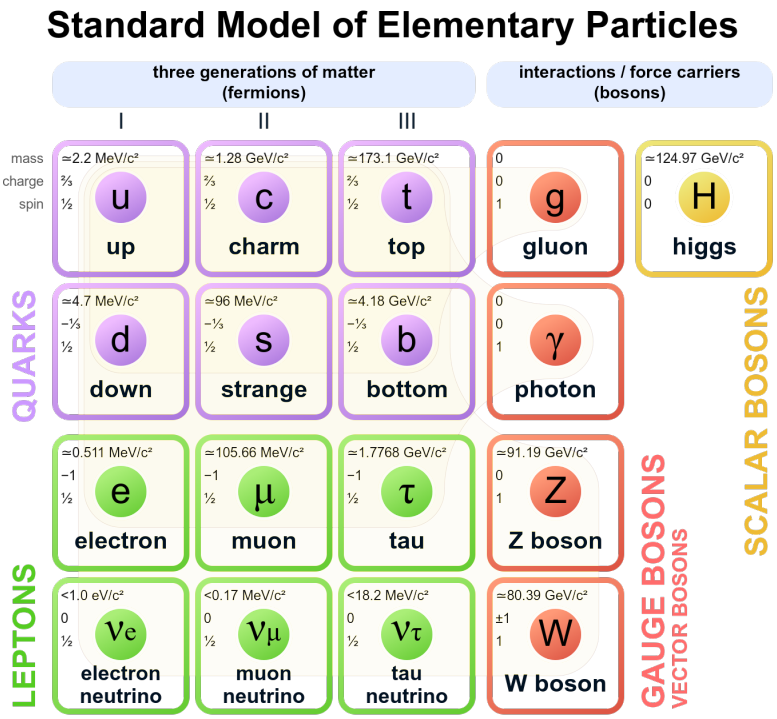

Figure 1.1: The Standard Model of Particle Physics [1]. The fermions are depicted in purple (quarks) and green (leptons). The force carriers are shown in red (gauge bosons) and yellow (higgs boson). The brown background indicates which fermion interacts with which gauge boson. To the left of each particle, the mass, charge and spin of the particle are displayed.

where the (un)primed d, s and b denote the quark flavor (mass) eigenstates. It is commonly parameterized as

$$\begin{aligned} V_{\mathrm{CKM}} &= \begin{bmatrix} V_{ud} & V_{us} & V_{ub} \\ V_{cd} & V_{cs} & V_{cb} \\ V_{td} & V_{ts} & V_{tb} \end{bmatrix} \\ &= \begin{bmatrix} c_{12}c_{13} & s_{12}c_{13} & s_{13}e^{-\mathrm{i}\delta} \\ -s_{12}c_{23} - c_{12}s_{23}s_{13}e^{\mathrm{i}\delta} & c_{12}c_{23} - s_{12}s_{23}s_{13}e^{\mathrm{i}\delta} & s_{23}c_{13} \\ s_{12}s_{23} - c_{12}c_{23}s_{13}e^{\mathrm{i}\delta} & -c_{12}s_{23} - s_{12}c_{23}s_{13}e^{\mathrm{i}\delta} & c_{23}c_{13} \end{bmatrix}, \end{aligned} \tag{1.2}$$

where $c_{ij} = \cos(\theta_{ij})$, $s_{ij} = \sin(\theta_{ij})$, the mixing angles θ_{12}, θ_{23} and θ_{13} describe the mixing between different generations of quarks and the complex phase δ describes CP violation [6], [7]. Historically, the development of the CKM matrix in 1973 was

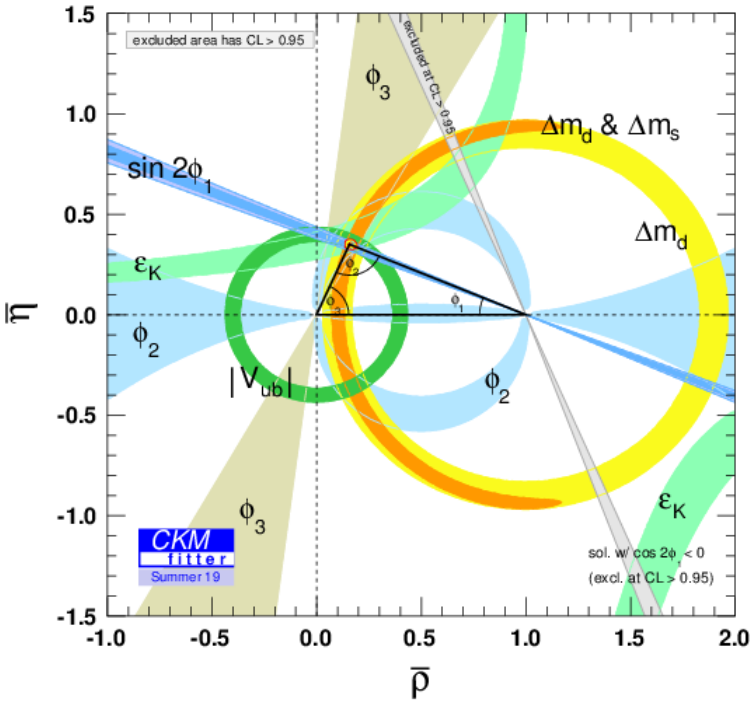

Figure 1.2: The CKM triangle [2].

a major achievement for particle physics since it extended the 2×2 Cabbibo matrix [8] to a 3×3 matrix and consequently proposed a third yet undiscovered quark generation. This extension of the Cabbibo matrix was necessary to explain the CP violation observed by Cronin and Fitch in the system of neutral Kaons in 1964 [9]. In the SM, CP violation arises from the complex phase δ in the CKM matrix. In a model with two quark generations, no CP violation exists since a phase convention can be chosen in which the complex phase δ is zero [10]. Several different parametrizations of the CKM matrix exist. One commonly used is the Wolfenstein parameterization that exploits the hierarchy of the CKM matrix by expanding it in terms of $\lambda = s_{12}$ [11]. The CKM matrix in the Wolfenstein parametrizations is

$$V_{\mathrm{CKM}} = \begin{bmatrix} 1 - \frac{1}{2}\lambda^2 & \lambda & A\lambda^3(\rho - i\eta) \\ -\lambda & 1 - \frac{1}{2}\lambda^2 & A\lambda^2 \\ A\lambda^3(1 - \rho - i\eta) & -A\lambda^2 & 1 \end{bmatrix} + O(\lambda^4), \tag{1.3}$$

where $A\lambda^2 = s_{23}$ and $A\lambda^3(\rho + \mathrm{i}\eta) = s_{13}e^{\mathrm{i}\delta}$. Using the unitarity condition of the CKM matrix $\Sigma_i V_{ij} V_{ik}^* + \delta_{jk}$, the Wolfenstein parameterization allows to construct so called

unitarity triangles in the $\eta - \rho$ plane [7]. The length of the sides of these triangles are related to the magnitude of the different CKM matrix elements and the angles are related to the CP violation in the decay of quarks and anti-quarks. Therefore measurement of the different sides and angles allows to constrain the CKM matrix. The system of B-mesons is particularly interesting for CP violation measurements because a sizable CP violation is expected in the bottom sector [12]. This can be shown vividly using the unitarity triangles. The unitarity triangle related to the decay of B-mesons is constructed by taking

$$V_{ud}V_{ub}^* + V_{cd}V_{cb}^* + V_{td}V_{tb}^* = 0 \tag{1.4}$$

from the unitarity condition and dividing each side by $V_{cd}V_{cb}^*$. The triangle is shown in Fig. 1.2. Of particular interest for this thesis are the parameters $\sin(2\phi_1)$ and Δm_d, which constrain the upper half of the triangle. All sides of this triangles are of order $\mathcal{O}(\lambda^3)$, leading to large angles corresponding to large CP violation. In contrast, the triangle related to the decay of neutral Kaons,

$$V_{ud}V_{us}^* + V_{cd}V_{cs}^* + V_{td}V_{ts}^* = 0, \tag{1.5}$$

has two sides of order $\mathcal{O}(\lambda)$ and one side of order $\mathcal{O}(\lambda^5)$. This results in a very elongated triangle with a short side and small angles corresponding to small CP violation. Therefore it is easier to measure CP violation in the system of neutral B-mesons than neutral Kaons.

Although CP violation observed in the quark sector is explained within the SM, it is not enough to explain the matter-antimatter asymmetry in the universe. In addition, other observed phenomena like dark matter are also not explained. This indicates clearly the existence of physics beyond the SM. Two concurrent accelerator approaches exist to search for such physics. Firstly, direct searches, in which particles are collided at high center-of-mass energy to create and measure new, yet undiscovered particles. Secondly, indirect search, where parameters of the SM are measured with high precision to look for deviations from the theory expectation. B-flavor factories belong to the latter. A key component of the physics program of B-flavor factories that determines their design is the precision measurement of the parameters of the CKM matrix. To perform these measurements, asymmetric electron-positron beams are collided at the $\Upsilon(4S)$ resonance at B-flavor factories. This setup provides entangled B-$\overline{\mathrm{B}}$ meson pairs in a clean environment. Due to the asymmetric beam energies, the B-mesons are not produced at rest. This enables the measurement of time-dependent quantities, since a decay time difference between the B-mesons leads to a different decay vertex position in the beam boost direction. The environment of B-flavor factories also allows to perform precision measurements of other quantities than the CKM matrix parameters. For example, B-flavor factories are also τ factories since the production cross section of τ-pairs at the energy

of the $\Upsilon(4S)$ resonance is of the same order as the production cross section of B-$\overline{\text{B}}$ meson pairs. This allows to perform precision measurements of τ decays and search for example for CP violation in τ decays and lepton flavor violation [13]. The first generation B-flavor factories, BaBar and Belle [14], [15], discovered CP violation in the system of neutral B-mesons confirming the CKM matrix and provided precision measurements of various SM parameter. BaBar stopped taking data in 2008 and Belle in 2010. In 2018, the Belle II experiment began recording collision data. As a next-generation B-flavor factory, it is the successor of BaBar and Belle. Compared to Belle, Belle II is designed to accumulate a 50 times larger dataset corresponding to an integrated luminosity of 50 ab^{-1} [16], [17]. This will allow to measure SM parameters with even higher precision and find possible hints for physics beyond the SM.

The remainder of this thesis is structured as follows. In Chapter 2, the detector and the accelerator of the Belle II experiment is introduced in detail. To demonstrate that Belle II performs adequately and is well understood, an analysis of the electron identification efficiency of the detector is presented in Chapter 3. Finally, a first measurement of $\sin(2\phi_1)$ and Δm_d using the Belle II data is presented in Chapter 4. In Chapter 5, the results of this thesis are summarized .

Chapter 2

The Belle II Experiment

The SuperKEKB accelerator at the High Energy Accelerator Research Organization in Tsukuba (Japan) is a next generation flavor factory. The Belle II experiment is located at the Interaction Point (IP) of the accelerator. The search for new physics in the flavor sector is the primary focus of the Belle II experiment. In addition, it aims to improve the precision of measurements of the Standard Model parameters [17]. To achieve this objective, the KEKB accelerator was upgraded to the SuperKEKB accelerator to provide an instantaneous luminosity of $8 \cdot 10^{35}$ $\mathrm{cm}^{-2}\mathrm{s}^{-1}$. The Belle detector was also upgraded to the Belle II detector to deal with the challenges arising from such high luminosity. In this chapter an introduction to the SuperKEKB accelerator and the Belle II detector based on the *Belle II Physics Book* [17] and the *Belle II Technical Design Report* [18] is given.

2.1 The SuperKEKB Accelerator

The SuperKEKB accelerator is an asymmetric e^+-e^- collider. Electrons are generated by a Radio Frequency (RF) gun, accelerated to 7 GeV by a linear accelerator (linac) and then transferred into the High Energy Ring (HER). For the production

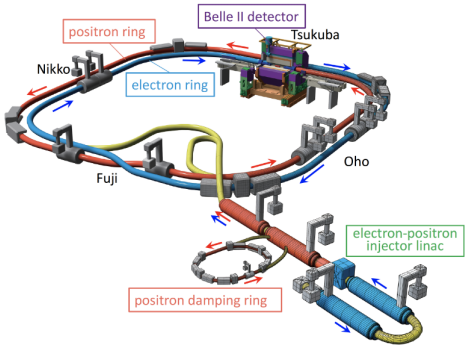

Figure 2.1: Schematic view of the SuperKEKB accelerator [19].

of positrons, a tungsten target is irradiated with electrons that have been accelerated by the linac. The positrons are extracted and transferred to a damping ring to reduce their emittance. Afterwards the positrons are injected into the linac and accelerated to 4 GeV before they are transferred into the Low Energy Ring (LER). The positron and electron beams are then collided at the Belle II detector. In Figure 2.1 a schematic overview of the SuperKEKB accelerator is shown.

The nominal Center Of Mass (COM) energy at the IP is at the $\Upsilon(4S)$ resonance ($m_{\Upsilon(4S)} = 10.58$ GeV). The beam energies can also be adjusted in the range from the $\Upsilon(1S)$ to the $\Upsilon(6S)$ resonance. The nominal COM energy is just above the energy threshold necessary to produce B-meson pairs. Therefore there is no production of fragmentation particles. Since the B-mesons are almost produced at rest in the COM frame the momentum of the B-mesons can be attributed to the boost due to the asymmetric beam energies. This allows to use the boost $\beta\gamma = 0.284$ of the $\Upsilon(4S)$ to convert the distance of the decay vertices in boost direction of the B-mesons $\Delta\ell$ into a proper time difference Δt,

$$\Delta t \approx \frac{\Delta \ell}{\beta \gamma c}. \tag{2.1}$$

Compared to its predecessor SuperKEKB is designed to achieve an instantaneous luminosity 40 times greater. This rise is realized by an increase of beam currents by a factor 2 compared to KEKB. In addition, the beam size at the IP is decreased by a factor 20 according to the nano beam scheme.

2.2 The Belle II Detector

The Belle II detector shares the same dimensions as its predecessor since it uses the same solenoid magnet, but the detector systems have been upgraded to handle the increase in luminosity and the resulting increase in background. Figure 2.2 shows a schematic view of the Belle II detector.

Coordinate System The origin of the Belle II coordinate system is the IP. The x-axis is defined to be horizontal and to point away from the center of the accelerator, the y-axis points vertical upwards and the z-axis is the symmetry axis of the detector roughly pointing in the direction of the electron beam. ϕ is the azimuth and θ is the zenith angle of the z-axis [21]. In this thesis, the acceptance of the electromagnetic calorimeter (ECL) is used to define three detector regions in θ: the forward endcap $[12.4°; 31.4°]$, the barrel $[32.2°; 128.7°]$ and the backward endcap $[130.7°; 155.1°]$. The numbers in squared brackets indicate the θ coverage of each region.

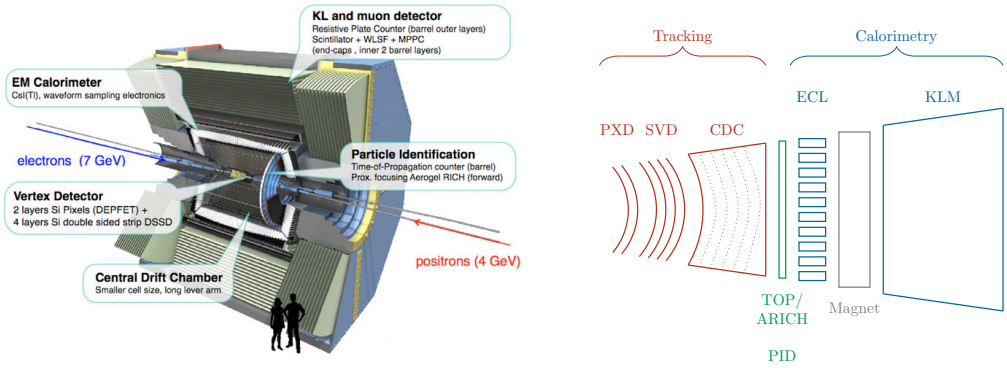

Figure 2.2: Left: layout of the Belle II detector [20]. Right: schematic view of the Belle II detector. The detector parts are shown in red (tracking), green (particle identification (PID)) and blue (calorimetry) according to their primary task.

Vertex Detector (VXD) The innermost detector, the VXD, measures the tracks of charged particles to determine the decay vertex position of particles that decay before reaching the detector. The Belle II VXD consists of two layers of pixel sensors based on the DEPleted Field Effect Transistor (DEPFET) technology [22] surrounded by four layers of silicon strip detectors. Compared to its predecessor which consisted of three layers of strip detectors, the innermost layer of the Belle II VXD is positioned closer to the IP (radius Belle 30 mm, Belle II 14 mm) and the outermost layer is positioned farther from the IP (radius Belle 60.5 mm, Belle II 140 mm) [18],[23]. This has two main consequences. Firstly, the resolution of the vertex reconstruction increases, which is especially advantageous for analyses that rely on a precise vertex reconstruction like the analyses presented in Chapter 4. Secondly, the background rate increases sharply since the background is proportional to the inverse square of the distance to the IP. To cope with the higher background, the pixel sensors are used for the two innermost layers. The first two layers have radii of 14 mm and 22 mm. The first layer using silicon strips has a radius of 38 mm. Pixel sensors have a larger number of channels compared to strip detectors and are therefore able to deal with a higher hit rate due to an increased background.

Central Drift Chamber (CDC) The CDC is a drift chamber filled with a $\mathrm{He} - \mathrm{C_2H_6}$ 50 : 50 gas mixture. It is used to measure the momentum of charged particles by determining their curvature in the magnetic field. In addition, the CDC measures the energy loss of charged particles in its gas volume. This information is used for particle identification since the energy loss per distance $\mathrm{d}E/\mathrm{d}x$ for a given momentum depends on the mass of a particle. Compared to its predecessor at Belle, the CDC at Belle II is bigger (inner radius: 77 mm Belle, 160 mm Belle II;

outer radius: 880 mm Belle, 1130 mm Belle II) and contains more wires (8.400 Belle, 14.336 Belle II). This allows more precise measurements. The acceptance of the CDC in θ ($17° - 150°$) is a limiting factor for many physics analyses.

Particle Identification (PID) System To improve the PID capabilities of the detector, especially the K/π separation, two dedicated PID systems are deployed. Firstly, the time-of-propagation (TOP) counter is installed in the barrel region. In the TOP, Cherenkov photons are created in a quartz bar by incoming charged particles and reflected until they reach photon detectors. The measurement of the x and y impact position of the photons on the photon detectors as well as their propagation time is used to reconstruct Cherenkov rings. The opening angle of the Cherenkov rings gives information about the particle species of the incoming charged particles. Secondly, the proximity-focusing Aerogel Ring-Imaging Cherenkov detector (ARICH) is installed in the forward endcap. In the ARICH, Cherenkov photons are produced in an aerogel by incoming charged particles and measured by photon detectors. Again, measuring the opening angle of reconstructed Cherenkov rings allows to extract PID information.

Electromagnetic Calorimeter The ECL is an electromagnetic calorimeter. Its primary task is the identification of electrons and the measurement of their energy. In Section 2.5 the identification of electrons is explained in more detail and in Chapter 3 an analysis of the electron identification efficiency of the Belle II detector is presented. Further tasks of the ECL are the detection of photons and the measurement of their energy and angular coordinates. The ECL consists of a highly-segmented array of thallium-doped caesium iodide CsI(Tl) crystals with photodiodes glued to their rear surface. Particles that interact with the detector material of the ECL create shower. The shower particles in turn create scintillation photons in the CsI(Tl) crystals which are detected by the photodiodes. The energy resolution of the Belle II ECL is expected to be similar to the energy resolution of the Belle ECL, since most of the Belle ECL components (the crystals, preamplifieres and support structure) have been reused. The Belle ECL energy resolution was $\sigma_E/E = 4\%$ at 100 MeV and 1.6% at 8 GeV.

K_L and Muon Detector (KLM) The KLM detects muons and measures the energy of hadronic interacting K_L. It consists of alternating layers of iron plates and active detector elements. Scintillator strips are used as active detector element in the endcaps and the two innermost layers of the barrel. The outer layers in the barrel consist of glass-electrode resistive plate chambers (RPC). The Belle KLM was purely based on RPCs. In Belle II, the scintillator strips were introduced because of the

higher expected background rate. Scintillator strips have a shorter dead time than RPCs and are therefore better equipped to handle the higher background rate.

2.3 Vertex Fitting

Short lived B-mesons decay before reaching the detector (they fly about 100 µm, the radius of the innermost VXD layer is 14 mm), therefore their decay vertex cannot be measured directly. To obtain the position of the decay vertex, the decay of B-mesons is fitted by combining information from their long lived measurable decay products. This section presents two vertex fitting algorithms used in Chapter 4.

Rave The Rave toolkit has been adapted for Belle II to perform geometric fits *i.e.* fits where one is only interested in the decay vertex position of the B and not in its kinematics. Rave was first developed for the CMS experiment and later transformed into a detector independent toolkit. Rave finds the common origin of input tracks by applying the Kalman Filter technique [24]. Compared to other fitting algorithms that also are using a Kalman Filter, Rave is able to iteratively weight tracks *i.e.* it is able to exclude outlier tracks or assign a lower weight to them. It is particularly useful for fitting decays whose decay structure is unknown, such as the decay of the tag B in the analysis presented in Chapter 4. For more information on Rave see Ref. [25].

TreeFitter TreeFitter is a fitting algorithm originally developed by the BaBar collaboration specifically to perform kinematic fits for B factories *i.e.* fits where the kinematics of particles is extracted as well as their vertex position. TreeFitter takes a decay chain as input and fits it using a Kalman Filter. In contrast to traditional fitting algorithms that fit a decay chain vertex by vertex, TreeFitter performs a global fit of the whole decay chain. This global fit method improves the fit of vertices that normally are only poorly fitted, for example vertices of decays with neutral or missing particles, since it allows to communicate information from one vertex to another. For more information on TreeFitter see Ref. [26].

2.4 Flavor Tagger

For measurements of the mixing frequency Δm_d and the time-dependent CP violation parameter $\sin(2\phi_1)$ the flavor of the tag side B accompanying the signal side B needs to be determined. For Belle II a multivariate flavor tagging algorithm was developed. The algorithm takes kinematic and particle identification information of the tag side particles as input. The output is given as the product $q \cdot r$, where q is 1 (-1) for tag B ($\overline{\mathrm{B}}$) and r is a dilution factor. The dilution factor is 1 if the flavor of the tag B

is determined with absolute certainty and 0 if the flavor cannot be determined with any certainty. In a study using early Belle II data, the Belle II flavor tagger reached an efficiency on par with the efficiency of of the Belle flavor tagger (efficiency Belle II $(33.8 \pm 3.9)\%$, Belle $(30.1 \pm 0.4)\%$) [27]. For more information on the flavor tagger see [28].

2.5 Particle Identification

Reliable PID is a key requirement to achieve the physics goals of the Belle II collaboration. At Belle II, a likelihood based approach is used to identify charged particles. In the approach, five different particle hypotheses $(\mathrm{e}, \mu, \pi, \mathrm{K}, \mathrm{p})$ are considered. For each of the hypotheses a likelihood is calculated for each sub-detector independently based on the sub-detectors information. The likelihoods from each sub-detector for a particle hypothesis i can then be combined by

$$\mathcal{L}_{\mathrm{i}} = \prod_{\mathrm{det}} \mathcal{L}_i^{\mathrm{det}}, \tag{2.2}$$

where det runs over all sub-detectors suitable for PID (CDC, TOP, ARICH, ECL, KLM). The ratio of the likelihoods of the particle hypotheses is then used to define a global PID probability. It is calculated for particle hypothesis i as

$$\mathrm{P}_i = \frac{\mathcal{L}_i}{\sum_j \mathcal{L}_j}, \tag{2.3}$$

where j runs over all particle hypotheses $(\mathrm{e}, \mu, \pi, \mathrm{K}, \mathrm{p})$. Many physics analyses only need information to distinguish between two particle hypotheses because the selection already reliably suppresses the others. In this case, it is possible to calculate a binary PID probability by letting j run just over those two hypotheses. Using the example of electron identification (eID), in the remainder of this section it is explained in more detail how the likelihood is constructed using information from the detector.

2.5.1 Electron Identification

Electrons are distinguished from other particles mainly by the energy measured in the ECL, E, over the the track momentum, p. For electrons the E/p distribution peaks sharply near one, since electrons deposit almost their whole energy in the ECL. For other charged particles, such as muons and pions, the distribution peaks at lower values. In Fig. 2.3, the E/p distribution for electrons, muons and pions is shown for low and high momentum. While for high momentum the E/p distribution of electrons peaks sharply, for low momentum a large tail towards low values is observable. Electrons with low momentum travel further outside of the ECL, since their tracks

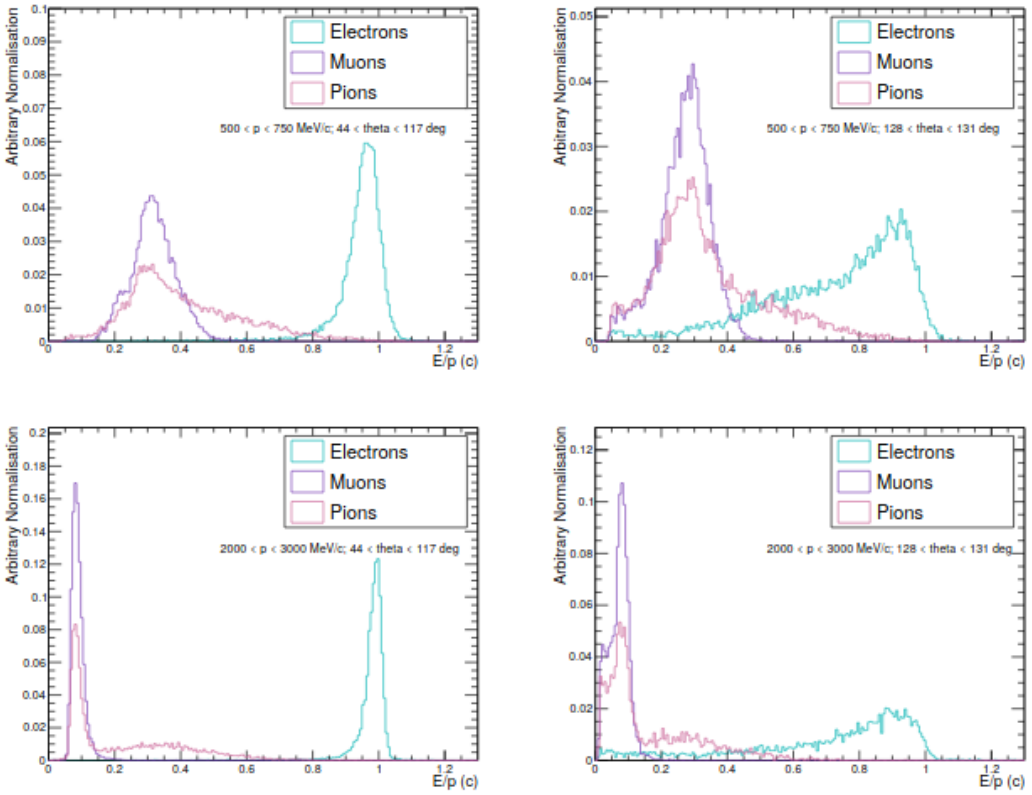

Figure 2.3: The E/p distribution for electrons, muons and pions in the 500 MeV $< p <$ 750 MeV (upper plots) and 2000 MeV $< p <$ 3000 MeV (lower plots) momentum range. The distributions are shown on the left side for a central part of the barrel ($44° < \theta < 117°$) and on the right side for the region between the barrel and the backward endcap ($128° < \theta < 131°$) [17].

are bent more strongly due to the magnetic field. This leads to a greater energy loss outside of the ECL resulting in lower E/p. Particles also lose a lot of energy close to the transition region between the barrel and the endcaps as there is no active detector material in this region. Because of the less discriminant E/p distribution it is significantly more difficult to distinguish electrons with low momentum from other particles than electrons with high momentum. Although other sub-detectors still provide eID information for low momentum (CDC via $\mathrm{d}E/\mathrm{d}x$ measurement, TOP/ARICH via the measurement of Cherenkov rings and KLM via muon detection). In Chapter 3, an analysis of the efficiency of the eID is presented.

Chapter 3

Lepton Identification Efficiency

In this chapter, a study of the electron identification (eID) using radiative Bhabha events is presented. Bhabha-like candidates are selected and a tag and probe approach is then used to asses the performance of the eID. Tight requirements are applied on one of the leptons in the event (the tag). A cut, eID > 0.90, is then applied on the other lepton (the probe) and the efficiency of this cut is evaluated. Bhabha events have been chosen for this analysis because they provide a very clear signature in the detector *i.e.* two back-to-back tracks associated with an energy cluster in the ECL and no other tracks seen in the detector. In Fig. 3.1, a typical Bhabha event recorded with the Belle II detector is shown. This makes Bhabha events particularly useful for the tag and probe approach, since it is very easy to select them by applying a strict selection to one of the tracks. In addition, Bhabha events allow to study the eID efficiency in a very wide momentum range, since the leptons only loose energy due to radiated photons. Bhabha events are also very common since their cross section at the energy of the $\Upsilon(4S)$ resonance is high (cross section: Bhabha ≈ 300 nb, $\Upsilon(4S) \approx 1$ nb). This allows to determine the eID efficiency with a high statistical accuracy even with a low integrated luminosity. The analysis presented in this chapter provided - together with other lepton identification efficiency studies - results for ICHEP 2020 [29]. A paper is in preparation. I did not develop this analysis from scratch but was able to build on the previous work

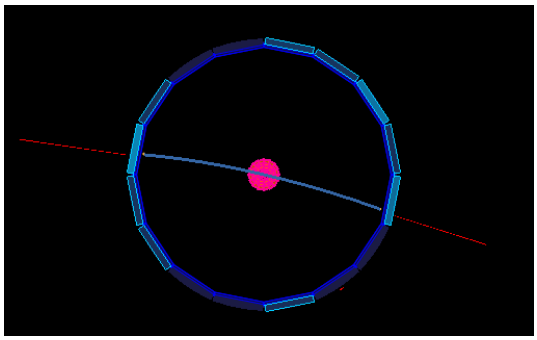

Figure 3.1: Event display of a Bhabha event.

of others. When I started working on the analysis, it was already decided to use Bhabha events in a tag and probe approach but the necessary code base to calculate the eID efficiency was not yet developed. In addition, the selection shown in Fig. 3.2 had already been devised except for the selection of a trigger. In the remainder of this chapter the analysis is presented. The structure of the presentation follows the structure of the internal Belle II note of this analysis [30].

3.1 Data Sets

In this analysis, three datasets are used to study the eID efficiency and assess whether the efficiencies change over time. The samples are listed in Tab. 3.1. In addition, simulated background and Bhabha events are used to estimate background contamination, asses a possible trigger bias and to determine the eID efficiency. In this analysis, simulation samples corresponding to the understanding of the detector conditions in 2019 and another corresponding to the understanding of the detector conditions in 2020 are used. The simulation samples are listed in Tab. 3.2 and in Tab. 3.3.

Table 3.1: Datasets used in this analysis.

Sample	Integrated luminosity [fb^{-1}]
July 2019	5.219
January 2020	5.023
June 2020	34.6

Table 3.2: 2019 simulation samples.

Sample	Number of events [10^6]	Equivalent luminosity [fb^{-1}]
$e^+e^- \to e^+e^-$	50	0.167
$e^+e^- \to e^+e^-e^+e^-$	210.6	5.30
$e^+e^- \to e^+e^-\mu^+\mu^-$	100	5.29
$e^+e^- \to \mu^+\mu^-$	55	47.9
$e^+e^- \to \tau^+\tau^-$	91.9	100

Table 3.3: 2020 simulation samples.

Sample	Number of events [10^6]	Equivalent luminosity [fb^{-1}]
$e^+e^- \to e^+e^-$	30000	100
$e^+e^- \to e^+e^-e^+e^-$	3970	100
$e^+e^- \to e^+e^-\mu^+\mu^-$	1890	100
$e^+e^- \to \mu^+\mu^-$	114.8	100
$e^+e^- \to \tau^+\tau^-$	91.9	100

3.2 Selection

In this study, events that are recorded by a low multiplicity trigger are analyzed. The trigger requires a cluster in the barrel region of the ECL with an energy above 2 GeV. To minimize a possible trigger bias on the probe, a trigger emulation is applied on the tag particle to ensure that the tag fired the trigger. Since the trigger simulation (TSIM) of Belle II is not fully developed yet, only the trigger emulation is applied in simulation. Recorded events are selected as Bhabha-like if they contain two tracks originating from the IP. To ensure the latter, the transverse distance of the origin of the tracks with respect to the IP $\mathrm{d}r$ must satisfy $|\mathrm{d}r| < 2$ cm and the z position of the origin of the tracks with respect to the IP $\mathrm{d}z$ must satisfy $|\mathrm{d}z| < 5$ cm. To suppress background events with missing particles, a cut of $m^2_{\mathrm{Recoil}} < 10\ \mathrm{GeV}^2$ is applied on the squared invariant mass of the recoiling system computed as

$$m^2_{\mathrm{Recoil}} = (\sqrt{s} - p)^2, \tag{3.1}$$

where $\sqrt{s}$ is the center of mass energy and p is the sum of the four momentum vectors of the e^+ and e^-. The tag is also required to satisfy eID > 0.95. Figure 3.2 shows the θ and p distributions for negatively charged probe candidate tracks for the June 2020 dataset and the 2020 simulation sample. For $p < 3$ GeV a slight discrepancy between data and MC is observed, otherwise data and MC agreement is good overall. In all bins the background contamination is lower than 0.5 %. Fig. 3.3 shows the same for positively charged probe candidate tracks.

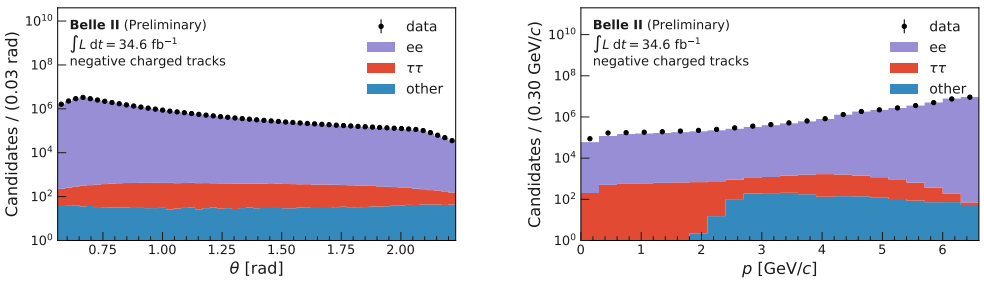

Figure 3.2: Left (Right): θ (p) distribution of negatively charged probe candidate tracks in the barrel. Data is depicted as black points with error bars. The distribution in the simulation samples is shown as purple (ee sample), red ($\tau\tau$ sample) and blue (eeee, ee$\mu\mu$ and $\mu\mu$ samples) filled area.

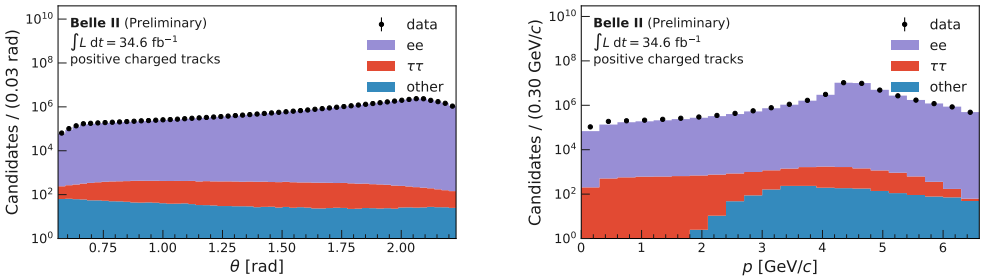

Figure 3.3: Left (Right): θ (p) distribution of positively charged probe candidate tracks in the barrel. Data is depicted as black points with error bars. The distribution in the simulation samples is shown as purple (ee sample), red ($\tau\tau$ sample) and blue (eeee, ee$\mu\mu$ and $\mu\mu$ samples) filled area.

3.3 Analysis Strategy

The efficiency ε of a given eID cut is computed as the number of probe leptons N_{probe} satisfying the cut over the total number of selected events N_{tot},

$$\varepsilon = \frac{p_{\text{probe}} \cdot N_{\text{probe}}}{p_{\text{tot}} \cdot N_{\text{tot}}}. \tag{3.2}$$

The purity $p_{\text{probe/tot}}$ designate the probability that the probe electron (positron) track candidate is correctly identified, *i.e.* corresponds to an actual electron (positron). The purities are computed using the simulated samples, as

$$p_{\text{tot/probe}} = \frac{N^{\text{Sig}}_{\text{tot/probe}}}{N^{\text{Sig}}_{\text{tot/probe}} + N^{\text{BG}}_{\text{tot/probe}}}, \tag{3.3}$$

where $N^{\text{Sig}}_{\text{tot}}$ ($N^{\text{Sig}}_{\text{probe}}$) is the number of events with a correctly identified probe and $N^{\text{BG}}_{\text{tot}}$ ($N^{\text{BG}}_{\text{probe}}$) is the number of events with a mis-identified probe before (after) applying the eID requirement on the probe.

3.3.1 Binning

The eID efficiency is calculated in bins of p and θ. Tab. 3.4 shows the binning used in this study. It is chosen to be consistent with other LID efficiency studies performed at Belle II.

Table 3.4: Left (Right): definition of the p (θ) bins.

p bins [GeV/c]
(0.4,0.5)
(0.5,1)
(1,1.5)
(1.5,2)
(2,2.5)
(2.5,3)
(3,3.5)
(3.5,4)
(4,4.5)
(4.5,5)
(5,5.5)
(5.5,6)
(6,6.5)
(6.5,7)

θ bins [rad]
(0.56,1.13)
(1.13,1.57)
(1.57,1.88)
(1.88,2.23)

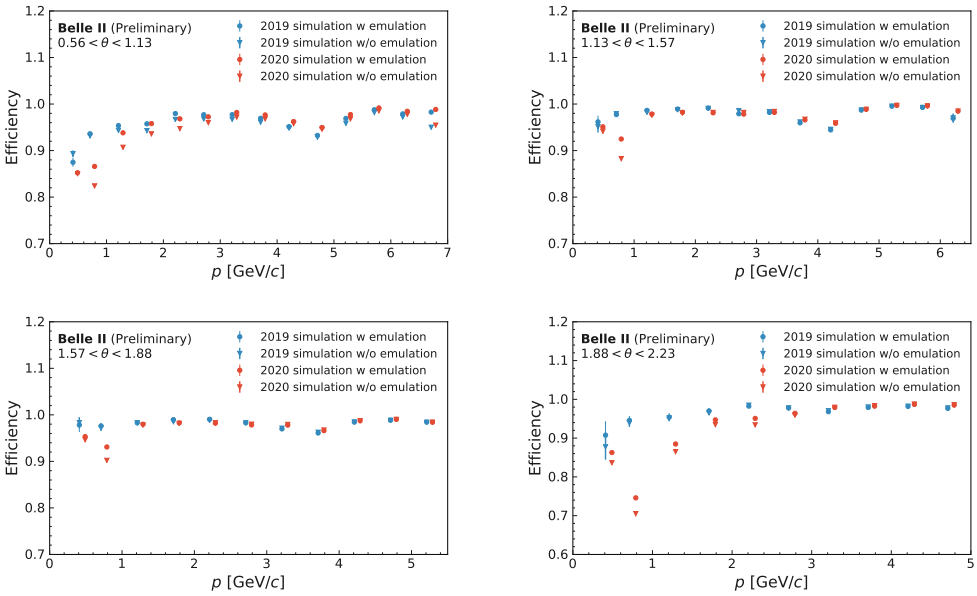

Figure 3.4: eID efficiency for negatively charged probe candidate tracks in the different θ bins. The eID efficiency calculated using the 2020 Bhabha simulation sample (2019 Bhabha simulation sample) with applied trigger emulation is shown as red (blue) dots with errorbars and the eID efficiency without applied trigger emulation is shown as red (blue) triangles with errorbars. The efficiency is calculated according to the binning defined in Tab. 3.4 but the dots/triangles are slightly shifted between the simulation samples for better visibility.

3.3.2 Systematic Uncertainties

Two sources of systematic uncertainties are considered. Firstly, the eID efficiency is computed with and without applying the purity factors. The absolute difference is used as a source of systematic uncertainty related to the background contamination. This treatment of the systematic uncertainty is rather conservative as it includes a scenario where there is no background contamination. However, the calculated systematic uncertainty is very low. It is at most $\approx 0.6\%$. Secondly, a possible trigger bias is estimated by computing the eID efficiency in the simulated Bhabha sample with and without applied trigger emulation. Fig. 3.4 and Fig. 3.5 show the computed efficiencies for negatively and positively charged probe tracks. The absolute difference between both efficiencies is taken as a systematic uncertainty related to the trigger bias. In the following, the trigger bias for the 2020 simulation sample is discussed. The figures show a bias introduced by the trigger for $p < 1$ GeV/c of $\approx$ 5%. With the exception of positrons in the forward (backward) part of the barrel where it

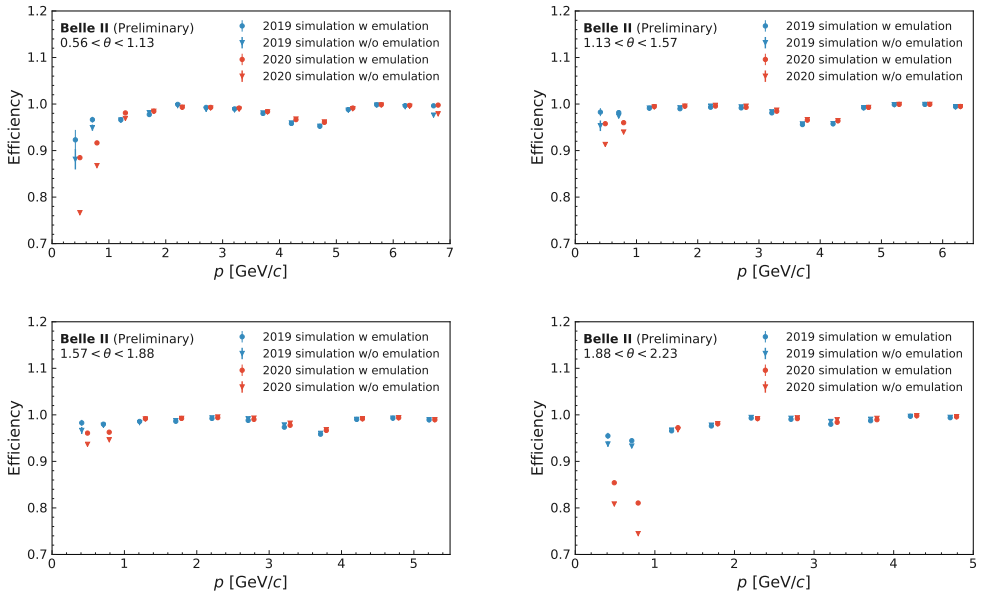

Figure 3.5: eID efficiency for positively charged probe candidate tracks in the different θ bins. The eID efficiency calculated using the 2020 Bhabha simulation sample (2019 Bhabha simulation sample) with applied trigger emulation is shown as red (blue) dots with errorbars and the eID efficiency without applied trigger emulation is shown as red (blue) triangles with errorbars. The efficiency is calculated according to the binning defined in Tab. 3.4 but the dots/triangles are slightly shifted between the simulation samples for better visibility.

reaches $\approx 15\%$ ($\approx 10\%$). In addition, both figures show a bias of $\approx 2\%$ for electrons with a momentum of $1 < p < 3$ GeV/c. Otherwise the estimated trigger bias is below 1%. The trigger bias is the dominating source for systematic uncertainty for low momentum. For higher momentum it is equal to the bias due to the background contamination. It is understood that the trigger bias stems from the fact that the trigger distorts the θ distribution of the tag tracks. Due to event kinematics this also distorts the θ distribution of the probe. This leads to a modified eID efficiency, since the eID efficiency is not completely flat as a function of θ. This effect will decrease if a finer θ binning is chosen in future studies. More information on the θ dependency of the eID efficiency are given in Section 3.5.1.

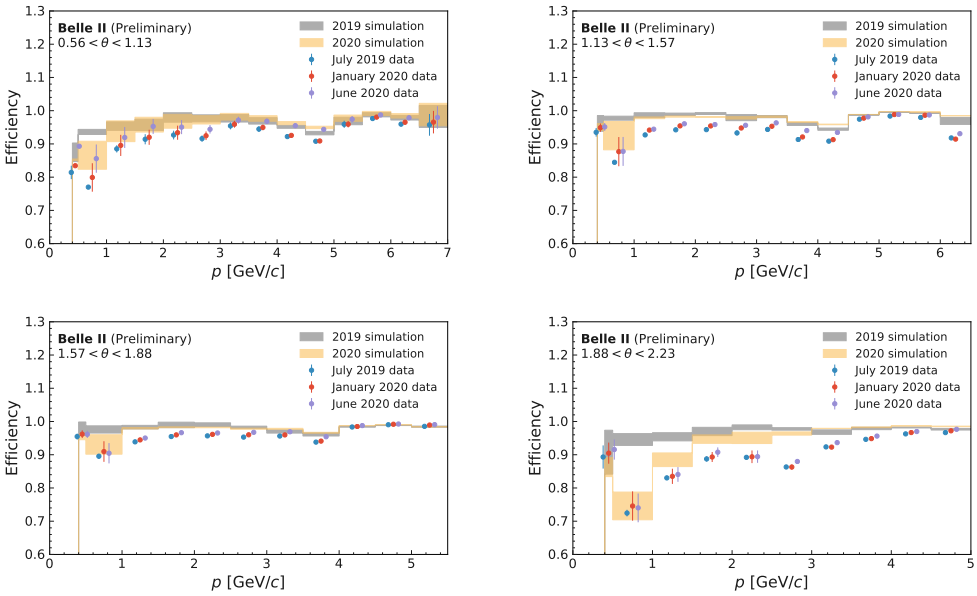

Figure 3.6: eID efficiency for negatively charged probe candidate tracks in the different θ bins. The efficiency calculated using the simulation samples is shown as grey bars (2019 simulation) and yellow bars (2020 simulation). The efficiency calculated using the data samples is shown as blue points with errorbars (July 2019 data), as red points with errorbars (January 2020 data) and as purple points with errorbars (June 2020). The efficiency is calculated according to the binning defined in Tab. 3.4 but for data the points with errorbars are slightly shifted for better visibility. The errorbars and errorbands are discussed in Section 3.4.

3.4 Results

The eID efficiency calculated for negatively (positively) charged probe candidate tracks is shown in Fig. 3.6 (Fig. 3.7). For the simulation samples, the errorbands of the efficiency display the systematic uncertainty related to the trigger bias and the linearly added statistical uncertainty. The systematic uncertainty related to background contamination is neglected since only the Bhabha simulation sample is used to calculate the displayed efficiency. This sample does not contain background. For the data samples, the errorbars of the efficiency show the systematic uncertainties added in quadrature and the linearly added statistical uncertainty. With the current amount of available data, the analysis is dominated by the systematic uncertainty. This is especially true for lower momentum bins where a larger trigger bias is observed. In some bins, the errorbars are above an efficiency of 1, which is unphysical.

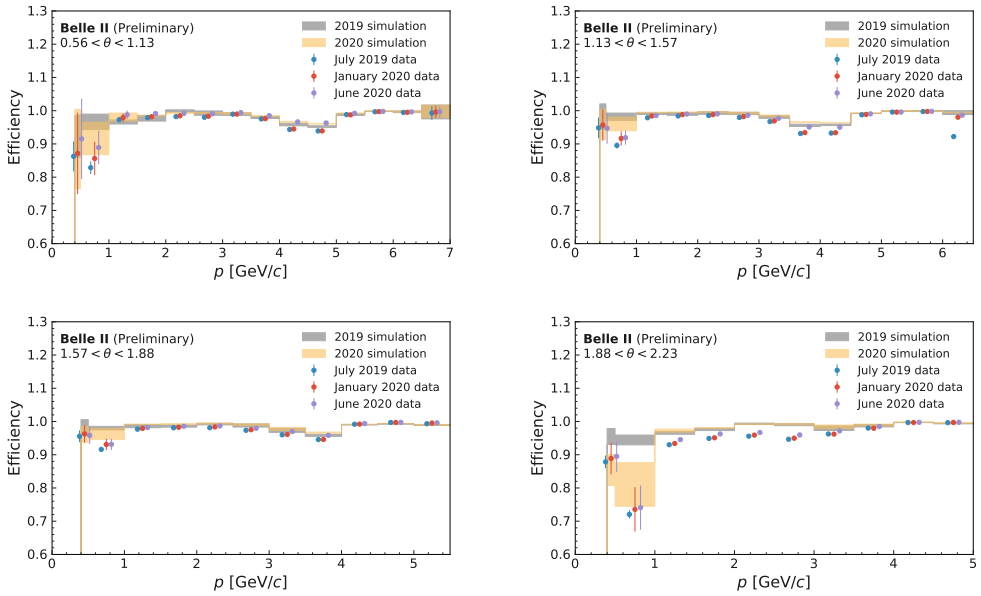

Figure 3.7: eID efficiency for positively charged probe candidate tracks in the different θ bins. The efficiency calculated using the simulation samples is shown as grey bars (2019 simulation) and yellow bars (2020 simulation). The efficiency calculated using the data samples is shown as blue points with errorbars (July 2019 data), as red points with errorbars (January 2020 data) and as purple points with errorbars (June 2020). The efficiency is calculated according to the binning defined in Tab. 3.4 but for data the points with errorbars are slightly shifted for better visibility. The errorbars and errorbands are discussed in Section 3.4.

This is due to the fact that all errors are calculated symmetrically. The different distributions show the same general trends. The eID efficiency increases with momentum, as the E/p distribution is more discriminatory for tracks with higher momentum as discussed in Section 2.5.1. The eID efficiency is especially low for $p \approx 0.7$ GeV/c. This is due to the fact that also the $\mathrm{d}E/\mathrm{d}x$ is less discriminatory in this momentum range since the kaon and electron $\mathrm{d}E/\mathrm{d}x$ bands cross. For more recent data, the eID efficiency increases slightly due to a better understood detector. The efficiency calculated using the simulation samples is slightly higher than the efficiency calculated in data. This discrepancy decreases for the 2020 simulation samples.

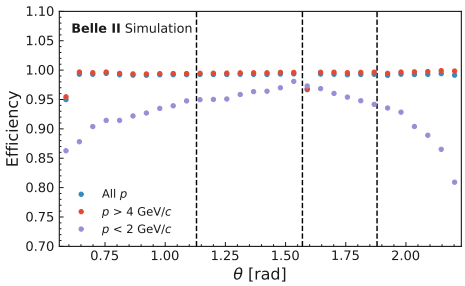

Figure 3.8: eID efficiency for positively charged probe candidate tracks in simulated Bhabha events of the 2020 simulation sample. The efficiency is shown as a function of θ for the whole p range (blue dots), high p (red dots) and low p (purple dots). The dashed lines indicate the borders of the θ bins defined in Section 3.3.1.

3.5 Outlook

The presented study provides results for the eID efficiency with data collected by Belle II until summer 2020. There are several ways how the study can be improved. For example, the study can contribute to a better understanding of the detector by calculating not only the efficiency for the global eID, *i.e.* for the eID including all subdetectors and possible particle hypotheses, but also the eID efficiency only based on information from certain subdetectors or by comparing only certain particle hypotheses. In addition, the high level trigger (HLT) system of Belle II has switched from monitoring to filtering mode in autumn 2020 due to the increasing instantaneous luminosity and the resulting increase in generated data. Therefore a suitable HLT has to be found for the study. In this section different ways to improve the study for the data that have already been analyzed are presented.

3.5.1 Binning

As a cross check, the eID efficiency is calculated as a function of θ in bins of p using simulated Bhabha events. The result is shown for positively charged probe candidate tracks in Fig. 3.8. For high p, the eID efficiency is flat as a function of θ for most of the θ range. Deviations from flat behavior are observable near the forward endcap and for $\theta \approx 1.59$ rad. For low p, a dependence of the eID efficiency on θ is observable. The eID efficiency peaks at $\theta \approx 1.53$ rad and decreases towards the endcaps. Ideally, the eID efficiency in the presented eID efficiency study should be flat in a θ bin. This is not the case for all of the current θ bins. This is an issue with the current θ binning, which can be solved by switching to thinner θ bins. As explained in Section 3.3.1, the current binning has been chosen to be consistent with other eID efficiency studies

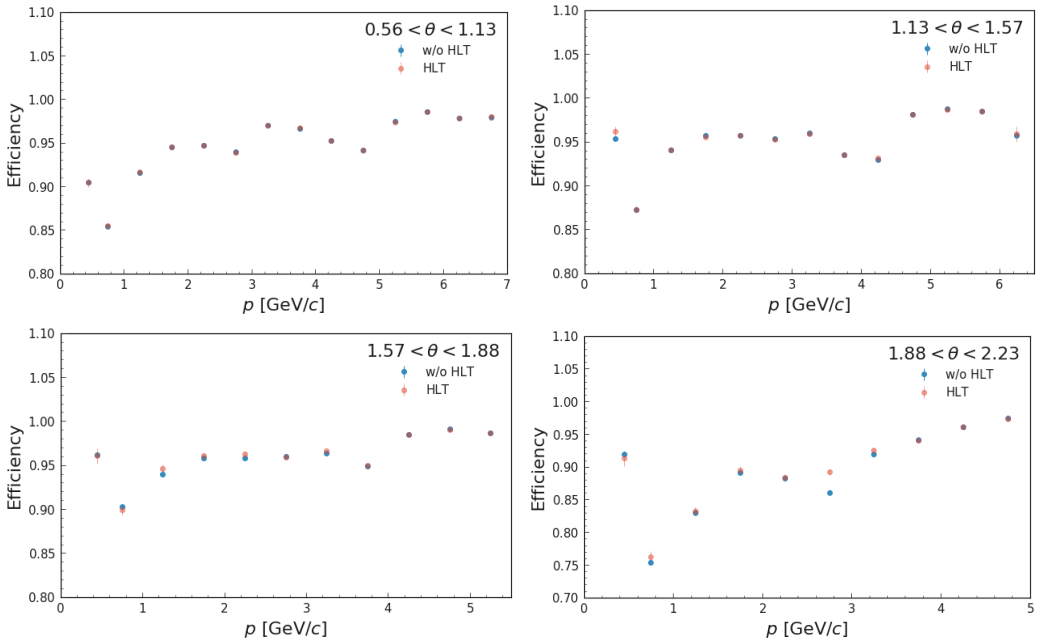

Figure 3.9: eID efficiency in 10 fb^{-1} of data for negatively charged probe tracks without (blue points with errorbars) and with (red points with errorbars) applied Bhabha HLT.

performed at Belle II. These studies are statistically limited. In the future, it will be possible to switch to a thinner θ binning with increasing integrated luminosity.

3.5.2 High Level Trigger

Up to the summer of 2020 the HLT system of Belle II ran in monitoring mode, from autumn 2020 onwards the HLT system runs in filtering mode. The HLT system of Belle II is a software trigger system. Events are reconstructed and selected if they fulfill the requirements of an HLT line. The HLT lines impose loose requirements on the topology of events, for example by requiring two tracks with an associated ECL cluster in an event. Possible HLT lines for this study were analyzed using a subset of 10 fb^{-1} of available data. The impact of a HLT line on the efficiency was assessed by computing the eID efficiency with and without applied HLT line. Figure 3.9 shows the efficiency for a HLT line that selects Bhabha events. The trigger retains 10% of the events due to the fact that the trigger randomly discards 90% of the selected events to decrease the event rate. Some bias can be observed for $p \approx 2.75$ GeV/c in the backward part of the barrel. This bias is due to the fact that the eID efficiency is not flat as function of θ in the backward barrel and the

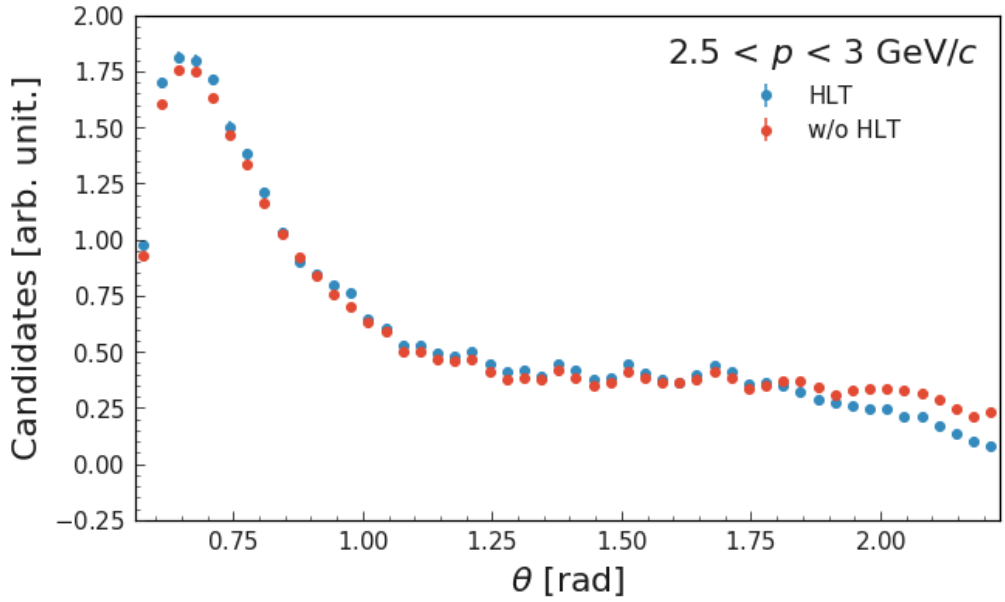

Figure 3.10: θ distribution in 10 fb^{-1} of data for negatively charged probe tracks without (blue points with errorbars) and with (red points with errorbars) applied Bhabha HLT.

trigger warps the θ distribution in this momentum range. Figure 3.10 shows the θ distribution with and without applied HLT line in this momentum range. In general, the bias introduced by this HLT line is lower than the already existing trigger bias and therefore not problematic for this analysis. In future, this trigger can be used for the study and its bias can be computed similarly to how its done for the trigger in 3.3.2.

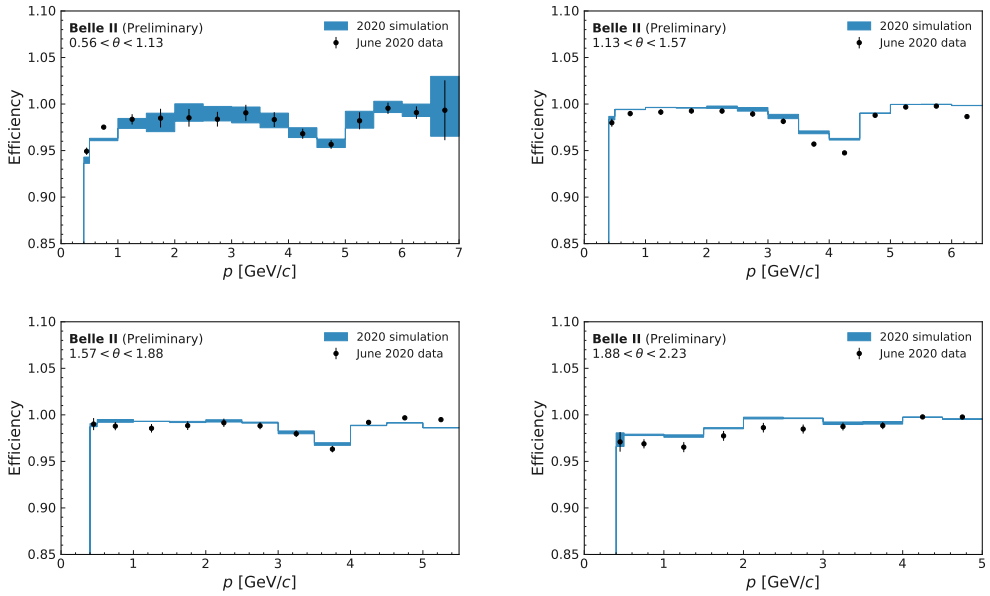

Figure 3.11: Binary e−π eID efficiency for negatively charged probe candidate tracks in the different θ bins. The efficiency calculated using the 2020 simulation samples is shown as blue bar and the efficiency calculated using the June 2020 dataset as black dots with errorbars. The errorbars are derived the same way as for the plots discussed in Section 3.4.

3.5.3 Binary Particle Identification

As explained in Section 2.5, it is also possible to compute a binary PID by considering only two particle hypotheses. The efficiency of this binary PID also needs to be assessed. The binary e−π eID efficiency can be calculated in a similar way to the regular eID efficiency by replacing the eID cut on the probe by a binary e−π eID cut. In Fig. 3.11, the efficiency for a probe cut of binary e−π eID > 0.90 for negatively charged probe candidate tracks in the June 2020 dataset and the 2020 simulation samples is shown. In the two central θ bins the binary e−π eID efficiency is flat in most of the p range and drops for $p \approx 3 - 4.5$ GeV/c. In the two outer θ bins the binary e−π eID efficiency increases with p and drops in the forward θ bin for $p \approx 4 - 5.5$ GeV/c. Compared to the efficiency of the regular eID, the binary e−π eID efficiency does not drop for $p \approx 0.7$ GeV/c. This is expected because the drop is understood to come from the difficulty of separating kaons and electrons and the kaon hypotheses is no longer considered.

3.6 Summary

In the analysis presented in this chapter, the eID efficiency of the Belle II detector was calculated using Bhabha events in a tag and probe approach. Events are selected by applying tight requirements on the tag particle and a cut of eID > 0.90 is applied on the probe particle. The efficiency of the cut on the probe particle is then computed using three different datasets which became available in July 2019, January 2020 and June 2020. The analysis shows that the eID of Belle II is performing adequately and its efficiency is increasing over time. The eID efficiency was also calculated using simulation samples. The ratio between the eID efficiency calculated using data and simulation samples is made available internally for the Belle II collaboration. Analysts can use this ratio to weight the events in their analysis to account for data-simulation discrepancies. The eID cut on the probe can be changed to a different cut (or to binary eID) to provide data-simulation efficiency ratios for different working points depending on the needs of an analysis. In the future, this study will be repeated using more recent data and simulation samples. For this, the analysis needs to be modified since the HLT system of Belle II will switch to filtering mode. A HLT line suitable for this analysis and its impact on the eID efficiency has been presented.

Chapter 4

Prompt $B^0 \to J/\psi\ K_S$ analysis

In the previous chapter, a measurement of one of the Belle II detector properties, the lepton identification efficiency, was presented. This technical measurement demonstrated that the lepton identification at Belle II is sufficiently understood to be used in physics analyses. In this chapter, a measurement of physics parameters is presented. The mixing frequency Δm_d in the system of neutral B-mesons and the angle ϕ_1 of the CKM triangle shown in Fig. 1.2 are measured. The angle ϕ_1 can be extracted by measuring the asymmetric time-dependent decay rates of neutral B- and $\overline{\mathrm{B}}$-mesons into a charmonium rich CP eigenstate. The asymmetry of the decay rates is given by [7]

$$A(t) = \frac{\Gamma(\overline{\mathrm{B}}^0(t) \to f) - \Gamma(\mathrm{B}^0(t) \to f)}{\Gamma(\overline{\mathrm{B}}^0(t) \to f) + \Gamma(\mathrm{B}^0(t) \to f)} = S_f \sin(\Delta m_d t) - C_f \cos(\Delta m_d t), \quad (4.1)$$

where

$$S_f = \frac{2\ \mathrm{Im}\lambda_f}{1+|\lambda_f|^2}, \quad C_f = \frac{1-|\lambda_f|^2}{1+|\lambda_f|^2}, \quad \lambda_f = e^{-2i\phi}\frac{\overline{A}_f}{A_f}. \quad (4.2)$$

Here, $e^{-2i\phi}$ is a complex phase related to the $\mathrm{B}-\overline{\mathrm{B}}$ mixing, $\Gamma(\overline{\mathrm{B}}^0(t) \to f)$ ($\Gamma(\mathrm{B}^0(t) \to f)$) is the decay rate of B-mesons ($\overline{\mathrm{B}}$-mesons) into the final state f, A_f ($\overline{A}_f$) is the amplitude of the $\mathrm{B}^0 \to f$ ($\overline{\mathrm{B}}^0 \to f$) decay and t is a proper time. For decays into a charmonium rich CP eigenstate it can be approximated with a precision better then one percent that [7]

$$\lambda_f = -e^{-2i\phi_1} \Rightarrow S_f = \sin(2\phi_1), \quad |\lambda_f| = 1 \Rightarrow C_f = 0. \quad (4.3)$$

The asymmetry of the time-dependent B- and $\overline{\mathrm{B}}$-meson decay rates then becomes

$$A(t) = \sin(2\phi_1)\sin(\Delta m_d t). \quad (4.4)$$

Therefore the measurement of $A(t)$ allows to extract ϕ_1. For the measurement of ϕ_1 presented in this chapter, decays into the CP eigenstates $\mathrm{B}^0 \to \mathrm{J}/\psi(\to \mu^+\mu^-)\mathrm{K_S}$ and $\mathrm{B}^0 \to \mathrm{J}/\psi(\to \mathrm{e}^+\mathrm{e}^-)\mathrm{K_S}$ are analyzed. Both decays are charmonium rich which is necessary for the approximation shown in Eq. 4.3. In addition, both decays have

a relatively large branching fraction and only low experimental background. To be able to perform the measurement of ϕ_1, the flavor of the tag B accompanying the B that decays into a CP eigenstate needs to be determined. For this purpose the flavor tagging algorithm explained in Section 2.4 is used. In addition, as explained more thoroughly in Section 4.1, the wrong tag fraction w *i.e.* the fraction of events where the flavor tagging algorithm determines the flavor of the tag side B wrongly also needs to be known. The wrong tag fraction can be measured by analyzing flavor specific decays. In this analysis, the flavor specific decay $\mathrm{B}^0 \to \mathrm{D}\pi$ is used to determine w. As a byproduct, the analysis of this decay allows to measure Δm_d as discussed in Section 4.1. The aim of the analysis presented in this chapter is to provide a first measurement of Δm_d and $\sin(2\phi_1)$ of Belle II in time for the ICHEP 2020 conference. Its aim is not to provide a precision measurement. In Section 4.9, the necessary steps to transform this prompt measurement into a precision measurement are discussed. The analysis was jointly developed by physicists at the university of Prague and the Max-Planck-Institute for Physics in Munich. The structure of this chapter follows the internal Belle II note of this analysis [31]. The note was written to obtain permission for unblinding before the ICHEP 2020 conference. The structure of this chapter and the areas of the analysis I contributed to are summarized in the bullet list below.

- In Section 4.1, the strategy to measure Δm_d and $\sin(2\phi_1)$ is summarized;
- In Section 4.2, the data samples used in this analysis are presented;
- In Section 4.3, the selection criteria for tracks and composite particles are discussed. I contributed to the development of the final selection;
- In Section 4.4, the extraction of the proper time difference shapes and the beam constrained mass shapes using simulation samples is presented. I extracted the beam constrained mass shapes;
- In Section 4.5, the obtained shapes and the general fitting procedure are tested using simulated samples. I participated in running of the presented pseudo-experiments;
- In Section 4.6, checks of the analysis procedure using real data samples are presented. I performed the presented checks;
- In Section 4.7, systematic uncertainties are discussed.
- In Section 4.8, the result of the analysis is shown.
- In Section 4.9, the analysis is summarized and the next steps to perform a precision measurement of $\sin(2\phi_1)$ at Belle II are discussed.

4.1 Analysis Strategy

As discussed in Section 2.1, neutral B-meson pairs are created by the SuperKEKB accelerator. Neutral B-mesons oscillate before they eventually decay. For the measurement of $\sin(2\phi_1)$, one of the B-mesons, referred to as signal B, $\mathrm{B}^0_{\mathrm{sig}}$, decaying into the CP eigenstate $\mathrm{B}^0 \to \mathrm{J/\psi\ K_S}$ is fully reconstructed. The other B, referred to as tag B, $\mathrm{B}^0_{\mathrm{tag}}$, is partially reconstructed by combining the remaining tracks in the event. After the reconstruction, a flavor tagging algorithm is used to determine the flavor of the $\mathrm{B}^0_{\mathrm{tag}}$. Depending on the flavor of the $\mathrm{B}^0_{\mathrm{tag}}$ events are classified as positive or negative flavor events. Negative (positive) flavor events are those events in which the $\mathrm{B}^0_{\mathrm{tag}}$ is tagged as a $\overline{\mathrm{B}}^0$ (B^0). Since both B-mesons are created in an entangled state the $\mathrm{B}^0_{\mathrm{sig}}$ has opposite flavor of the $\mathrm{B}^0_{\mathrm{tag}}$ at the time of the $\mathrm{B}^0_{\mathrm{tag}}$ decay. Therefore measuring the lifetime of the $\mathrm{B}^0_{\mathrm{sig}}$ from the moment of the $\mathrm{B}^0_{\mathrm{tag}}$ decay gives a proper time for the measurement of $\sin(2\phi_1)$. To extract the decay time difference of the B-mesons the position of the signal $\mathrm{B}^0_{\mathrm{sig}}$ decay vertex is fitted using TreeFitter while the position of the $\mathrm{B}^0_{\mathrm{tag}}$ vertex is fitted using Rave. The advantages of both fitting algorithms are discussed in Section 2.3. Using the output of the respective fit, the distance $\Delta\ell$ between the decay vertices can be calculated as,

$$\Delta\ell = \ell(\mathrm{B}^0_{\mathrm{sig}}) - \ell(\mathrm{B}^0_{\mathrm{tag}}), \tag{4.5}$$

where ℓ is the coordinate along the boost direction axis. Using the boost $\beta_{\Upsilon(4S)}\gamma_{\Upsilon(4S)}$ of the $\Upsilon(4S)$, the speed of the B-mesons relative to the speed of light β_{B}, the nominal lifetime of neutral B-mesons $\tau^0_{\mathrm{B}} = 1.52$ [ps] and the θ_{CMS} position of the $\mathrm{B}^0_{\mathrm{sig}}$ in the center-of-mass frame, $\Delta\ell$ can be converted into a proper time difference Δt,

$$\Delta t \approx \frac{\Delta\ell}{\beta_{\Upsilon(4S)}\gamma_{\Upsilon(4S)}c} + \frac{\beta_{\mathrm{B}}}{\beta_{\Upsilon(4S)}}(\tau^0_{\mathrm{B}} + \frac{\Delta\ell}{\beta_{\Upsilon(4S)}\gamma_{\Upsilon(4S)}c})\cos(\theta_{\mathrm{CMS}}). \tag{4.6}$$

The first term in Eq. 4.6 is the exact formula to calculate Δt if $\Delta\ell$ is perfectly measured and the B-mesons are produced completely at rest in the $\Upsilon(4S)$ frame. The second term contains corrections developed by the Belle II collaboration since the B-mesons are not created completely at rest in the $\Upsilon(4S)$ frame. Similar corrections were already performed at BaBar [32]. It is useful to define three different Δt:

- $\Delta t_{\mathrm{gen}} = \tau(\mathrm{B}^0_{\mathrm{sig}}) - \tau(\mathrm{B}^0_{\mathrm{tag}})$ is the true decay time difference between the two B-mesons and is accessible only in the simulation;
- Δt_{MC} is the decay time difference approximation computed with Eq. 4.6 using the true coordinate ℓ, the true θ_{CMS} of the $\mathrm{B}^0_{\mathrm{sig}}$ and the true value of the boost. This quantity is therefore also only accessible in simulated events. It differs from Δt_{gen}, since both B^0s are not completely at rest in the $\Upsilon(4S)$ frame;

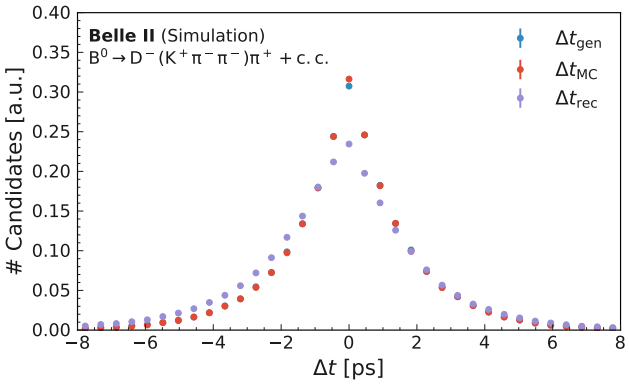

Figure 4.1: Δt_{gen} (blue points), Δt_{MC} (red points) and Δt_{rec} (purple) distributions for simulated $\text{B}^0 \to \text{D}\pi$ events.

- Δt_{rec} is the measured decay time difference computed with Eq. 4.6 using the coordinate ℓ measured from the fitted positions of both B^0 vertices. Compared to the previous quantities, Δt_{rec} is smeared due to the finite detector resolution. This is the only quantity that is also accessible in the real data.

In Fig. 4.1 the different Δt distributions are shown. While the true decay time difference Δt_{gen} and the decay time difference Δt_{MC} calculated using Eq. 4.6 and true values as input differ only slightly, the measured decay time difference Δt_{rec} is visibly smeared. In this analysis, it is approximated that $\Delta t_{\text{gen}} \approx \Delta t_{\text{MC}}$ and in Section 4.1.1 it is explained how the smearing of Δt_{rec} is accounted for to relate Δt_{MC} and the measured Δt_{rec}. Using the approximation shown in Eq. 4.3 and neglecting detector effects, the distribution of positive and negative flavor events as a function of Δt_{gen} follows

$$\begin{aligned} N^{\pm}(\Delta t_{\text{gen}}) &= N \cdot g^{\pm}(\Delta t_{\text{gen}}) \\ &= N \cdot \frac{\exp(-|\Delta t_{\text{gen}}|/\tau)}{4\tau}\{(1 \mp \Delta w) \pm (1-2w) S_f \sin(\Delta m_d \Delta t_{\text{gen}})\} \end{aligned} \tag{4.7}$$

where N is the number of positive/negative flavor events, w is the wrong tag fraction *i.e.* the fraction of the events where the flavor of the B^0_{tag} is wrongly determined, Δw is the difference in wrong tag fraction between a B^0 and a $\overline{\text{B}}^0$ tag, τ is the B^0 lifetime, Δm_d is the mixing frequency and S_f is the time-dependent CP violation parameter. In this analysis, the parameter Δw is neglected and thus assumed to be 0. Under this assumptions, Eq. 4.7 simplifies to

$$N^{\pm}(\Delta t_{\text{gen}}) \approx N \cdot \frac{\exp(-|\Delta t_{\text{gen}}|/\tau)}{4\tau}\{(1 \pm (1-2w) \cdot S_f \cdot \sin(\Delta m_d \Delta t_{\text{gen}})\}. \tag{4.8}$$

In this analysis, the parameters τ and Δm_d are fixed to the average value of previous measurements [33]. The flavor specific decay $B^0 \to D^{\mp}(K^{\pm}\pi^{\mp}\pi^{\mp})\pi^{\pm}$ (hereafter referred to as $B^0 \to D\pi$) is used to determine the wrong tag fraction. The reconstruction and vertex fitting of the two B-mesons in the flavor specific decay is carried out in the same way as for the CP eigenstates. Events are then classified as same flavor (SF) or opposite flavor (OF) events depending on whether the B^0_{sig} and B^0_{tag} have the same flavor or opposite flavor. If CP violation in mixing as well as Δw is neglected, the distributions of SF events N^{SF} and OF events N^{OF} follow [32]

$$\begin{aligned} N^{\text{SF}}(\Delta t_{\text{gen}}) &= N^{\text{SF}} \cdot g^{\text{SF}}(\Delta t_{\text{gen}}) \\ &= N \cdot \frac{\exp(-|\Delta t_{\text{gen}}|/\tau)}{4\tau} \left[1 + (1-2w)\cos(\Delta m_d \Delta t_{\text{gen}})\right] \\ N^{\text{OF}}(\Delta t_{\text{gen}}) &= N^{\text{OF}} \cdot g^{\text{OF}}(\Delta t_{\text{gen}}) \\ &= N \cdot \frac{\exp(-|\Delta t_{\text{gen}}|/\tau)}{4\tau} \left[1 - (1-2w)\cos(\Delta m_d \Delta t_{\text{gen}})\right]. \end{aligned} \tag{4.9}$$

Using N^{SF} and N^{OF} it is possible to define a mixing asymmetry as

$$A_{\text{mix}}(\Delta t_{\text{gen}}) = \frac{N^{\text{SF}} - N^{\text{OF}}}{N^{\text{SF}} + N^{\text{OF}}} = \cos(\Delta m_d \Delta t) \tag{4.10}$$

Therefore, measuring N^{SF} and N^{OF} not only allows to extract w but as a byproduct also allows to determine Δm_d. In the remainder of this section it is first explained in Section 4.1.1 how the distributions $g^{\pm}$ and $g_{\text{eff}}^{\text{SF/OF}}$ depending on $\Delta t_{\text{gen}} \approx \Delta t_{\text{MC}}$ can be related to the measured Δt_{rec} distribution. Then the background considered in this analysis and its treatment is discussed in Section 4.1.2. Finally in Section 4.1.3 the final fit to extract S_f is shown explicitly.

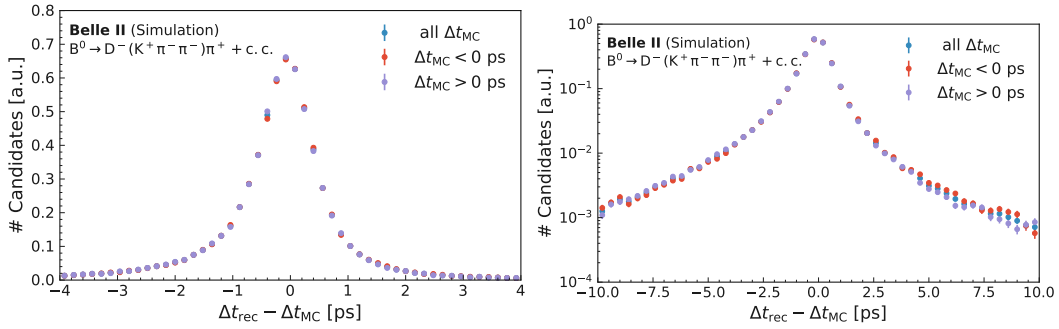

Figure 4.2: $\Delta t_{\text{rec}} - \Delta t_{\text{MC}}$ distribution for simulated $B^0 \to D\pi$ events in linear (left) and logarithmic (right) scale. The distribution is shown for all Δt_{MC} values (blue points), and also for $\Delta t_{\text{MC}} < 0$ (red points) and $\Delta t_{\text{MC}} > 0$ (purple points). Only slight differences between the distributions are observed and neglected for the purpose of this analysis.

4.1.1 Resolution Function

As shown in Fig. 4.1, the measured Δt_{rec} distribution differs from Δt_{gen} and Δt_{MC} due to the finite detector resolution. Therefore, the measured distributions $\mathcal{G}^{\pm}$ (Δt_{rec}) and $\mathcal{G}^{\text{SF/OF}}$ (Δt_{rec}) also differ from the theory distributions described in Eq. 4.7 and Eq. 4.9 which are functions of Δt_{gen}. Under the assumption that $\Delta t_{\text{gen}} \approx \Delta t_{\text{MC}}$, a resolution function $\mathcal{R}(\Delta t_{\text{rec}} - \Delta t_{\text{MC}})$ describing the residual distribution $\Delta t_{\text{res}} = \Delta t_{\text{rec}} - \Delta t_{\text{MC}}$ can be used to relate the measured and the theory distributions. In this section, the resolution function is presented since it is a key ingredient to perform the measurement of $\sin(2\phi_1)$ and Δm_d. However, I would like to emphasize once again that the resolution function was not developed by me, but by other physicists. To relate the measured and theory distributions, $g^{\pm}$ and $g^{\text{SF/OF}}$ are convoluted with the resolution function

$$\begin{aligned} \mathcal{G}^{\text{SF/OF}}(\Delta t_{\text{rec}}) &= (g^{\text{SF/OF}} * \mathcal{R})(\Delta t_{\text{rec}}), \\ \mathcal{G}^{\pm}(\Delta t_{\text{rec}}) &= (g^{\pm} * \mathcal{R})(\Delta t_{\text{rec}}). \end{aligned} \tag{4.11}$$

Two prerequisites need to be fulfilled to be able to relate $g^{\pm}$ and $g^{\text{SF/OF}}$ to the measured distributions via a convolution. First, the shape of $\mathcal{R}(\Delta t_{\text{rec}} - \Delta t_{\text{MC}})$ needs to be independent of Δt_{MC}. Second, the detector acceptance needs to be flat as a function of Δt_{MC}. Checks for both are shown in Fig. 4.2 and in Fig. 4.3.

In this analysis, a 1D resolution function which is a sum of several Gaussian distributions with exponential tails is used. The resolution function contains several Gaussian cores to take the spread of the uncertainty of Δt_{rec}, Δt_{err}, into account. Previous measurements performed by BaBar and Belle used a resolution function

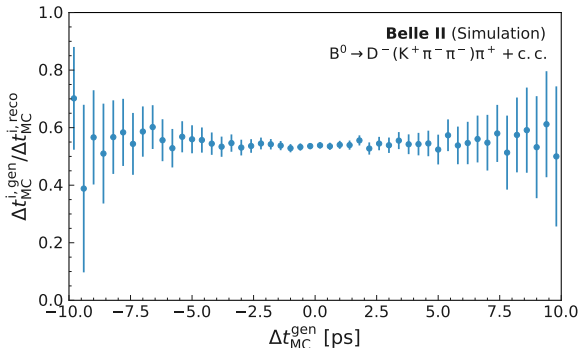

Figure 4.3: To assess whether the acceptance of the detector is flat in Δt_{MC}, $\mathrm{B}^0 \to \mathrm{D}\pi$ events are simulated twice. Once with and once without detector simulation. The Δt_{MC} distributions in both samples, $\Delta t_{\mathrm{MC}}^{\mathrm{reco}}$ in the sample with detector simulation and $\Delta t_{\mathrm{MC}}^{\mathrm{i,gen}}$ in the sample without detector simulation, are then binned and the obtained histograms are divided by each other. The resulting distribution is shown as blue points with errorbars.

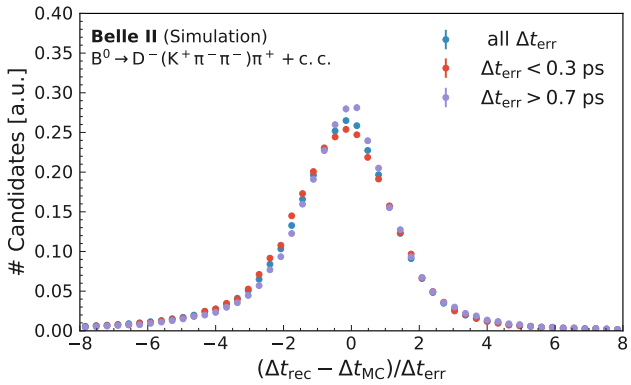

Figure 4.4: Distribution of the Δt_{rec} pull in $\mathrm{B}^0 \to \mathrm{D}\pi$ simulated decays. The pull distribution is shown for all Δt_{err} values (blue points), and also for small ($\Delta t_{\mathrm{err}} < 0.3$ ps) values (red points) and large ($\Delta t_{\mathrm{err}} > 0.7$ ps) values (purple points).

which is conditional on Δt_{err}. In this analysis, the resolution function is not conditional because the pull distribution $(\Delta t_{\text{rec}} - \Delta t_{\text{MC}})/\Delta t_{\text{err}}$ shown in Fig. 4.4 is not constant in bins of Δt_{err} due to for example secondary particles in the B^0_{tag} decay. The exponential tails are added to describe the smearing due to tracks coming from the decay of secondary particles in the B^0_{tag} decay. To be explicit, the following strategy is used to describe the resolution function in all channels of this analysis. First, the Δt_{err} distribution is binned into 18 bins Δt^i_{err} and the fractions of events belonging in each bin f^i_{err} is extracted from a simulation sample. The 18 bins are the same for all channels in this analysis and are shown in Fig. 4.5.

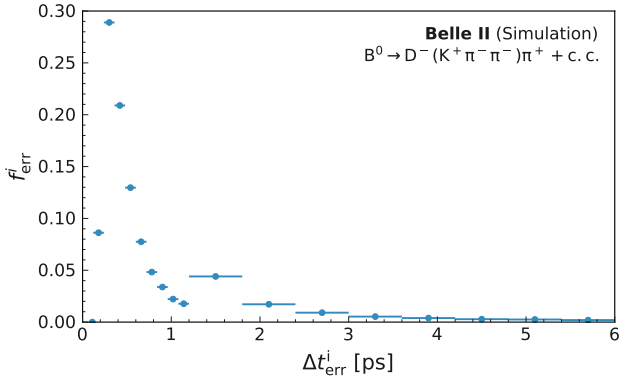

Δt^i_{err} bin edges [ps]				
0.10,	0.12,	0.24,	0.36,	0.48,
0.60,	0.72,	0.84,	0.96,	1.08,
1.20,	1.80,	2.40,	3.00,	3.60,
4.20,	4.80,	5.40,	6.00	

Figure 4.5: Left: fractions of $\text{B}^0 \to \text{D}\pi$ events in the 18 bins of Δt^i_{err} used for the resolution function. Right: corresponding Δt^i_{err} bin edges.

The resolution function is then described as a sum of 18 Gaussian distributions with exponential tails whose mean and width are proportional to Δt^i_{err}:

$$\mathcal{R}(\Delta t_{\text{res}}) = \sum_i f^i_{\text{err}} \cdot \mathcal{R}^i(\Delta t_{\text{res}}), \tag{4.12}$$

with

$$\begin{aligned}\mathcal{R}^i(\Delta t_{\text{res}}) = (1 - r_{\text{tail}}) \cdot G(\Delta t_{\text{res}}, \mu \cdot \Delta t^i_{\text{err}}, \sigma \cdot \Delta t^i_{\text{err}}) \\ + r_{\text{tail}} \cdot r_{\text{R}} \cdot G(\Delta t_{\text{res}}, \mu \cdot \Delta t^i_{\text{err}}, \sigma \cdot \Delta t^i_{\text{err}}) * \exp_R(-c_{\text{R}} \cdot \Delta t_{\text{res}}/\Delta t^i_{\text{err}}) \\ + r_{\text{tail}} \cdot (1 - r_{\text{R}}) \cdot G(\Delta t_{\text{res}}, \mu \cdot \Delta t^i_{\text{err}}, \sigma \cdot \Delta t^i_{\text{err}}) * \exp_L(c_{\text{L}} \cdot \Delta t_{\text{res}}/\Delta t^i_{\text{err}}),\end{aligned} \tag{4.13}$$

where

- $G(\Delta t_{\text{res}}, \mu \cdot \Delta t^i_{\text{err}}, \sigma \cdot \Delta t^i_{\text{err}})$ is the normalized gaussian function of mean $\mu \cdot \Delta t^i_{\text{err}}$ and width $\sigma \cdot \Delta t^i_{\text{err}}$;
- $\exp_R(-c_{\text{R}} \cdot \Delta t_{\text{res}}) = c_{\text{R}} \exp(-c_{\text{R}} \cdot \Delta t_{\text{res}})$ when $\Delta t_{\text{res}} > 0$, 0 otherwise;

- $\exp_L(c_{\rm L} \cdot \Delta t_{\rm res}) = c_{\rm L} \exp(c_{\rm L} \cdot \Delta t_{\rm res})$ when $\Delta t_{\rm res} < 0$, 0 otherwise;
- $r_{\rm tail}$ is the fraction of events belonging to the tails of the distribution;
- $r_{\rm R}$ is the fraction of events in the tails that belong to the right tail.

This resolution function has hence six free parameters in total: μ, σ, $c_{\rm L}$, $c_{\rm R}$, $r_{\rm tail}$, $r_{\rm R}$. For each signal mode, these six parameters, as well as the fractions $f^i_{\rm err}$, are extracted from a fit to the $\Delta t_{\rm res}$ distribution. When fitting the real data, all parameters remain fixed to their values obtained in the simulation. However, to accommodate potential discrepancies between the real data and the simulation in the Δt resolution function, the mean and width of the distribution are shifted and scaled by two parameters, Δ_μ and s_σ, common to all modes, *i.e.*

$$\begin{array}{rcl} \text{simulation} & \rightarrow & \text{real data} \\ \sigma & \rightarrow & s_\sigma \cdot \sigma \\ \mu & \rightarrow & \mu + \Delta_\mu. \end{array} \tag{4.14}$$

In summary, to describe the real data, the signal $B^0 \rightarrow D^- K_S$ $\Delta t_{\rm rec}$ distribution is fitted with

$$\mathcal{G}^{\rm SF/OF}(\Delta t_{\rm rec}; w, \Delta_\mu, s_\sigma) = (g^{\rm SF/OF} * \mathcal{R})(\Delta t_{\rm rec}; w, \Delta_\mu, s_\sigma), \tag{4.15}$$

and the $B^0 \rightarrow J/\psi K_S$ $\Delta t_{\rm rec}$ distribution with

$$\mathcal{G}^{\pm}(\Delta t_{\rm rec}; S_f, w, \Delta_\mu, s_\sigma) = (g^{\pm} * \mathcal{R})(\Delta t_{\rm rec}; S_f, w, \Delta_\mu, s_\sigma), \tag{4.16}$$

where the parameters after the semi-column are free floating in the fit. Other parameters of the resolution function, including the $f^i_{\rm err}$, are fixed to their values found by fitting simulated events. This is possible as the $\Delta t_{\rm err}$ distribution agrees well between data and simulation as shown in the appendix.

To illustrate the impact of the detector effects and the wrong tag fraction w on the measured Δt distribution, in Fig. 4.6 the Δt distribution of simulated $\mathrm{B}^0 \rightarrow \mathrm{D}\pi$ events is shown without detector effects and with $w = 0$. In addition, the Δt distribution is shown without detector effects and with $w = 0.20$ as well as the Δt distribution with detector effects and with $w = 0.20$.

The convolution between $\mathcal{R}$ and the physical distributions $g^{\rm SF/OF}$, $g^{\pm}$ is performed analytically. This convolution heavily relies on the computations in Ref. [34], and its implementation in python software relies on the `scipy.wofz` function [35].

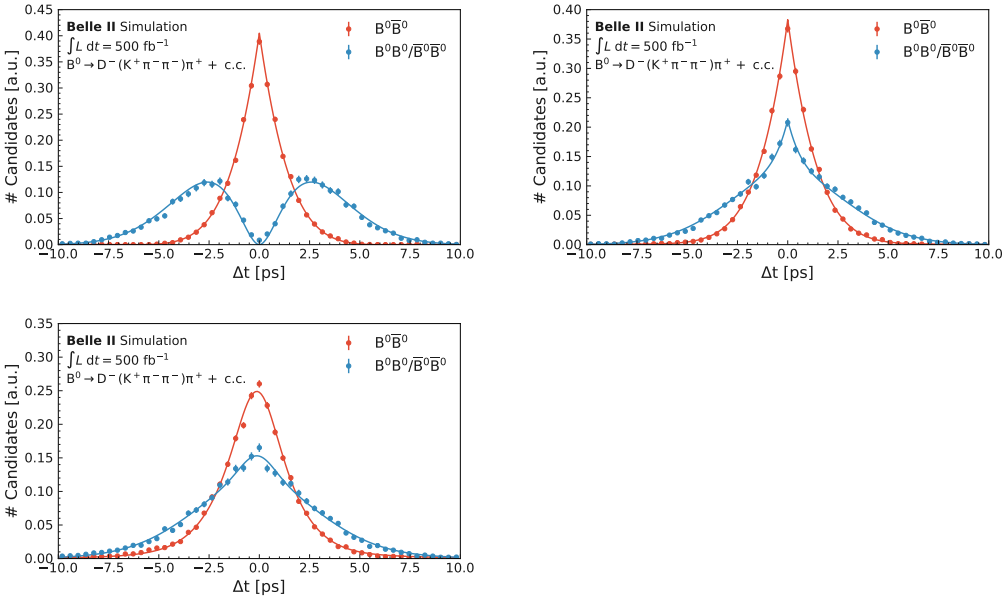

Figure 4.6: Δt distribution without detector effects and $w = 0$ (upper left), Δt distribution without detector effects and $w = 0.20$ (upper right) and Δt (lower left) distribution with detector effects and $w = 0.20$ in simulated $B^0 \to D\pi$ events. The distributions are shown for SF (blue points) and OF (red points) events. The result of the fit for each distribution is superimposed as a solid line in the same color.

4.1.2 Background

Some background events remain after applying the selection discussed in Section 4.3. In this subsection, a description of the main background components surviving the selection is given and it is presented how the background is taken into account in the $\Delta t_{\rm rec}$ fit. In time-dependent CP violation analysis, two standard variables are used to discriminate signal and background. The first is the beam energy-constrained mass, $m_{\rm bc}$, defined as:

$$m_{\rm bc} = \sqrt{(E^*_{\rm beam})^2 - (p^*_B)^2}, \tag{4.17}$$

where $E^*_{\rm beam}$ is half the center of mass energy and $p^*_{\rm B}$ the momentum of the $\rm B^0_{sig}$ candidate in the $\Upsilon(4S)$ frame. In the calculation of $m_{\rm bc}$, the beam energy is used instead of the energy of the $\rm B^0_{sig}$ computed from the momenta of the daughter particles since it is known with higher precision. The second variable is ΔE, defined as:

$$\Delta E = E^*_{\rm B} - E^*_{\rm beam}, \tag{4.18}$$

where $E^*_{\rm beam}$ is half the center of mass energy and $E^*_{\rm B}$ is the energy of the $\rm B^0_{sig}$ candidate computed from the momenta of the daughter particles in the $\Upsilon(4S)$ frame. Both variables peak sharply for fully reconstructed B decays (at zero for ΔE and at the B mass for $m_{\rm bc}$) but have a continuum-like shape for background events. A requirement on $m_{\rm bc}$ is also used to define two regions,

- for $5.27 < m_{\rm bc} < 5.30$ GeV, the signal region (SR) in which $> 99.9\%$ of the correctly reconstructed signal events are situated;
- for $5.20 < m_{\rm bc} < 5.27$ GeV, the sideband region (SB) populated only by background events.

In Fig. 4.7, the $m_{\rm bc}$ distribution for simulated $\rm B^0 \to D\pi$ signal and background events is shown. The $m_{\rm bc}$ distribution of signal events peaks sharply in the signal region while the $m_{\rm bc}$ distribution of $q\overline{q}$ background events is continuum like. The $m_{\rm bc}$ distribution of $\rm B\overline{B}$ background events also has a continuum like shape but contains a small peak in the signal region. The different background components are explained in more detail in Section 4.1.2.1 and Section 4.1.2.2.

4.1.2.1 $q\overline{q}$ Background

The $q\overline{q}$ or continuum background consists of events where $\rm e^+e^- \to q\overline{q}, q = u, d, s, c$. It is the dominant source of background, since most of the tracks in $q\overline{q}$ events come directly from the IP and therefore have a high chance to pass the track selection. For the same reason the $\Delta t_{\rm rec}$ distribution of $q\overline{q}$ background is much thinner than that of the signal. The $q\overline{q}$ $\Delta t_{\rm rec}$ shape can be studied in the SB, since its $m_{\rm bc}$ distribution does not contain a peaking structure but is completely continuum-like.

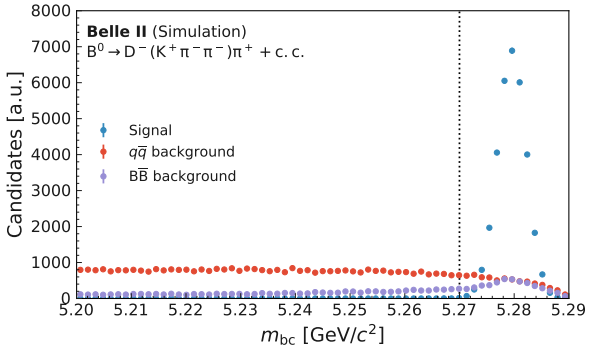

Figure 4.7: The m_{bc} distribution for simulated $\mathrm{B}^0 \to \mathrm{D}\pi$ signal (blue points), $q\overline{q}$ background (red points) and $\mathrm{B}\overline{\mathrm{B}}$ background (purple points) events. The vertical dotted line delimits the sideband region (on the left) from the signal region (on the right).

4.1.2.2 $\mathrm{B}\overline{\mathrm{B}}$ Background

The $\mathrm{B}\overline{\mathrm{B}}$ background consists of events where actual B pairs are created but the $\mathrm{B}^0_{\mathrm{sig}}$ is mis-reconstructed. There are three ways how the reconstruction of the $\mathrm{B}^0_{\mathrm{sig}}$ can fail with different implications for the m_{bc} and Δt_{rec} distributions.
First, the $\mathrm{B}^0_{\mathrm{sig}}$ decays via the signal channel, but the $\mathrm{B}^0_{\mathrm{sig}}$ is wrongly reconstructed. For example in a $\mathrm{B}^0 \to \mathrm{D}^{\mp}(\mathrm{K}^{\pm}\pi^{\mp}\pi^{\mp})\pi^{\pm}$ decay, the $\mathrm{K}^{\pm}$ is reconstructed as $\pi^{\pm}$ and the $\pi^{\pm}$ as $\mathrm{K}^{\pm}$. Events like this are also called self cross-feed (scf) events.
Scf events are actual signal events, but are grouped into the background due to the simplicity of this analysis.
Second, the $\mathrm{B}^0_{\mathrm{sig}}$ decays via a different decay channel than the signal channel and at least one daughter particle of the $\mathrm{B}^0_{\mathrm{sig}}$ is misidentified. For example $\mathrm{B}^0 \to \mathrm{DK}$ decays with the K misidentified as π are a sizable background for the $\mathrm{B}^0 \to \mathrm{D}\pi$ channel. This background contains a peaking structure, since it contains a fully reconstructed B, and is therefore also called peaking background. The Δt_{rec} distribution is similar to the distribution of signal events.
Third, in the reconstruction tracks from the $\mathrm{B}^0_{\mathrm{tag}}$ decay are wrongly assigned to the $\mathrm{B}^0_{\mathrm{sig}}$. This background is called combinatorial background throughout this thesis. Its m_{bc} distribution is continuum-like and the Δt_{rec} distribution is thinner than the distribution of signal events, since it is no longer possible to differentiate between the $\mathrm{B}^0_{\mathrm{tag}}$ and $\mathrm{B}^0_{\mathrm{sig}}$ vertex.
Due to the simplicity of this analysis, the different $\mathrm{B}\overline{\mathrm{B}}$ components are grouped together into one background category. In a precision measurement, the different components will need to be analyzed independently, since their Δt_{rec} distributions

differ. In Section 4.7, several systematic uncertainties related to the $B\overline{B}$ background are discussed to account for this simplistic treatment.

4.1.2.3 Background Treatment

For each channel, signal and background $m_{\rm bc}$ shapes are extracted by fitting a probability density function (pdf) to simulation samples containing only one particular component. For the $B^0 \to D\pi$ channel individual shapes for the $q\overline{q}$ and $B\overline{B}$ backgrounds are extracted. For the $B^0 \to J/\psi\ K_S$ channels only one shape describing both background components together is extracted since most ($\approx 80\%$) of the background events are $q\overline{q}$ events and due to the low overall expected number of background events in the SR. In the fit to data, the parameters of the shapes are fixed to the values obtained in the simulation, but as for the resolution function, a shift parameter $\Delta_{m_{\rm bc}}$ common to all shapes is introduced to account for data-simulation discrepancies. The parameter shifts the mean of the shapes. The used pdfs and obtained shapes are described in more detail in Section 4.4.1

4.1.3 Combined fit strategy

The fit to extract $\sin(2\phi_1)$ is an extended maximum likelihood fit performed simultaneously on all channels. It is a 2D $m_{\rm bc}; \Delta t_{\rm rec}$ fit in the $m_{\rm bc}$ SR and a 1D $m_{\rm bc}$ fit in the $m_{\rm bc}$ SB. To be explicit, the function $\mathcal{L}_{\rm tot}$ that is minimized reads

$$\mathcal{L}_{\rm tot} = \sum_c -2\left(L_c + \log(N^c_{\rm sig} + N^c_{\rm bkg})\right), \tag{4.19}$$

where $N^c_{\rm sig}$ and $N^c_{\rm bkg}$ are the signal and background yields for the channel c (c runs over $B^0 \to J/\psi\ K_S$ positive and negative flavor events, and $B^0 \to D\pi$ SF and OF). For the extraction of Δm_d only the $B^0 \to D\pi$ sample is fitted (c then runs only over $B^0 \to D\pi$ SF and OF). The function L_c is a log likelihood that takes as input the data events i characterized by their coordinates $\Delta t_{{\rm rec}^i}; m^i_{\rm bc}$,

$$\begin{aligned} L_c = & \sum_{i\in {\rm c,\ SR}} \log\big[N^{\rm c}_{\rm sig}\cdot f^{\rm SR}_{\rm sig}\cdot \mathcal{G}^{\rm c}_{\rm sig}(\Delta t_{{\rm rec}^i}; w, (s_f), s_{\Delta {\rm t}}, \Delta_{\Delta {\rm t}})\cdot h^{\rm c}_{\rm sig}(m^i_{\rm bc}; \Delta_{m_{\rm bc}}) \\ & \qquad + N^{\rm c}_{\rm bkg}\cdot f^{\rm SR}_{\rm bkg}\cdot \mathcal{G}^{\rm c}_{\rm bkg}(\Delta t_{{\rm rec}^i}; s_{\Delta {\rm t}}, \Delta_{\Delta {\rm t}})\cdot h^{\rm c}_{\rm bkg}(m^i_{\rm bc}; \Delta_{m_{\rm bc}})\big] \\ & + \sum_{i\in {\rm c,\ SB}} \log\big[N^{\rm c}_{\rm sig}\cdot(1-f^{\rm SR}_{\rm sig})\cdot h^{\rm c}_{\rm sig}(m^i_{\rm bc}; \Delta_{m_{\rm bc}})\big] \\ & \qquad + N^{\rm c}_{\rm bkg}\cdot(1-f^{\rm SR}_{\rm bkg})\cdot h^{\rm c}_{\rm bkg}(m^i_{\rm bc}; \Delta_{m_{\rm bc}})\big]\,, \end{aligned} \tag{4.20}$$

where

- the superscripts SR (SB) indicate a quantity relative to the signal region (sideband);
- $\mathcal{G}^{\rm c}_{\rm sig}$ ($\mathcal{G}^{\rm c}_{\rm bkg}$) is the signal (background) $\Delta t_{\rm rec}$ shape for channel c;
- $h_{\rm sig}$ ($h_{\rm bkg}$) is the signal (background) $m_{\rm bc}$ shape;
- $f^{SR}_{\rm sig}$ ($f^{\rm SR}_{\rm bkg}$) is the fraction of signal (background) events belonging to the signal region. It is not a free parameter, but it is computed from the integral of $h_{\rm sig}$ ($h_{\rm bkg}$) over the appropriate $m_{\rm bc}$ range.

4.2 Data Sets

In this analysis a data sample with an integrated luminosity of 34.6 fb^{-1} is used. For the two CP eigenstate channels and the flavor specific channel signal simulation samples with respectively 1 million and 2 million events are generated. For the background study generic simulations samples, containing $q\overline{q}, q = u, d, s, c$, $B^0\overline{B^0}$, B^+B^- and $\tau^+\tau^-$ components with an integrated luminosity of 500 fb^{-1} are used. The signal simulation samples are listed in Tab. 4.1 and the generic simulation samples are summarized in Tab. 4.2.

Table 4.1: Signal simulation samples used in this analysis.

Sample	Number of events [10^6]
$B^0 \to J/\psi(\to e^+e^-)K_S$	1
$B^0 \to J/\psi(\to \mu^+\mu^-)K_S$	1
$B^0 \to D\pi$	2

Table 4.2: Generic simulation samples used in this analysis.

Sample	Equivalent luminosity [fb^{-1}]
$u\overline{u}$	500
$d\overline{d}$	500
$c\overline{c}$	500
$s\overline{s}$	500
$B^0\overline{B^0}$	500
B^+B^-	500
$\tau^+\tau^-$	500

4.3 Reconstruction and Selection

In this section the selection applied to the different decay channels is presented. To suppress background tracks not coming from the IP, charged tracks are selected by applying a requirement on the transverse distance of the origin of the tracks with respect to the IP of dr < 0.5 cm and a requirement on the z position of the origin of the tracks with respect to the IP of $|\mathrm{dz}| < 3$ cm. In addition, tracks are required to be within the acceptance of the CDC. Tracks that are reconstructed as $\pi^{\pm}$ originating from a $\mathrm{K_S^0}$ decay are not required to fulfill these requirements, since they do not originate from the IP. In addition, tracks reconstructed as $\mathrm{K}^{\pm}$ are required to satisfy a loose kaonID requirement of kaonID > 0.01 and tracks reconstructed as leptons a loose cut on their respective leptonID of leptonID > 0.01. The cleaned tracks are used to reconstruct composite particles. After the particles are reconstructed a further selection is applied to reduce remaining background events, and to remove events with poor flavor tagger information or a bad vertex fit. In Tab. 4.3 this selection is summarized.

A cut on the reduced Foxram Wolfram moment [36] of $R_2 < 0.4$ is applied for all channels to remove combinatorial background. The reduced Foxram Wolfram moment describes the event shape of final states in $\mathrm{e^+\,e^-}$ annihilation. To supress combinatorial background and partially reconstructed B decays, a $|\Delta E| < 0.05$ GeV cut is placed for the channels without electrons. For the $\mathrm{B^0 \to J/\psi(\to e^+e^-)K_S}$ channel, a J/ψ-mass constrained ΔE_{ctr} variable is used, $|\Delta E_{\mathrm{ctr}}| < 0.04$ GeV. The ΔE_{ctr} variable is calculated by subtracting the measured mass of the J/ψ from ΔE and adding the nominal value of the J/ψ. This is done for the $\mathrm{B^0 \to J/\psi(\to e^+e^-)K_S}$ channel since the electrons loose a lot of energy due to bremstrahlung which is currently not well described in the simulation. To remove events with poor flavor information, a cut on the flavor tagger quality $|qr| > 0.2$ is applied. Requirements on the p-value of the signal and tag vertices, p-val(tag) $> 1\%$ and p-val(sig) > -1, are placed to remove failed vertex fits. A cut $0.1 < \Delta t_{\mathrm{err}} < 6.0$ ps is applied to remove events with a too large uncertainty on Δt_{rec} or a failed computation of Δt_{err}[1]. To supress prompt combinatorial events for the $\mathrm{B^0 \to J/\psi(\ell\ell)K_S}$ channels, a cut is placed on the radial distance of the $\mathrm{K_S}$, dr($\mathrm{K_S}$). J/ψ and $\mathrm{K_S}$ mass window requirements are also applied.

After all cuts, small peaking backgrounds stemming from $\mathrm{B^0 \to \eta_c(\pi^-\pi^+)K_S}$ and $\mathrm{B^0 \to D^-(K_S\pi^-)\pi^+}$, where two pions are mis-identified for leptons, remain. To suppress these backgrounds a di-lepton mass veto with a lepton to pion mass hypothesis switch, $m_{\ell\to\pi}(\ell\ell) > 3.05$ GeV, and a $\mathrm{K_S}\ell$ mass with a lepton to pion mass hypothesis switch, $m_{\ell^{\pm}\to\pi^{\pm}}(\mathrm{K_S}\ell^{\pm}) \notin (1.85,\ 1.89)$ GeV is applied. In the $\mathrm{B^0 \to\ D}\pi$

[1] In the current implementation of Rave, sometimes during fitting the weights of all tracks are set to 0 *i.e.* all tracks are ignored. In this case the p-value is very low and Δt_{err} is 0. This justifies the $\Delta t_{\mathrm{err}} > 0.1$ ps and p-val(tag) $> 1\%$ cuts.

Table 4.3: Final applied selection requirements.

all channels		
$\lvert qr\rvert$	$>$	0.2
R_2	$<$	0.4
Δt_{err}	$>$	0.1 ps
	$<$	6.0 ps
p-val(tag)	$>$	1%
p-val(sig)	$>$	-1
m_{bc}	$\in$	(5.2, 5.3) GeV

$\mathrm{B^0} \to \mathrm{J/\psi(\to \ell\ell)K_S}$			$\mathrm{B^0} \to \mathrm{D\pi}$		
$m_{\mu\to\pi}(\ell\ell)$	$>$	3.05 GeV	$\lvert\Delta E\rvert$	$<$	0.05 GeV
$m_{\mu^\pm\to\pi^\pm}(\mathrm{K_S}\ell^\pm)$	$\notin$	(1.85, 1.89) GeV	$m(\mathrm{D})$	$\in$	(1.844, 1.894) GeV
$m(\pi\pi)$	$\in$	(0.47, 0.53) GeV	$\mathrm{ID_K}(\pi_\mathrm{B})$	$<$	0.5
$\mathrm{dr(K_S)}$	$>$	0.6 cm	$\mathrm{ID_K(K)}$	$>$	0.4
$\mathrm{B^0} \to \mathrm{J/\psi(\to \mu^+\mu^-)K_S}$					
$\lvert\Delta E\rvert$	$<$	0.05 GeV			
$m(\mu\mu)$	$\in$	(3.00, 3.15) GeV			
$\mathrm{ID_\mu}(\mu^+)$ or $\mathrm{ID_\mu}(\mu^-)$	$>$	0.2			
$\mathrm{B^0} \to \mathrm{J/\psi(\to e^+e^-)K_S}$					
$\lvert\Delta E_{\mathrm{ctr}}\rvert$	$<$	0.04 GeV			
$m(\mathrm{ee})$	$\in$	(2.90, 3.15) GeV			
$\mathrm{ID_e}(\mathrm{e}^+)$ or $\mathrm{ID_e}(\mathrm{e}^-)$	$>$	0.2			

channel, peaking background stemming from $\mathrm{B^0} \to \mathrm{D^-K^+}$ remains. This background is suppressed by placing a D mass window cut and a PID requirement on the kaon $\mathrm{ID_K(K)} > 0.4$.

4.4 Fit Shapes from the Simulation

In this section, the signal and background $m_{\rm bc}$ and $\Delta t_{\rm rec}$ shapes are extracted using the simulation samples. The shapes are extracted by fitting the $m_{\rm bc}$ and $\Delta t_{\rm rec}$ distribution of the different signal and background samples individually. In the final fits to extract S_f and Δm_d, described in Section 4.1.3, the obtained shapes are used as an input. The individual shapes are then fixed to the shapes extracted by the fits to the simulation samples. Only the yield, the wrong tag fraction w and the time dependent CP violation parameter S_f as well as shift and scale parameter that shift and scale the shapes to account for data-simulation discrepancies are free parameter in the final fits to the real data. Figuratively, the $m_{\rm bc}$ shapes are used to determine the number of signal and data events in the real data. The $\Delta t_{\rm rec}$ shapes are necessary to extract S_f and Δm_d as described in Section 4.1. Since the final fits are 2D in $m_{\rm bc}; \Delta t_{\rm rec}$, the uncertainty of the signal and background yields is directly propagated to the physics parameter.

4.4.1 $m_{\rm bc}$ shapes

In this section, the signal and background $m_{\rm bc}$ shapes are extracted. The extraction is carried out in two steps. First, probability density functions are used to fit the signal and background simulation samples individually. Then the extracted shapes are used to fit the whole generic simulation sample. In the later fit, all shapes are fixed to the shapes obtained by the previous fits. Only the yields of the different shapes are free floating. It is checked whether the obtained yields for the different signal and background components agree with the true simulation values.

4.4.1.1 Fits for $B^0 \to D\pi$ events

A Crystal Ball pdf CB is used to fit the signal $m_{\rm bc}$ distribution [37]. The Crystal Ball function consists of a Gaussian core with a power-law tail. It is parameterized as

$$\mathrm{CB}(x,\alpha,n,\overline{x},\sigma) = N \cdot \begin{cases} \exp(-\frac{(x-\overline{x})^2}{2\sigma^2}), & \text{for } x > -\beta \\ A(B - \frac{(x-\overline{x})^2}{2\sigma^2})^{-n}, & \text{for } x \leq -\beta \end{cases}, \tag{4.21}$$

where $A = (n/\alpha)^n \cdot \exp(-\alpha^2/2)$, $B = n/|\alpha| - |\alpha|$ and N is a normalization constant. The fit to the simulated signal sample as well as the fit parameters are shown in Fig. 4.8.

For the $q\overline{q}$ background an Argus function Ar is used [38]. The Argus function is

parameterized for $0 < x < 1$ as

$$\mathrm{Ar}(x, \chi, x_0, m_0) = \frac{\chi^3}{\sqrt{2\pi}\psi(\chi)} \frac{(x - x_0)}{m_0} \sqrt{1 - \frac{(x - x_0)^2}{m_0^2}} \exp(-\chi^2(1 - \frac{(x - x_0)^2}{m_0^2})/2), \tag{4.22}$$

where $\Psi(\chi) = \Phi(\chi) - \chi\phi(\chi) - 1/2$, with Φ being the cumulative distribution function (cdf) of the standard normal distribution and ϕ being the pdf of the standard normal distribution. For the different Argus pdfs used throughout this thesis, m_0 is fixed to half the beam energy. The fit to the simulated $q\overline{q}$ background sample as well as the fit parameters is shown in Fig. 4.9.

The $\mathrm{B\overline{B}}$ background m_{bc} distribution is fitted with the sum of an Argus and Crystal Ball with the portion of the Crystal Ball, f_{CB}, left free floating in the fit,

$$f(x, f_{\mathrm{CB}}) = (1 - f_{\mathrm{CB}}) \cdot \mathrm{Ar} + f_{\mathrm{CB}} \cdot \mathrm{CB}. \tag{4.23}$$

The fit to the simulated $\mathrm{B\overline{B}}$ background sample as well as the fit parameters are shown in Fig. 4.10.

For the fit to the combined simulation sample shown in Fig. 4.11 the shapes of the different components are fixed to the shapes extracted by the fits to the dedicated component. In addition, the fraction of events between $q\overline{q}$ and $\mathrm{B\overline{B}}$ background is fixed to the true simulation value. Otherwise the $\mathrm{B\overline{B}}$ background component tends to be underestimated by the fit. In Section 4.7, a systematic uncertainty for the fixed $q\overline{q}$ and $\mathrm{B\overline{B}}$ background fraction is calculated. The combined fit has two free parameters, the signal and background yield. The yields obtained by the fit agree well with the true simulation values.

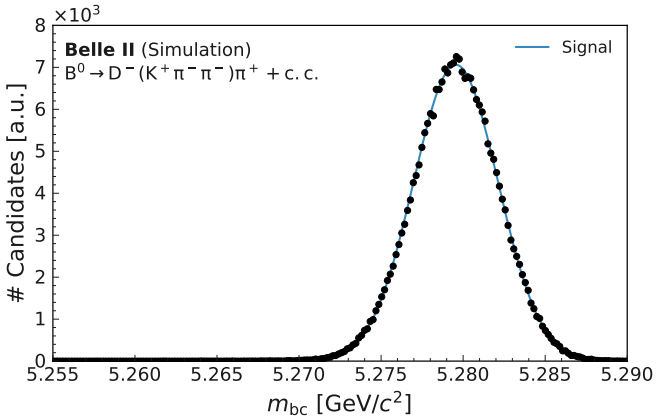

Parameter	Value	Error
α	2.682	0.036
n	9.83	0.13
$\overline{x}$ [GeV]	5.27955	$5.1{\cdot}10^{-6}$
σ [MeV]	2.5664	0.0038
yield	259930	500

Figure 4.8: Top: m_{bc} distribution of simulated $\mathrm{B}^0 \to \mathrm{D}\pi$ events (black points). The result of a fit using a Crystal Ball function is shown as blue line. Bottom: corresponding fit parameters.

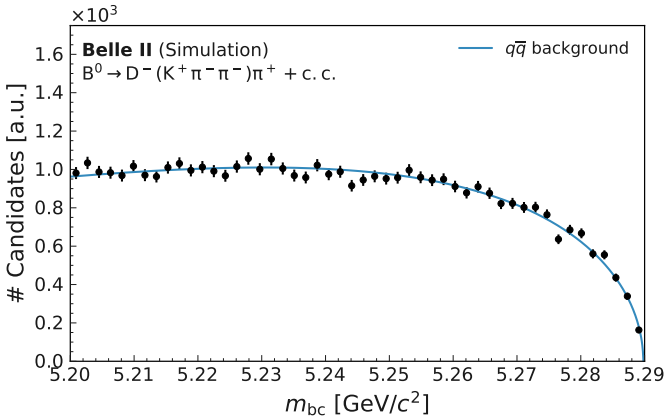

Parameter	Value	Error
χ	6.614	0.080
x_0 [MeV]	0.012	0.026
yield	44160	210

Figure 4.9: Top: m_{bc} distribution of simulated $q\bar{q}$ background events (black points) for $B^0 \to D\pi$. The result of a fit using an Argus function is shown as blue line. Bottom: corresponding fit parameters.

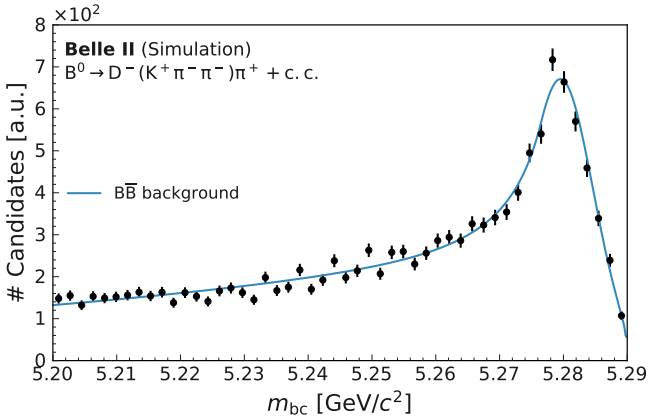

Parameter	Value	Error
α	0.675	0.077
n	1.110	0.028
$\overline{x}$ [GeV]	5.27968	0.00017
σ [GeV]	0.00476	0.00015
χ	8.70	0.63
x_0 [MeV]	-0.09	0.18
CrystalFrac	0.649	0.078
yield	12750	110

Figure 4.10: Top: m_{bc} distribution of simulated $B\overline{B}$ background events (black points) for $B^0 \to D\pi$. The result of a fit using a Crystal Ball + Argus function is shown as blue line. Bottom: corresponding fit parameters.

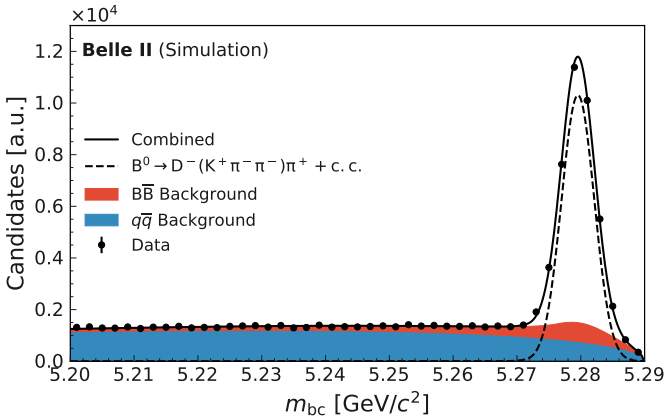

Component	Yield	Error	Expected
Signal	33180	210	32800
Background	58550	260	56910

Figure 4.11: Top: m_{bc} distribution of simulated $\mathrm{B}^0 \to \mathrm{D}\pi$ candidates (black points). The total fit is shown as solid black line. The different components of the fit are shown as dashed line (signal), filled blue area ($q\overline{q}$ background) and filled red area ($\mathrm{B}\overline{\mathrm{B}}$ background). Bottom: Corresponding fit parameters.

4.4.1.2 m_{bc} shapes for the SF and OF sample

It is checked whether the m_{bc} shapes for $\mathrm{B}^0 \to \mathrm{D}\pi$ same flavor and opposite flavor events differ. The result is shown in Figure 4.12. No significant difference between the same flavor and opposite flavor m_{bc} shape is observed. This reassures that it is not necessary to extract separate m_{bc} shapes for both populations.

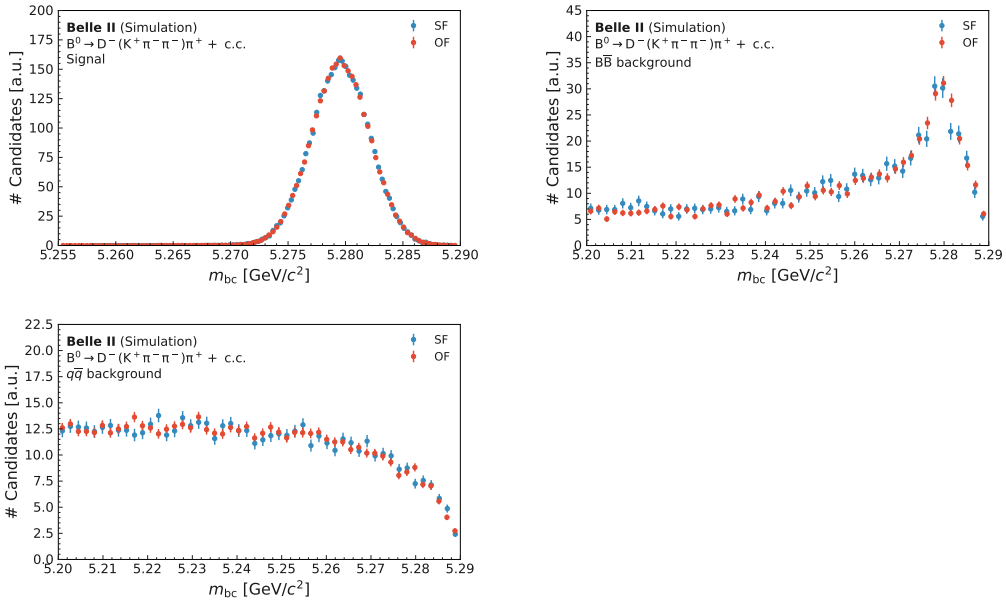

Figure 4.12: Comparison between the m_{bc} shape of SF (blue dots) and OF (red dots) events for the signal (upper left), $\mathrm{B\overline{B}}$ background (upper right) and $q\overline{q}$ background (lower left) component of the $\mathrm{B}^0 \to \mathrm{D}\pi$ sample. The SF and OF shapes have been normalised to the same event number. No significant difference between the SF and OF shape can be observed.

4.4.1.3 Fits for $\mathrm{B}^0 \to \mathrm{J/\psi}(\to \mu^+\mu^-)\mathrm{K_S}$ events

A Crystal Ball function is used for the signal component of the $\mathrm{B}^0 \to \mathrm{J/\psi}(\to \mu^+\mu^-)\mathrm{K_S}$ channel. The fit is shown in Fig. 4.13.

As mentioned in Section 4.1.2, the shapes of the $\mathrm{B\overline{B}}$ and $q\overline{q}$ background are extracted together due to the low expected number of background events in the data sample. An Argus and a Gaussian pdf with the portion of the Gaussian, f_{Gaus}, left free floating is used in the background fit,

$$\mathrm{Ar}(x, \chi, x_0, m_0) = (1 - f_{\mathrm{Gaus}}) \cdot \mathrm{Ar} + f_{\mathrm{Gaus}} \cdot \phi. \tag{4.24}$$

The fit is shown in Fig. 4.14.

The fit to the combined simulation sample is shown in Fig. 4.15. For the combined fit, the shapes of the different components are fixed to the shapes extracted by the fits to the dedicated component. The signal and background yields are the free parameters for this fit. The yields found by the fit agree well with the true simulation values.

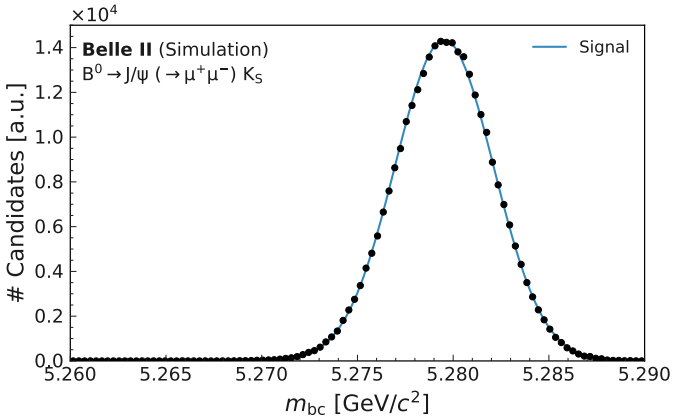

Parameter	Value	Error
α	3.077	0.024
n	3.65	0.14
$\overline{x}$ [GeV]	5.27953	$4.7{\cdot}10^{-6}$
σ [MeV]	2.5754	0.0034
yield	308800	560

Figure 4.13: Top: m_{bc} distribution of simulated signal events (black points) for $\mathrm{B}^0 \to \mathrm{J}/\psi(\to \mu^+\mu^-)\mathrm{K_S}$. The result of a fit using a Crystal Ball function is shown as blue line. Bottom: corresponding fit parameters.

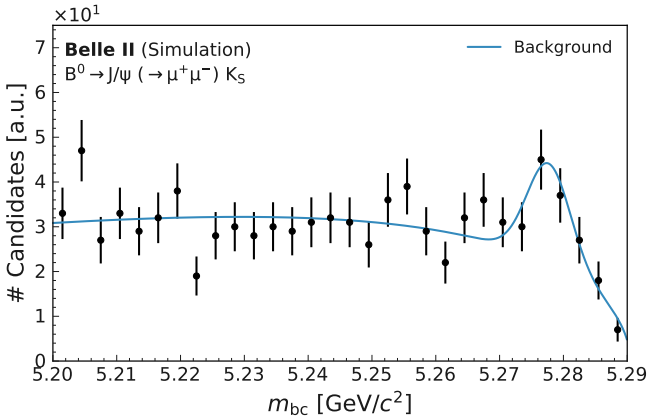

Parameter	Value	Error
χ	6.52	0.81
x_0 [MeV]	0.7	1.1
μ [GeV]	5.27771	0.00090
σ [MeV]	3.39	0.97
fracGaus	0.0220	0.0061
yield	912	30

Figure 4.14: Top: m_{bc} distribution of simulated background events (black points) for $\mathrm{B}^0 \to \mathrm{J}/\psi(\to \mu^+\mu^-)\mathrm{K_S}$. The result of a fit using an Argus + Gaussian function is shown as blue line. Right: corresponding fit parameters.

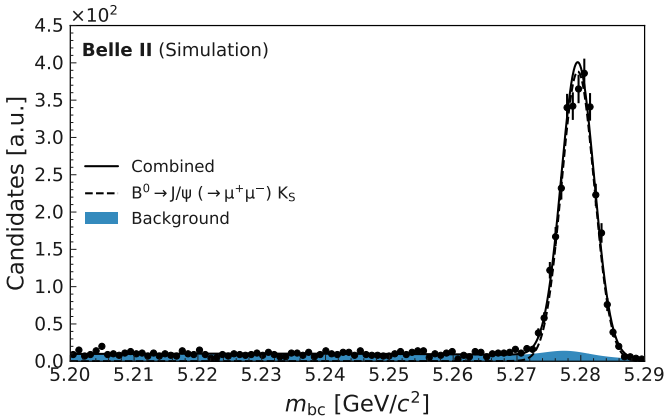

Component	Yield	Error	Expected
Signal	2786	55	2784
Background	966	33	912

Figure 4.15: Top: m_{bc} distribution of simulated $\mathrm{B}^0 \to \mathrm{J}/\psi(\to \mu^+\mu^-)\mathrm{K_S}$ candidates (black points). The total fit is shown as solid black line. The different components of the fit are shown as dashed line (signal) and filled blue area (background). Bottom: Corresponding fit parameters.

4.4.1.4 Fits for $B^0 \to J/\psi(\to e^+e^-)K_S$ events

For the $B^0 \to J/\psi(\to e^+e^-)K_S$ channel the same pdfs as for the $B^0 \to J/\psi(\to \mu^+\mu^-)K_S$ are used. The fit to the signal sample is shown in Fig. 4.16 and the fit to the background sample is shown in Fig. 4.17. The yields found by the fit to the combined sample shown in Fig. 4.18 agree well with the true simulation values.

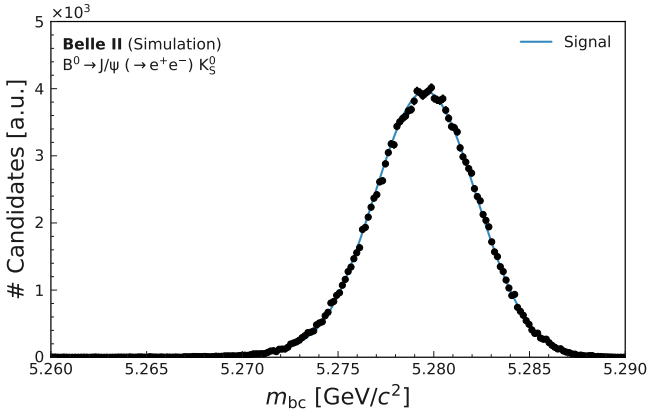

Parameter	Value	Error
α	1.922	0.047
n	14.1	3.0
$\overline{x}$ [GeV]	5.27956	$7.2{\cdot}10^{-6}$
σ [MeV]	2.6689	0.0057
yield	178040	420

Figure 4.16: Top: m_{bc} distribution of simulated signal events (black points) for $B^0 \to J/\psi(\to e^+e^-)K_S$. The result of a fit using a Crystal Ball function is shown as blue line. Bottom: corresponding fit parameters.

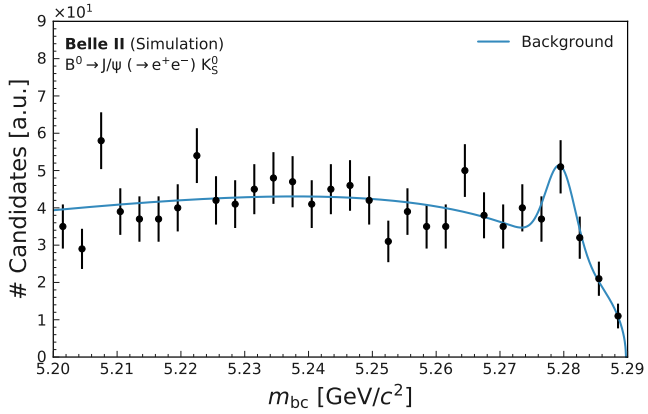

Parameter	Value	Error
χ	7.08	0.52
x_0 [MeV]	-0.05	0.25
μ [GeV]	5.2795	0.00075
σ [MeV]	2.27	0.80
fracGaus	0.0134	0.0044
yield	1181	33

Figure 4.17: Top: m_{bc} distribution of simulated background events (black points) for $B^0 \to J/\psi(\to e^+e^-)K_S$. The result of a fit using an Argus + Gaussian function is shown as blue line. Bottom: corresponding fit parameters.

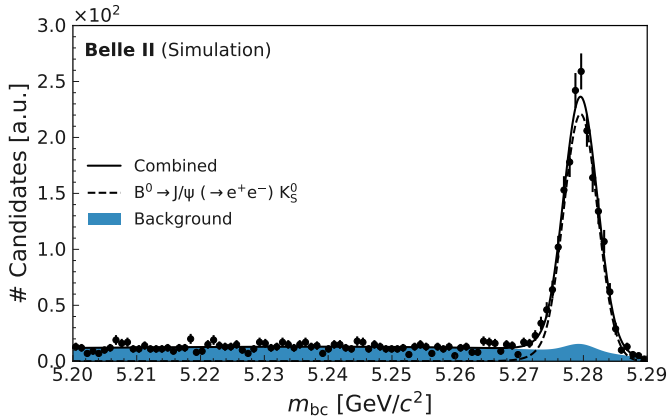

Component	Yield	Error	Expected
Signal	1656	43	1664
Background	1190	38	1181

Figure 4.18: Top: m_{bc} distribution of simulated $\mathrm{B}^0 \to \mathrm{J}/\psi(\to \mathrm{e}^+\mathrm{e}^-)\mathrm{K_S}$ candidates (black points). The total fit is shown as solid black line. The different components of the fit are shown as dashed line (signal) and filled blue area (background). Bottom: Corresponding fit parameters.

4.4.2 Δt_{rec} shapes

In this section, the Δt_{rec} (residual) distributions of the signal and background simulation samples are fitted using the resolution function described in Section 4.1.1. The obtained shapes of the resolution function are used as an input for the final fit described in Section 4.1.3.

4.4.2.1 $B^0 \to J/\psi\ K_S$ signal resolution function

The result of the fit to the Δt_{rec} residual distribution of events in the signal simulation $B^0 \to J/\psi\ K_S$ samples with the resolution function given by Eq. 4.13 is shown in Fig. 4.19 together with the obtained values of the fitted parameters. The fit describes the data reasonably well. Some differences between the fit and the data are observable in the right tail, but these differences do not have a relevant impact on the fit to the real data since the expected number of events in the real data sample is three orders of magnitude lower than number of events in the simulation. Due to the displacement of secondary particles coming from the B^0_{tag}, the width σ of the Gaussian cores is significantly larger than 1.0.

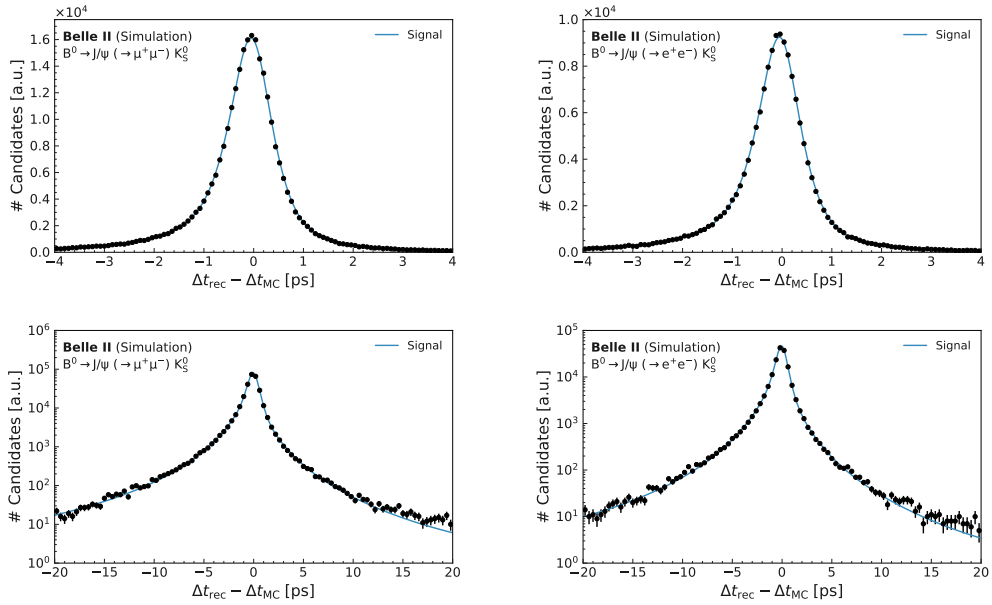

Parameter	Value	Error
μ	-0.1492	0.0078
σ	1.3546	0.0077
c_R	0.2864	0.0098
c_L	0.2835	0.0049
r_{tail}	0.2812	0.0063
r_R	0.2749	0.0090

Parameter	Value	Error
μ	-0.155	0.011
σ	1.360	0.011
c_R	0.301	0.013
c_L	0.2865	0.0068
r_{tail}	0.2864	0.0090
r_R	0.287	0.012

Figure 4.19: Top Left (Right): Δt_{rec} residual distribution of simulated $B^0 \to J/\psi(\to \mu^+\mu^-)K_S$ ($B^0 \to J/\psi(\to e^+e^-)K_S$) signal events shown as black points with error bars. The result of the fit is shown as solid blue line. Middle Left (Right): same than Top Left (Right) but in logarithmic scale. Bottom Left (Right): shape parameters obtained from the fit.

4.4.2.2 $B^0 \to J/\psi K_S$ background Δt_{rec} shape

The result of the fit to the $\Delta t_{\rm rec}$ distribution of events in the background simulation $B^0 \to J/\psi\ K_S$ samples is shown in Fig. 4.20. For the fit, the finite effective lifetime of the background events is neglected. This is possible, even though $B\overline{B}$ background events have a finite effective lifetime, because the number of $B\overline{B}$ background events is very low (the $B\overline{B}$ background is $\approx 20\%$ of the total background). Neglecting the lifetime allows to use the resolution function as shape for the fit. The background is divided into four populations, sideband region, signal region, positive and negative flavor events. Due to the low number of background events, it is sufficient to use the the same $\Delta t_{\rm rec}$ shape for all populations. The fit is performed once for all four background populations combined. The value of the width σ of the Gaussian cores obtained by the fit is significantly larger than for the signal. This is interpreted as coming from background events with a finite lifetime that widen the distribution.

4.4.2.3 $B^0 \to D\pi$ signal resolution function

The result of the fit to the $\Delta t_{\rm rec}$ residual distribution of events in the signal simulation $B^0 \to D\pi$ sample with the resolution function given by Eq. 4.13 is shown in Fig. 4.21 together with the obtained values for the fit parameters. As for the fit to the $B^0 \to J/\psi\ K_S$ samples, the fit is good overall but some discrepancies between the data and the fit function are observable in the right tail. Again, the fit function is deemed to work reasonably well considering that the expected number of events in the real data is two orders of magnitude lower than the number of events in the simulation sample.

In Fig. 4.22 the $\Delta t_{\rm err}$ distribution and the residual distribution for simulated signal $B^0 \to D\pi$ same flavor and opposite flavor events are shown. The resolution function is superimposed to the residual distribution. Its parameters have their values fixed to the ones shown in Fig. 4.21, but the $f^i_{\rm err}$ values are extracted from the SF and OF samples separately. The resolution function describes the SF and OF residuals well without the need to update its shape parameters, although some differences are visible between the residual distributions for SF and OF events. The differences between the SF and OF is understood to stem from the fact that the SF sample is smaller than the OF sample and the fraction of events with a poorly reconstructed tag vertex is therefore higher.

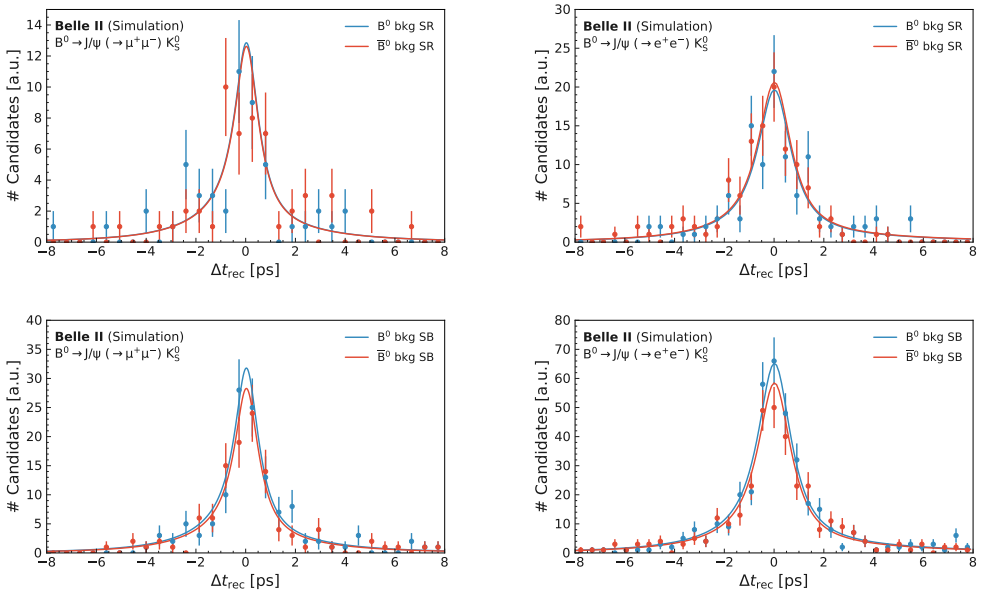

Parameter	Value	Error
μ	0.21	0.25
σ	1.21	0.29
c_R	0.198	0.068
c_L	0.287	0.071
r_{tail}	0.59	0.16
r_R	0.389	0.099

Parameter	Value	Error
μ	0.16	0.21
σ	1.88	0.19
c_R	0.101	0.033
c_L	0.210	0.051
r_{tail}	0.431	0.079
r_R	0.424	0.088

Figure 4.20: Top Left (Right): Δt_{rec} distribution of simulated $B^0 \to J/\psi(\to \mu^+\mu^-)K_S$ ($B^0 \to J/\psi(\to e^+e^-)K_S$) background events in the SR. The Δt_{rec} distribution of positive (negative) flavor events is shown as red (blue) points. Middle Left (Right): same as Top Left (Top Right), but in the SB. The result of a simultaneous fit to the SR and SB distributions is shown in corresponding colors. Bottom Left (Right): fit parameters for the fit to all $B^0 \to J/\psi(\to \mu^+\mu^-)K_S$ ($B^0 \to J/\psi(\to e^+e^-)K_S$) background events.

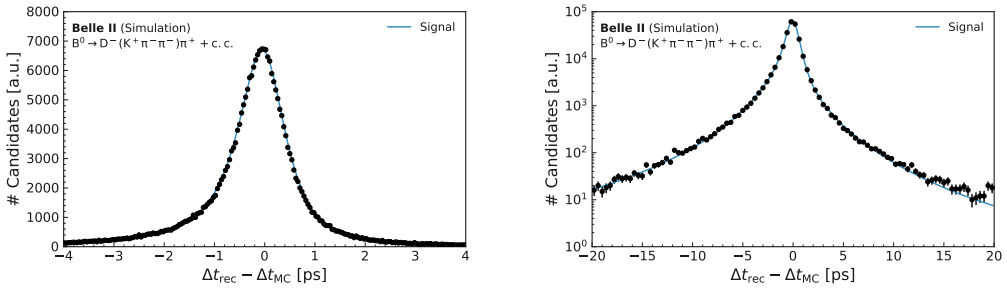

Parameter	Value	Error
μ	-0.1335	0.0084
σ	1.3608	0.0082
c_R	0.231	0.089
c_L	0.2842	0.0057
r_{tail}	0.2608	0.0067
r_R	0.2518	0.0088

Figure 4.21: Top left: Δt_{rec} residual distribution of simulated $B^0 \to D\pi$ signal events shown as black points with error bars. The result of the fit is shown as solid blue line. Top Right: same but in logarithmic scale. Bottom: shape parameters obtained from the fit.

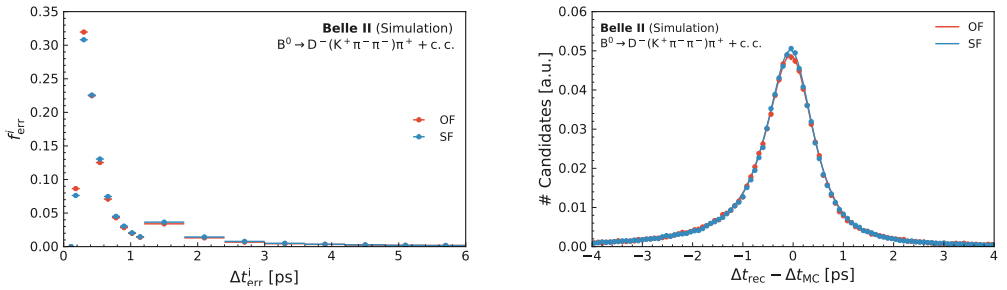

Figure 4.22: Left: fraction of events in bins of Δt_{err} for SF (black dots) and OF (red dots) events in the signal $B^0 \to D\pi$ simulation sample. Right: Δt_{rec} residual distribution for the same events in same colors. The resolution function is also shown as solid line in corresponding color.

4.4.2.4 $B^0 \to D\pi$ background Δt_{rec} shape

The result of the fit to the $\Delta t_{\rm rec}$ distribution of events in the $q\overline{q}$ background simulation $B^0 \to D\pi$ sample is shown in Fig. 4.23. The $q\overline{q}$ background is fitted using only the resolution function, similar to the background study for the $B^0 \to J/\psi\ K_S$ samples. All background populations (SB, SR, SF and OF) in the sample are fitted simultaneously because no significant difference in the $\Delta t_{\rm rec}$ distributions of the different populations is observed.

For the $B\overline{B}$ background the $\Delta t_{\rm rec}$ distribution is wider in the SR than in the SB because the SR contains peaking background while the SB contains only combinatorial background. As discussed in Section 4.1.2, peaking background events have a $\Delta t_{\rm rec}$ distribution similar to signal events while combinatorial background has a narrow $\Delta t_{\rm rec}$ distribution. Therefore, the $\Delta t_{\rm rec}$ distribution in the sideband and signal region are fitted separately. In both regions, the fit proceeds as follows. First, same flavor and opposite flavor events are not separated and the lifetime distribution is fitted with an exponential decay with an effective free-floating lifetime $\tau_{\rm eff}$ convoluted with the resolution functions

$$\exp(\tau_{\rm eff}) * \mathcal{R}. \tag{4.25}$$

All parameters are free floating in that fit except the width of the resolution function σ, which is fixed at 1.35 since otherwise the fit is unstable. The value of 1.35 is chosen since it is close to the value obtained for the signal. Secondly, the $\Delta t_{\rm rec}$ function is fitted simultaneously for the SF and OF samples with the shape of Eq. 4.11. In that second fit, the lifetime and resolution function parameters are fixed to the values found in the lifetime fit, but the effective wrong tag fraction $w_{\rm eff}$ and the effective mixing frequency $\Delta m_{\rm eff}$ of the $B\overline{B}$ background are left free to float. In the final fit for S_f, both parameters are fixed for the $B\overline{B}$ background to the values obtained by these fits. The results of the fits are shown in Fig. 4.24.

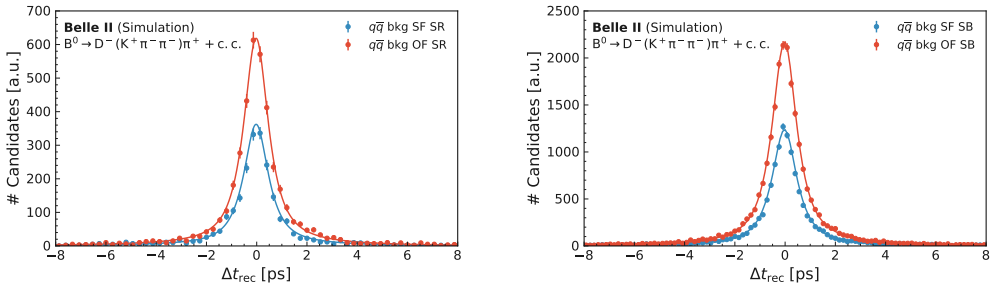

Name	Value	Error
μ	-0.102	0.018
σ	1.464	0.020
c_R	0.199	0.015
c_L	0.137	0.010
r_{tail}	0.203	0.012
r_R	0.565	0.022

Figure 4.23: Top: Δt_{rec} distribution of simulated $q\bar{q}$ background events in the $B^0 \to D\pi$ sample in the SR (Left) and the SB (Right). SF events are depicted in blue and OF events in red. The result of the fit simultaneous to all events is shown as solid line in corresponding color. Bottom: parameters of the fit.

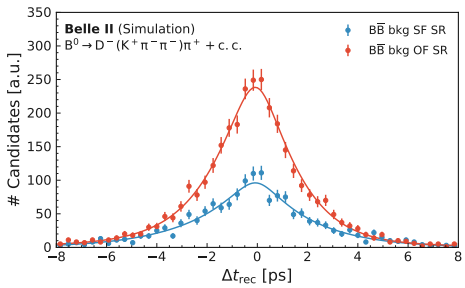

Parameter	Value	Error
μ	-0.159	0.070
σ	1.35	fixed
c_R	0.0060	0.0017
c_L	0.1672	0.0160
r_{tail}	0.157	0.010
r_R	0.426	0.028
τ_{eff}	1.546	0.040
w_{eff}	0.3696	0.0052
Δm_{eff}	0.488	0.031

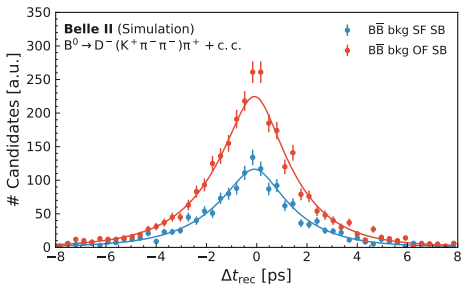

Parameter	Value	Error
μ	-0.188	0.029
σ	1.35	fixed
c_R	0.0084	0.0019
c_L	0.179	0.013
r_{tail}	0.168	0.011
r_R	0.482	0.025
τ_{eff}	1.377	0.039
w_{eff}	0.42569	0.00013
Δm_{eff}	0.02544	0.00023

Figure 4.24: Top Left (Right): Δt_{rec} distribution of simulated $B\overline{B}$ background events for $B^0 \to D\pi$ in the SR (SB). SF events are depicted in blue and OF events in red. The result of a fit simultaneous to all events in the SR (SB) is shown in corresponding colors. Bottom Left (Right): parameters of the fit in the SR (SB).

4.5 Validation of the Fit Using Simulated Events

The extracted shapes and the general fitting procedure are validated by separately fitting the signal simulation samples alone and the combined signal and background simulation samples together. The fit to the $B^0 \to D\pi$ signal sample obtains for the wrong tag fraction a value of $w = 0.2095 \pm 0.0019$. The fit to the $B^0 \to J/\psi(\to \mu^+\mu^-)K_S$ ($B^0 \to J/\psi(\to e^+e^-)K_S$) signal sample obtains for the time dependent CP violation parameter a value of $S_f = 0.6923 \pm 0.0062$ ($S_f = 0.6933 \pm 0.0081$). These values are biased by $\sim 4\%$ compared to the true simulation values (the true values are: $S_f^{\text{truth}} = 0.695$, $w^{\text{truth}}_{B^0 \to J/\psi\ K_S} = 19.22\%$, $w^{\text{truth}}_{B^0 \to D\pi} = 20.12\%$). The values of $w = 0.2057 \pm 0.0062$ and $S_f = 0.735 \pm 0.055$ obtained by the fit to the whole simulation sample are within one standard deviation of the true simulation values. The result of these fits is shown in Section A.1. Furthermore, pseudo-experiments are used to test the stability of the fits and estimate the precision of S_f and the mixing frequency Δm_d as discussed in the following. For the pseudo-experiments, pseudo-datasets are generated by randomly selecting events from the whole simulation samples of the $B^0 \to D\pi$, $B^0 \to J/\psi(\to \mu^+\mu^-)K_S$ and $B^0 \to J/\psi(\to e^+e^-)K_S$ channels. The size of each of the acquired samples corresponds to an integrated luminosity of 30 fb^{-1} of Belle II data, which is approximately the size of the real data sample.

4.5.1 Pseudo-experiments for the precision of S_f

To predict the precision of S_f, 1000 pseudo-datasets corresponding to $B^0 \to J/\psi\ K_S$ and $B^0 \to D\pi$ events are generated. These datasets are fitted with the complete fit planned to be used on the real data. The pull distributions for S_f and w are shown in Fig. 4.25 and are fitted with a Gaussian function. There is no significant bias observed on S_f. The bias on w is $\sim 10\%$ of its statistical uncertainty. For each of these 1000 pseudo-datasets, the statistical significance of the observation of time-dependent CP violation $S_f/\text{err}(S_f)$ is computed. The distribution of the significance is shown in Fig. 4.26. It is ~ 3.1 standard deviations on average.

4.5.2 Pseudo-experiments for the precision of Δm_d

Similiar to what was done for S_f, to estimate the precision of Δm_d 1000 pseudo-datasets corresponding to $B^0 \to D\pi$ events are generated and fitted with the complete fit planned to be used on the real data to extract Δm_d. The pulls on w and Δm_d are shown in Fig. 4.27. The pull on w is similar as what is obtained when Δm_d is fixed. There is however a significant shift on Δm_d, which corresponds to $\sim 25\%$ of its statistical uncertainty. That means that the average value found by the fit is $\Delta m_d \approx 0.514\ ps^{-1}$, biased by 1.5% from the generated value $\Delta m_d^{\text{gen}} = 0.5065\ ps^{-1}$.

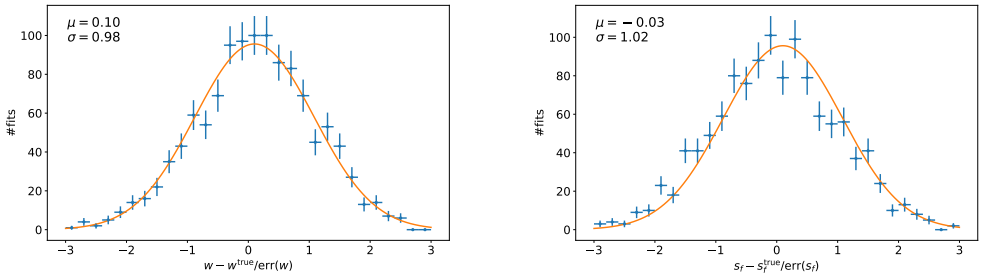

Figure 4.25: Left (Right): Pull distribution of the fit parameters w (S_f) for 1000 complete fits to the $m_{\text{bc}}; \Delta t_{\text{rec}}$ distributions in 1000 pseudo-datasets corresponding to 30 fb^{-1} of $\text{B}^0 \to \text{J}/\psi\ \text{K}_\text{S}$ and $\text{B}^0 \to \text{D}\pi$ data. The pull distributions are fitted with a Gaussian curve shown in orange and its mean and sigma are shown in the top left corner of the figures.

A small bias is expected due to the imperfection of the fitting model. For example the resolution function does not describe the Δt_{rec} residual distribution perfectly as shown in Fig. 4.21.

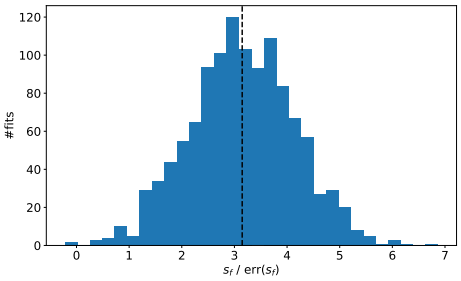

Figure 4.26: Expected statistical significance of the observation of time-dependent CP violation computed for 1000 pseudo-datasets. The black doted line indicates the mean of the distribution.

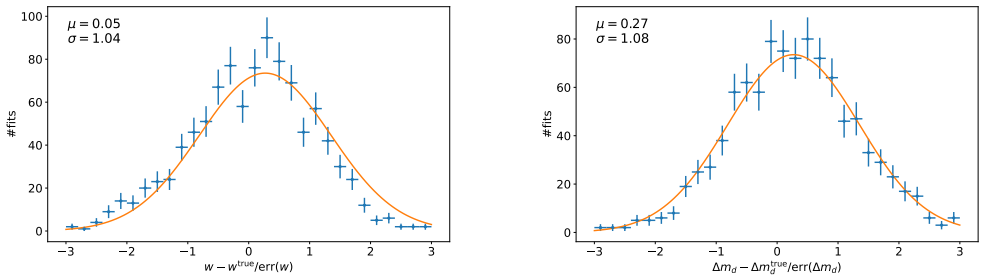

Figure 4.27: Left (Right): Pull distribution of the fit parameters w (Δm_d) for 1000 fits to the $m_{\text{bc}}; \Delta t_{\text{rec}}$ distributions in 1000 pseudo-datasets corresponding to 30 fb^{-1} of $B^0 \to D^- \pi^+$ data. The pull distributions are fitted with a Gaussian curve shown in orange and its mean and sigma are shown in the top left corner of the figures.

4.6 Cross-checks Using the Real Data

In this section, two checks using real data are presented. First, the extracted m_{bc} shapes are used to fit the m_{bc} distribution of the real data. The obtained yields are compared to the yields expected from the simulation. The values of the shift parameter $\Delta_{m_{\mathrm{bc}}}$ for the individual decay channels are also checked. This parameter shifts the m_{bc} shapes to account for imperfect beam energy calibration in the simulation samples. In the final fit, this parameter is free floating and common to all decay channels and m_{bc} shapes. Second, the Δt_{rec} distribution of $\mathrm{B}^0 \to \mathrm{D}\pi$ candidates in the m_{bc} sideband is fitted. It is checked which values for the scale parameter $s_{\Delta \mathrm{t}}$ that scales the width of the resolution function and the shift parameter $\Delta_{\Delta \mathrm{t}}$ that shifts the mean of the resolution function are obtained. Both parameters are introduced to account for possible data simulation discrepancies. In the final fit, both parameters are free floating and common to all Δt_{rec} shapes. Comparisons between the distribution of several variables in the real data and simulation samples can be found in A.5, A.6 and A.7 in the appendix. The agreement between the real data and simulation distributions is very good, given the available statistical precision. This reassures that the m_{bc} and Δt_{rec} shapes extracted using simulation samples can be used to fit the data.

4.6.1 Fit to the m_{bc} shape in the real data

The result of the m_{bc} fits to real data is shown in Fig. 4.28, 4.29 and 4.30. The values and errors of the fit parameters are shown together with the corresponding figures. The obtained signal yields agree with the expectation from the simulation. The shift parameter $\Delta_{m_{\mathrm{bc}}}$ is very small and only for the $\mathrm{B}^0 \to \mathrm{J}/\psi(\to \mu^+\mu^-)\mathrm{K_S}$ sample not compatible with zero. Small shift parameters are expected since the beam energy calibration is not perfect in the simulation.

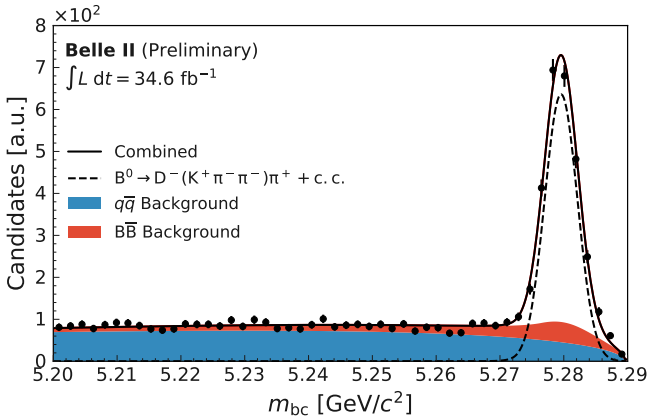

Parameter	Value	Error	Exp.
Signal	2276	54	2269
Background	4096	68	3936
$\Delta_{m_{\mathrm{bc}}}$ [MeV]	0.018	0.065	-

Figure 4.28: Top: fit of the shapes shown in Figure 4.8, 4.10 and 4.9 to the data sample of $B^0 \to D\pi$ (black dots). Bottom: corresponding free fit parameters. Exp. denotes the yield expected from scaling the simulation to data luminosity.

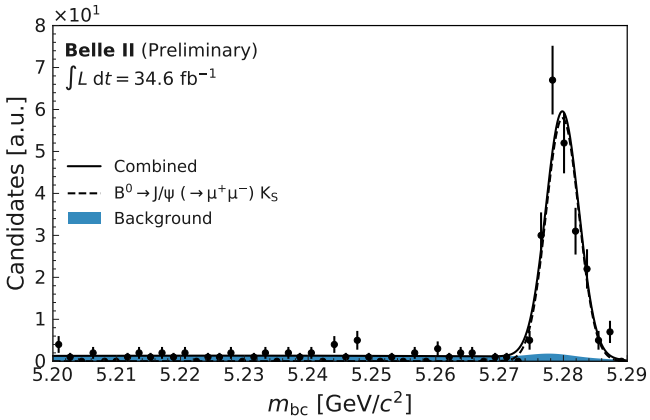

Parameter	Value	Error	Exp.
Signal	208	15	193
Background	63.1	8.7	63.1
$\Delta_{m_{\mathrm{bc}}}$ [MeV]	0.31	0.18	-

Figure 4.29: Top: fit of the shapes shown in Figure 4.13 and 4.14 to the data sample of $B^0 \to J/\psi(\to \mu^+\mu^-)K_S$ (black dots). Bottom: corresponding free fit parameters. Exp. denotes the yield expected from scaling the simulation to data luminosity.

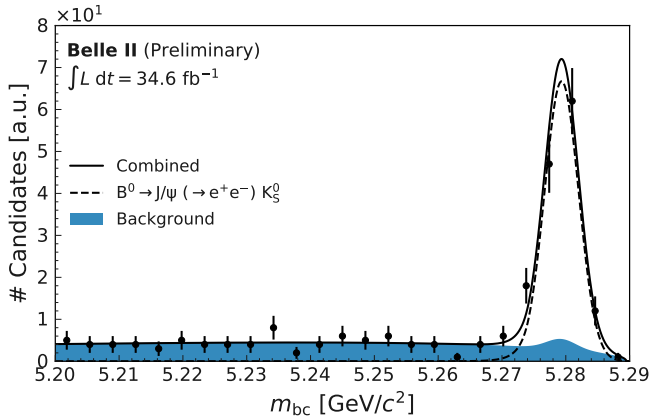

Parameter	Value	Error	Exp.
Signal	125	12	115
Background	102	11	82
$\Delta_{m_{\mathrm{bc}}}$ [MeV]	-0.21	0.26	-

Figure 4.30: Top: fit of the shapes shown in Figure 4.16 and 4.17 to the data sample of $B^0 \to J/\psi(\to e^+e^-)K_S$ (black dots). Bottom: corresponding free fit parameters. Exp. denotes the yield expected from scaling the simulation to data luminosity.

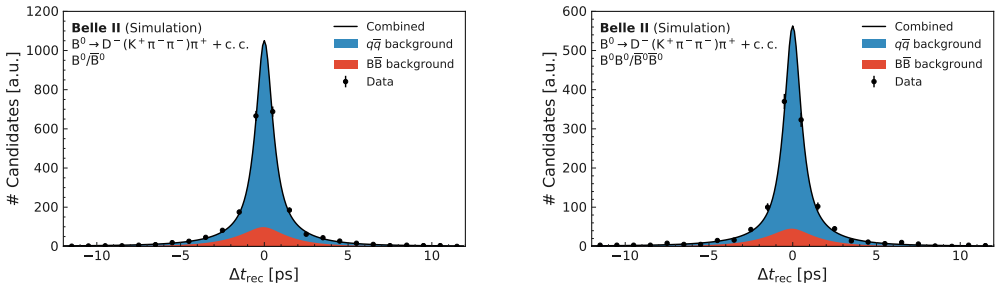

Parameter	Value	Error
$\Delta_{\Delta t}$	0.084	0.041
$s_{\Delta t}$	1.006	0.029

Figure 4.31: Top Left (Right): $\Delta t_{\rm rec}$ distribution for reconstructed $B^0 \to D\pi$ OF (SF) candidates in the SB in the data sample shown as black dots. The total fit is shows as solid black line. The $q\bar{q}$ ($B\overline{B}$) background component of the fit is shows as filled blue (red) area. Bottom: values of errors of the fit parameters.

4.6.2 Fit to the $\Delta t_{\rm rec}$ distribution in the Sideband

The result of the fit to the $\Delta t_{\rm rec}$ distribution of for $B^0 \to D\pi$ candidates in the $m_{\rm bc}$ sideband of the real data is shown in Fig. 4.31. The values and errors of the fit parameters are shown below the fit. The $s_{\Delta t}$ data/simulation correction parameter is compatible with "no correction", but not the $\Delta_{\Delta t}$ parameter.

4.7 Systematic Uncertainties

In Tab. 4.4, the magnitude of the different sources of systematic uncertainty considered in this analysis are shown. The different sources are discussed in the following subsections. The systematic uncertainties are calculated conservatively. Even with this conservative approach, the precision of the measurement is dominated by the statistical uncertainty.

Table 4.4: Summary of the systematic uncertainties. The second column shows the uncertainty for the fit of Δm_d and the third column for the fit of S_f. The given uncertainties denote the relative change on Δm_d and S_f for each source of systematic uncertainty. The last row shows the sum in quadrature of all uncertainties.

Source	Δm_d [%]	S_f [%]
Background scale and shift (Section 4.7.1)	-0.2	-0.3
Peaking Background $B^0 \to J/\psi\ K_S \pm 100\%$ (Section 4.7.2)	•	-2.7
$B\overline{B}$ fraction $\pm 50\%$ in $B^0 \to D\pi$ (Section 4.7.2)	0.03	-2.1
Δm_{eff} for $B\overline{B}$ free (Section 4.7.3)	0.8	0.4
w_{eff} for $B\overline{B}$ free (Section 4.7.3)	-0.15	4.9
w difference between $B^0 \to J/\psi\ K_S$ and $B^0 \to D\pi$ (Section 4.7.4)	•	2.9
Resolution function tail scale (Section 4.7.5)	1.2	0.6
Resolution function tail fraction $\pm 50\%$ (Section 4.7.5)	1.4	0.4
Kinematic approximation w, Δm_d (Section 4.7.6)	1.2	0.0
Kinematic approximation S_f (Section 4.7.6)	•	-0.9
VXD misalignment (Section 4.7.7)	0.4	2.0
total	2.4	7.1

4.7.1 Background Scale and Shift

In the nominal fit, the Δt background shape is fixed to the shape obtained from the simulation. To obtain the systematic uncertainty related to the Δt background shape, a scale factor s_{bkg} and a shift factor Δ_{bkg} is extracted from a fit to the Δt shape in the m_{bc} sideband. The fit is then rerun twice. Once with the background Δt shape scaled and shifted by s_{bkg} and Δ_{bkg} and once with the background shape scaled and shifted by $1/s_{\text{bkg}}$ and $-\Delta_{\text{bkg}}$. The largest deviation of S_f and Δm_d from the nominal fit result is assigned as systematic uncertainty.

4.7.2 $B\overline{B}$ Background Fraction

The fraction of $B\overline{B}$ background events in the $B^0 \to D\pi$ channel has been fixed to the simulation value. To account for data-simulation discrepancies the fraction has been

varied by ±50% in the fit to the data. The difference of the obtained Δm_d and S_f compared to the the result of the nominal fit is assigned as systematic uncertainty related to the $B\overline{B}$ background fraction.
In addition, for the $B^0 \to J/\psi\ K_S$ channel the fit is rerun two times. Once with f_{Gaus} set to 0 and once with f_{Gaus} doubled. The largest deviation of S_f from the nominal fit result is assigned as systematic uncertainty.

4.7.3 Effective Wrong Tag Fraction and Effective Mixing Frequency of the $B\overline{B}$ Background

In the nominal fit, the effective wrong tag fraction w_{eff} and the effective mixing frequency Δm_{eff} for the $B\overline{B}$ background are fixed to the values obtained by the fit to the simulation sample shown in Fig. 4.24. Alternatively, the fit is rerun once with w_{eff} and once with m_{eff} free. The deviations of S_f and Δm_d obtained by these fits from the nominal values are assigned as systematic uncertainty.

4.7.4 Difference in wrong tag fraction between $B^0 \to J/\psi K_S$ and $B^0 \to D^-\pi^+$

The dilution factor 1-2w differs in the simulation by 3.0% between the $B^0 \to D\pi$ channel and the $B^0 \to J/\psi\ K_S$ channels. The difference is assigned as a systematic uncertainty.

4.7.5 Resolution Function Tails

Two systematic uncertainties related to the tails of the resolution function are calculated. First, in the nominal fit the tails are not scaled by s_σ that otherwise scales the width of the resolution function to account for possible data-simulation discrepancies. The fit is rerun with the tails also scaled by s_σ. The difference of the obtained Δm_d and S_f compared to their values in the nominal fit is assigned as a systematic uncertainty.
Second, the fit is repeated with the fraction of the events in the tails varied by ±50%. Again, the difference of the obtained Δm_d and S_f compared to their values in the nominal fit is assigned as a systematic uncertainty.

4.7.6 Kinematic Approximation

The Eq. 4.11 describes only approximately the movement of the Bs in the $\Upsilon(4S)$ rest frame. To estimate the systematic uncertainty related to this approximation, the Δt_{MC} distribution for the $B^0 \to D\pi$ channel is fitted. The deviation of w and Δm_d obtained by the fit and the nominal value is assigned as systematic uncertainty on Δm_d and propagated to S_f. Likewise, the Δt_{MC} distribution for the $B^0 \to J/\psi\ K_S$

channels is also fitted. The deviation of S_f obtained by the fit from the nominal value is assigned as systematic uncertainty on S_f.

4.7.7 VXD alignment

To estimate the systematic uncertainty related to the VXD misalignment, the tracking and reconstruction for simulated $B^0 \to J/\psi\ K_S$ and $B^0 \to D\pi$ events is performed twice. Once using the nominal VXD geometry and once using the misalignment estimated by the Belle II alignment group. The signal resolution function is extracted using the sample with the nominal alignment. This resolution function is then used to perform the fit to extract S_f on both samples with the nominal and misaligned geometry. The values found for S_f are shown in table 4.5. The value of S_f with both geometries are statistically compatible with each other, and compatible with the value found by fitting the centrally produced $B^0 \to J/\psi\ K_S$ simulation sample (Fig. A.2). To be conservative, the 2.6% difference in S_f between the nominal and misaligned geometry is assigned as a systematic uncertainty.

Table 4.5: Results misalignment studies for each channel.

Channel	Name	Nominal		Misalignment		δ_{syst}^{VXD}
		Value	Error	Value	Error	
$B^0 \to J/\psi(\to \mu^+\mu^-)K_S$	S_f	0.687	0.019	0.702	0.019	0.016
$B^0 \to J/\psi(\to e^+e^-)K_S$	S_f	0.672	0.025	0.642	0.024	0.031
$B^0 \to D\pi$	w	0.200	0.006	0.204	0.006	0.004

4.8 Results

B-meson decays into the flavor specific channel $\mathrm{B}^0 \to \mathrm{D}\pi$ are reconstructed and fitted to extract the mixing frequency Δm_d. The fit for Δm_d shown in Fig. 4.32 obtains a value of

$$\Delta m_d = (0.531 \pm 0.046\ (\text{stat.}) \pm 0.013\ (\text{syst.}))\ \text{ps}^{-1}. \tag{4.26}$$

The fit agrees with the world average of $\Delta m_d = (0.5065 \pm 0.0019)\ \text{ps}^{-1}$ [33].

To extract the time dependent CP violation parameter S_f, data samples obtained by reconstructing B-meson decays into the flavor specific channel $\mathrm{B}^0 \to \mathrm{D}\pi$ and into the two CP eigenstates $\mathrm{B}^0 \to \mathrm{J/\psi}(\to \mu^+\mu^-)\mathrm{K_S}$ and $\mathrm{B}^0 \to \mathrm{J/\psi}(\to \mathrm{e}^+\mathrm{e}^-)\mathrm{K_S}$ are fitted simultaneously. Both CP eigenstate channels were chosen because they have a comparatively high branching fraction and a low experimental background. The mixing frequency Δm_d is fixed to the PDG average in the fit for S_f. The fit for S_f shown in Fig. 4.33 obtains a value of

$$S_f = 0.55 \pm 0.21\ (\text{stat.}) \pm 0.04\ (\text{syst.}), \tag{4.27}$$

which is in agreement with the world average of $S_f = 0.691 \pm 0.017$ [33]. Accounting only for the statistical uncertainty, Belle II sees hint of time-dependent CP violation at 2.62σ. The wrong tag fraction obtained by the fit $w = (20.9 \pm 2.1)\%$ agrees with the value of $w = 20.12\%$ expected from the simulation.

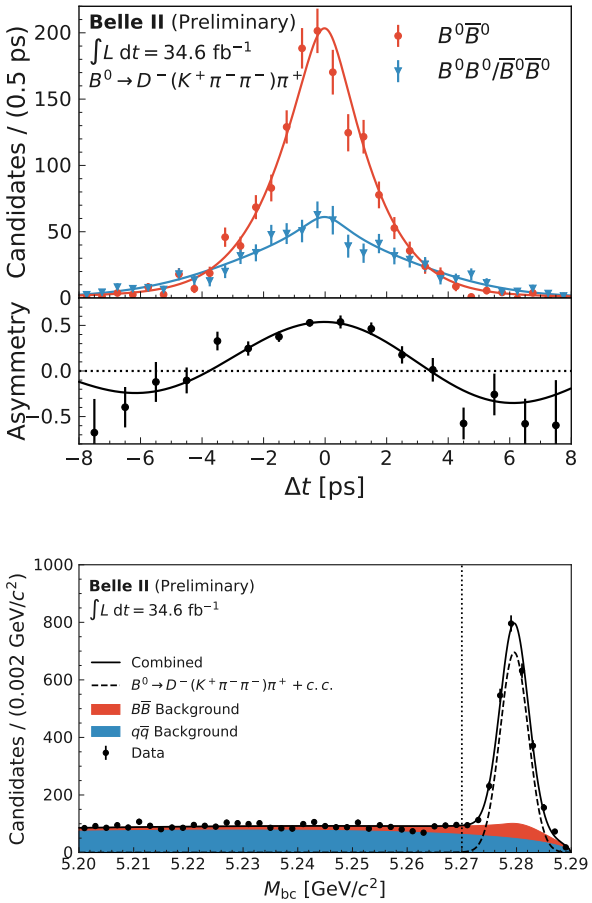

Figure 4.32: Upper top: Δt distribution for reconstructed $\mathrm{B}^0 \to \mathrm{D}\pi$ candidates. The red points show OF events and the blue triangles show SF events. The solid lines in corresponding colors show the result of the fit. The background expectation has been subtracted to display only signal events. Lower top: asymmetry between the number of SF and OF events. The asymmetry is defined as $\frac{N(\mathrm{OF})-N(\mathrm{SF})}{N(\mathrm{OF})+N(\mathrm{SF})}$. The asymmetry obtained from the fit result is superimposed as solid black line. Bottom: m_{bc} distribution for reconstructed $\mathrm{B}^0 \to \mathrm{D}\pi$ candidates (black dots). The total fit is displayed as solid black line. The different components of the fit are shown as dashed black line (signal), filled blue area ($q\overline{q}$ background) and filled red area ($\mathrm{B}\overline{\mathrm{B}}$ background). The vertical dotted line delimits the sideband region (on the left) from the signal region (on the right).

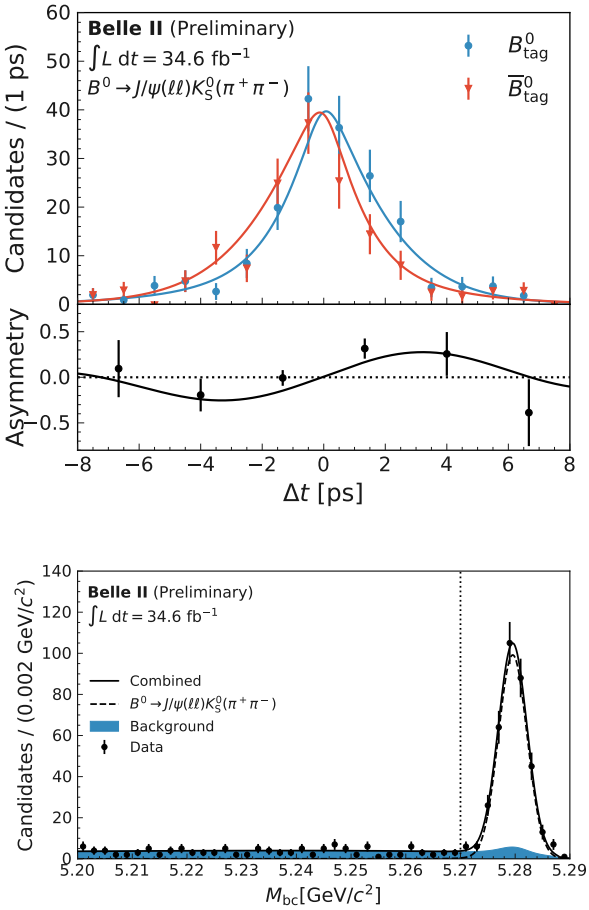

Figure 4.33: Upper top: Δt distribution for reconstructed $B^0 \to J/\psi\ K_S$ candidates. The red triangles show events with a $\overline{B}^0$ tag B and the blue points show events with a B^0 tag B . The solid lines in corresponding colors show the result of the fit. The background expectation has been subtracted to display only signal events. Lower top: asymmetry between the number of events with a tag B^0 and $\overline{B}^0$. The asymmetry is defined as $\frac{N(B^0)-N(\overline{B}^0)}{N(B^0)+N(\overline{B}^0)}$. The asymmetry obtained from the fit result is superimposed as solid black line. Bottom: m_{bc} distribution for reconstructed $B^0 \to J/\psi\ K_S$ candidates (black dots). The total fit is displayed as solid black line. The different components of the fit are shown as dashed black line (signal) and filled blue area (background). The vertical dotted line delimits the sideband region (on the left) from the signal region (on the right).

4.9 Summary

In this analysis, a first measurement of $\sin(2\phi_1)$ of Belle II using a 34.6 fb^{-1} dataset collected at the $\Upsilon(4S)$ resonance with the Belle II detector was performed. For the measurement, two CP eigenstate channel $B^0 \to J/\psi(\to \mu^+\mu^-)K_S$ and $B^0 \to J/\psi(\to e^+e^-)K_S$ as well as one flavor specific channel $B^0 \to D\pi$ were analyzed. The obtained value of

$$\sin(2\phi_1) = 0.55 \pm 0.21 \text{ (stat.)} \pm 0.04 \text{ (syst.)} \tag{4.28}$$

agrees with the world average. Neglecting the statistical uncertainty, Belle II sees hint of time-dependent CP violation at 2.62σ. In addition, the mixing frequency Δm_d has been measured. The measured value

$$\Delta m_d = (0.531 \pm 0.046 \text{ (stat.)} \pm 0.013 \text{ (syst.)}) \text{ ps}^{-1} \tag{4.29}$$

agrees as well with the world average. The primary objective of this analysis was to provide a first measurement of $\sin(2\phi_1)$ in time for ICHEP 2020. Because of time constraints with regards to ICHEP 2020, this analysis was kept as simple as possible. Several physicist contributed to the analysis. I myself contributed to the development of the final selection, extracted the mass background shapes and participated in the verification of the extracted shapes using real data and simulation samples. Going forward, several areas of this analysis need to be improved to provide a precision measurement of $\sin(2\phi_1)$. First, the resolution used in this analysis is a simple sum of Gaussian cores with exponential tails. For a precision measurement, the resolution function needs to be updated. Currently two different resolutions functions are being developed at Belle II, one is based on the resolution function presented in this analysis and modified to incorporate the uncertainty of the vertex position in boost direction. The other is the Belle I resolution function ported to Belle II.
Second, the correction for the motion of the Bs in the $\Upsilon(4S)$ can be improved.
Third, due to differences in the calibration of the beam spot between data and simulation, for the fitting of the B^0_{sig} and B^0_{tag} vertices no beam spot constrained has been applied. A new beam spot calibration has already been developed at Belle II and is currently validated. The inclusion of beam spot constraints will improve the precision of the fit of the vertices. In addition, TreeFitter is improved to be able to not only fit the B^0_{sig} decay, but the whole $\Upsilon(4S) \to B^0_{\text{sig}}B^0_{\text{tag}}$ decay chain.
Forth, the analysis was minimal in the number of analyzed CP-eigenstate and flavor specific channels. Work is already ongoing to include more channels.
Fifth, the analysis has not been binned in bins of the flavor tagger quality r due to time constraints, as the dependency of the resolution function on r needs to be studied. Performing the analysis in bins of r will increase the precision.

Chapter 5

Summary and Conclusion

The first generation B-flavor factories BaBar and Belle provided precision measurements of various parameters of the SM. Among other things, they helped to solidify our current understanding of CP violation which arises from a complex phase in the CKM matrix in the Standard Model. As a next-generation B-flavor factory, the Belle II experiment is the successor of BaBar and Belle. One of its main goals is the precision measurement of the size of the sides and angles of the unitary triangle associated to B-meson decays. Possible non-closure of the triangle would provide a hint for physics beyond the Standard Model. In this thesis, two analyses using data taken by the Belle II experiment until June 2020 were presented.

In the first analysis, radiative Bhabha events are used in a tag and probe approach to measure the electron identification efficiency of the Belle II detector. The efficiency is measured using different data and simulation samples which became available at different times. The analysis shows adequate performance of the electron identification of Belle II and that its efficiency is increasing over time. Analysts working at Belle II can use the ratio between the electron identification efficiency calculated using data and simulation samples to account for data-simulation discrepancies. The study will be repeated as soon as new data or simulation samples become available. To ensure that the analysis can also be carried out in the future, a high level trigger line suitable for the analysis and its impact on the electron identification efficiency is presented. This high level trigger line is currently not part of the analysis but will be needed in future since the high level trigger system of Belle II switched from monitoring into filtering mode in autumn 2020.

In the second analysis presented in this thesis, the time dependent CP violation parameter $\sin(2\phi_1)$ and the mixing frequency in the system of neutral B-mesons Δm_d is measured using a 34.6 fb^{-1} dataset collected at the $\Upsilon(4S)$ resonance with the Belle II detector. This analysis is the joint work of a larger team within the Belle II collaboration. The author has contributed in several areas, namely the extraction of mass background shapes, the development of the final selection and the verification of the extracted shapes using real data and simulation samples. In this analysis, decays into the flavor eigenstate $\text{B}^0 \to \text{D}\pi$ and the CP eigenstates $\text{B}^0 \to \text{J}/\psi(\to \mu^+\mu^-)\text{K}_\text{S}$ and $\text{B}^0 \to \text{J}/\psi(\to \text{e}^+\text{e}^-)\text{K}_\text{S}$ are reconstructed. Subsequently, $\sin(2\phi_1)$ and Δm_d are

extracted by performing fits to the obtained data samples. The obtained values of

$$\sin(2\phi_1) = 0.55 \pm 0.21 \text{ (stat.)} \pm 0.04 \text{ (syst.)} \tag{5.1}$$

and

$$\Delta m_d = (0.531 \pm 0.046 \text{ (stat.)} \pm 0.013 \text{ (syst.)}) \text{ ps}^{-1} \tag{5.2}$$

agree with the world average. Although this analysis does not yet provide a precision measurement due to the small data set and its simple approach, it shows that Belle II is well prepared to perform precision measurements in the future and to achieve its physics goals. In Section 4.9, the necessary steps to transform this analysis into a precision analysis are discussed.

In conclusion, this thesis provides a measurement of the efficiency of the electron identification of the Belle II detector, showing its adequate performance. In addition, a first measurement of the time dependent CP violation parameter $\sin(2\phi_1)$ and the mixing frequency in the system of neutral B-mesons Δm_d using Belle II data has been presented. Currently, this analysis is limited by the statistical uncertainty. The Belle II collaboration aims to record 50 ab^{-1} of data by 2025. This amount of data allows to measure $\sin(2\phi_1)$ and Δm_d with a precision of better than 1%. Consequently, measurements with Belle II data will be able to provide stringent constraints on the CKM parameters of the Standard Model. The analysis presented in this thesis provides the foundation to perform these precision measurements.

Bibliography

1. Wikipedia. Standard Model. *Wikipedia, The Free Encyclopedia.* [Online; accessed 14-December-2020] (2020).
2. Charles, J. *et al.* CP violation and the CKM matrix: assessing the impact of the asymmetric B factories. *The European Physical Journal C* **41,** 1–131. ISSN: 1434-6052 (May 2005).
3. CERN. The Standard Model. *Cern Webpage.* [Online; accessed 24-December-2020] (2020).
4. Altarelli, G. & Wells, J. *Gauge Theories and the Standard Model* ISBN: 978-3-319-51920-3. doi:10.1007/978-3-319-51920-3_1. https://doi.org/10.1007/978-3-319-51920-3_1 (Springer International Publishing, Cham, 2017).
5. Kuhr, T. *Flavor physics at the Tevatron* doi:10.1007/978-3-642-10300-1 (2013).
6. Chau, L.-L. & Keung, W.-Y. Comments on the Parametrization of the Kobayashi-Maskawa Matrix. *Phys. Rev. Lett.* **53,** 1802–1805 (19 Nov. 1984).
7. Zyla, P. *et al.* Review of Particle Physics. *PTEP* **2020,** 083C01 (2020).
8. Cabibbo, N. Unitary Symmetry and Leptonic Decays. *Phys. Rev. Lett.* **10,** 531–533 (12 June 1963).
9. Christenson, J., Cronin, J., Fitch, V. & Turlay, R. Evidence for the 2π Decay of the K_2^0 Meson. *Phys. Rev. Lett.* **13,** 138–140 (1964).
10. Kobayashi, M. & Maskawa, T. CP-Violation in the Renormalizable Theory of Weak Interaction. *Progress of Theoretical Physics* **49,** 652–657. ISSN: 0033-068X (Feb. 1973).
11. Wolfenstein, L. Parametrization of the Kobayashi-Maskawa Matrix. *Phys. Rev. Lett.* **51,** 1945–1947 (21 Nov. 1983).
12. Carter, A. B. & Sanda, A. I. CP violation in B-meson decays. *Phys. Rev. D* **23,** 1567–1579 (7 Apr. 1981).
13. Michel Hernandez Villanueva. Prospects for tau lepton physics at Belle II. *Proceedings of the 15th International Workshop on Tau Lepton Physics (TAU2018)* (Feb. 2019).

14. BaBar Collaboration. Letter of intent for the study of CP violation and heavy flavor physics at PEP-II. doi:10.2172/10171297. https://www.osti.gov/biblio/10171297 (June 1994).

15. Cheng, M. *et al.* Letter of intent for a study of CP violation in B meson decays. *KEK Report 94-2* (Apr. 1994).

16. Brodzicka, J. *et al.* Physics Achievements from the Belle Experiment. *PTEP* **2012,** 04D001 (2012).

17. Kou, E. *et al.* The Belle II Physics Book. *Progress of Theoretical and Experimental Physics* **2019.** ISSN: 2050-3911. doi:10.1093/ptep/ptz106. http://dx.doi.org/10.1093/ptep/ptz106 (Dec. 2019).

18. Abe, T. *et al.* Belle II Technical Design Report. arXiv: 1011.0352 [physics.ins-det] (Nov. 2010).

19. Akai, K., Furukawa, K. & Koiso, H. SuperKEKB collider. *Nuclear Instruments and Methods in Physics Research Section A: Accelerators, Spectrometers, Detectors and Associated Equipment* **907,** 188–199. ISSN: 0168-9002 (Nov. 2018).

20. Matvienko, D. The Belle II experiment: status and physics program. *EPJ Web of Conferences* **191,** 02010 (Jan. 2018).

21. Hara, T., Kuhr, T. & Ushiroda, Y. Belle II Coordinate System and Guideline of Belle II Numbering Scheme. *Internal Belle II Document Server.* https://docs.belle2.org/record/242?ln=en (Aug. 2011).

22. Schieck, J. DEPFET pixels as a vertex detector for the Belle II experiment. *Nuclear Instruments and Methods in Physics Research Section A: Accelerators, Spectrometers, Detectors and Associated Equipment* **732,** 160–163. ISSN: 0168-9002 (Dec. 2013).

23. Abashian, A. *et al.* The Belle detector. *Nuclear Instruments and Methods in Physics Research Section A: Accelerators, Spectrometers, Detectors and Associated Equipment* **479.** Detectors for Asymmetric B-factories, 117–232. ISSN: 0168-9002 (2002).

24. Fruhwirth, R. Application of Kalman filtering to track and vertex fitting. *Nucl. Instrum. Meth. A* **262,** 444–450 (1987).

25. Waltenberger, W. RAVE—A Detector-Independent Toolkit to Reconstruct Vertices. *IEEE Transactions on Nuclear Science* **58,** 434–444 (2011).

26. Krohn, J.-F. *et al.* Global decay chain vertex fitting at Belle II. *Nuclear Instruments and Methods in Physics Research Section A: Accelerators, Spectrometers, Detectors and Associated Equipment* **976,** 164269. ISSN: 0168-9002 (Oct. 2020).

27. Belle II Collaboration. First flavor tagging calibration using 2019 Belle II data. arXiv: 2008.02707 [hep-ex] (2020).

28. Abudinén, F. Development of a B^0 flavor tagger and performance study of a novel time-dependent CP analysis of the decay $B^0 \to \pi^0\pi^0$ at Belle II. *Ludwig-Maximilians-Universität München.* http://nbn-resolving.de/urn:nbn:de:bvb:19-230032 (Oct. 2018).

29. The Belle II collaboration. Muon and electron identification efficiencies and hadron-lepton mis-identification probabilities. *Belle II Document Server.* https://docs.belle2.org/record/2062?ln=en (July 2020).

30. Kraetzschmar, T. M. G., Skorupa, J. & Humair, T. Bhabha Lepton Identification Study with Early Phase 3 Data. *Internal Belle II Document Server.* https://docs.belle2.org/record/1500?ln=en (June 2019).

31. Chekelian, V., Humair, T., Kandra, J., Skorupa, J. & Zlebcik, R. Prompt $B^0 \to J/\psi K_S$ analysis. *Internal Belle II Document Server.* https://docs.belle2.org/record/1957?ln=en (June 2020).

32. Bevan, A. J. *et al.* The Physics of the B Factories. *The European Physical Journal C* **74.** ISSN: 1434-6052. doi:10.1140/epjc/s10052-014-3026-9. http://dx.doi.org/10.1140/epjc/s10052-014-3026-9 (Nov. 2014).

33. Tanabashi, M. *et al.* Review of Particle Physics. *Phys. Rev. D* **98,** 030001 (2018).

34. Karbach, T. M., Raven, G. & Schiller, M. Decay time integrals in neutral meson mixing and their efficient evaluation. arXiv: 1407.0748 [physics.data-an] (July 2014).

35. Oeftiger, A. *et al.* Review of CPU and GPU Faddeeva Implementations. *7th International Particle Accelerator Conference,* WEPOY044 (2016).

36. Fox, G. C. & Wolfram, S. Event shapes in e+e- annihilation. *Nuclear Physics B* **149,** 413–496. ISSN: 0550-3213 (1979).

37. Gaiser, J. E. Charmonium Spectroscopy From Radiative Decays of the J/ψ and ψ'. *SLAC Stanford - SLAC-255 (82,REC.JUN.83) 194p* (Aug. 1982).

38. Albrecht, H. *et al.* Search for hadronic b→ u decays. *Physics Letters B* **241,** 278–282. ISSN: 0370-2693 (1990).

Appendix A

Prompt $B^0 \to J/\psi\ K_S$ analysis

In this chapter, fit check and data/simulation comparison plots of the prompt $B^0 \to J/\psi\ K_S$ analysis are shown.

A.1 Check of the Fit using Simulated Events

In this section, plots showing the result of the fit to the whole simulation sample are shown. The plots provide additional information for Section 4.5.

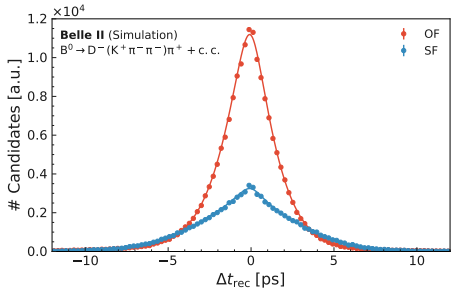

Parameter	Value	Error
$\Delta_{\Delta t_{\mathrm{rec}}}$	0.0070	0.0089
$s_{\Delta t_{\mathrm{rec}}}$	0.9203	0.0071
w	0.2095	0.0019

Figure A.1: Left: Δt_{rec} distribution for signal $B^0 \to D\pi$ SF (blue points) and OF (red point) simulated events. The result of the fit is shown with the solid line in the corresponding colour. Right: values and errors of the fit parameters.

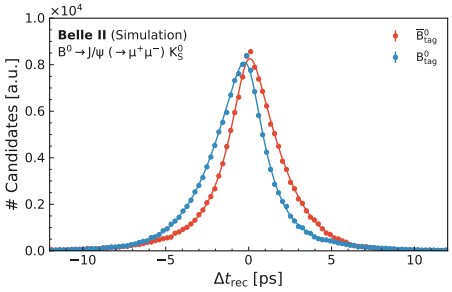

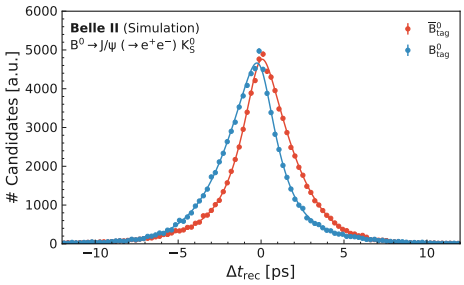

Parameter	Value	Error
$\Delta_{\Delta t_{\mathrm{rec}}}$	0.0101	0.0093
$s_{\Delta t_{\mathrm{rec}}}$	0.9600	0.0080
S_f	0.6923	0.0062

Parameter	Value	Error
$\Delta_{\Delta t_{\mathrm{rec}}}$	0.009	0.012
$s_{\Delta t_{\mathrm{rec}}}$	0.943	0.010
S_f	0.6933	0.0081

Figure A.2: Top Left (Top Right): Δt_{rec} distribution for signal $\mathrm{B^0 \to J/\psi(\to \mu^+\mu^-)K_S}$ ($\mathrm{B^0 \to J/\psi(\to e^+e^-)K_S}$) simulated events. The distribution of positive flavor events is shown as blue points with error bars and the distribution of negative flavor events as red points with errorbars. The result of the fit is shown with the solid line in the corresponding colour. Bottom Left (Right): values and errors of the fit parameters corresponding to the fit shown above.

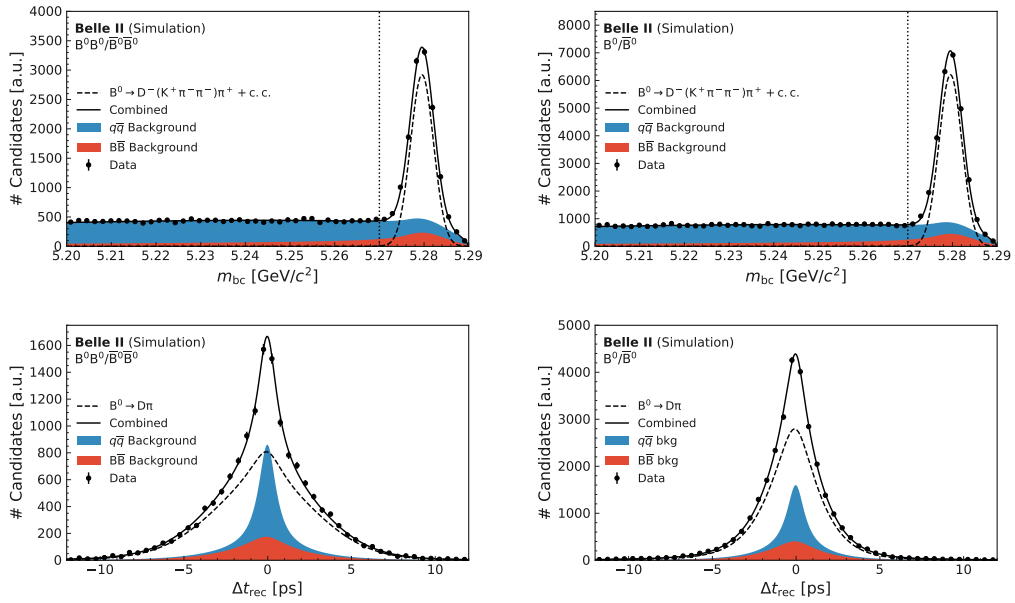

Figure A.3: Top Left (Right): m_{bc} distribution of reconstructed $\mathrm{B}^0 \to \mathrm{D}\pi$ SF (OF) candidates in the $\mathrm{B}^0 \to \mathrm{D}\pi$ simulation sample shown as black dots. The total fit is shown as a solid black line. The different components of the fit are shown as dashed line (signal), filled blue area ($q\overline{q}$ background) and filled red area ($\mathrm{B}\overline{\mathrm{B}}$ background). The vertical line delimits the SB (on the left) from the SR (on the right). Bottom Left (Right): Δt_{rec} distribution for SF (OF) candidates belonging to the SR $m_{\mathrm{bc}} > 5.27$ GeV shown as black dots. The total fit is shown as a solid black line. The different components of the fit are shown as dashed line (signal), filled blue area ($q\overline{q}$ background) and filled red area ($\mathrm{B}\overline{\mathrm{B}}$ background).

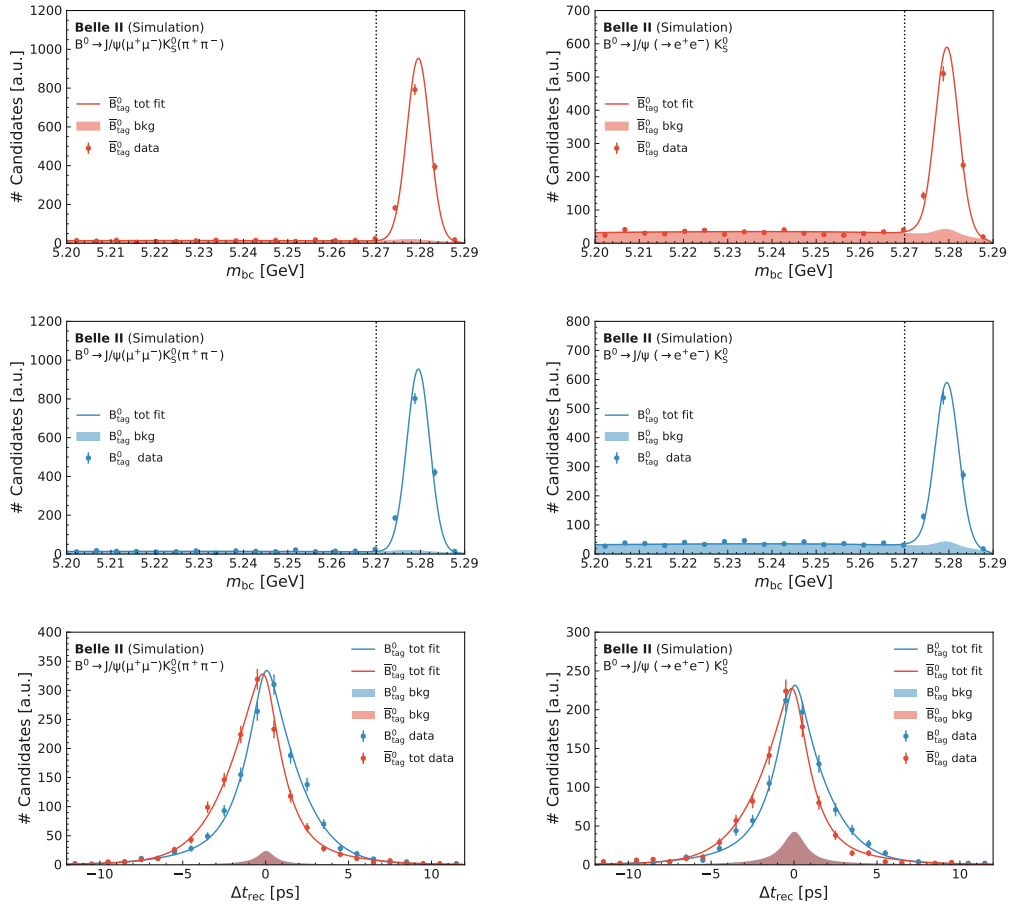

Figure A.4: Left (Right): m_{bc} and Δt_{rec} distribution of reconstructed $\mathrm{B^0 \to J/\psi(\to \mu^+\mu^-)K_S}$ ($\mathrm{B^0 \to J/\psi(\to e^+e^-)K_S}$) candidates in the $\mathrm{B^0 \to J/\psi(\to \mu^+\mu^-)K_S}$ ($\mathrm{B^0 \to J/\psi(\to e^+e^-)K_S}$) simulation. Top (Middle): m_{bc} distribution of reconstructed $\mathrm{B^0 \to J/\psi(\ell\ell)K_S}$ negative (positive) flavor events shown as red (blue) dots. The result of the total fit is shows as solid red (blue) line. The background component is shown as filled red (blue) area. The vertical line delimits the SB (on the left) from the SR (on the right). Bottom: Δt_{rec} distribution of reconstructed $\mathrm{B^0 \to J/\psi(\ell\ell)K_S}$ candidates shown as red (blue) dots for reconstructed negative (positive) flavor events. The result of the total fit for negative (positive) flavor events is shown as solid red (blue). The background component is shown as filled red (blue) area.

Table A.1: Obtained values and errors for the parameter of the simultaneous fit to $B^0 \to J/\psi\ K_S$ and $B^0 \to D\pi$ simulation samples.

Parameter	Value	Error
$N_{\rm sig}(B^0 \to J/\psi(\to \mu^+\mu^-)K_S)$	1345	26
$N_{\rm bkg}(B^0 \to J/\psi(\to \mu^+\mu^-)K_S)$	259	13
$N_{\rm sig}(B^0 \to J/\psi(\to e^+e^-)K_S)$	821	22
$N_{\rm bkg}(B^0 \to J/\psi(\to e^+e^-)K_S)$	640	19
$N^{\rm SF}_{\rm sig}(B^0 \to D\pi)$	10440	120
$N^{\rm OF}_{\rm sig}(B^0 \to D\pi)$	22190	170
$N^{\rm SF}_{\rm bkg}(B^0 \to D\pi)$	20950	160
$N^{\rm OF}_{\rm bkg}(B^0 \to D\pi)$	37470	210

Parameter	Value	Error
w	0.2057	0.0062
S_f	0.735	0.055
$\Delta_{\Delta t_{\rm rec}}$	0.013	0.027
$s_{\Delta t_{\rm rec}}$	0.949	0.023
$\Delta_{m_{\rm bc}}$ [MeV]	-0.003	0.017

A.2 Data/Simulation Comparison Plots

In this section, plots showing the distribution of several variables in the real data and simulation samples of the prompt $B^0 \to J/\psi K_S$ analysis are presented. The plots provide additional information for Section 4.6.

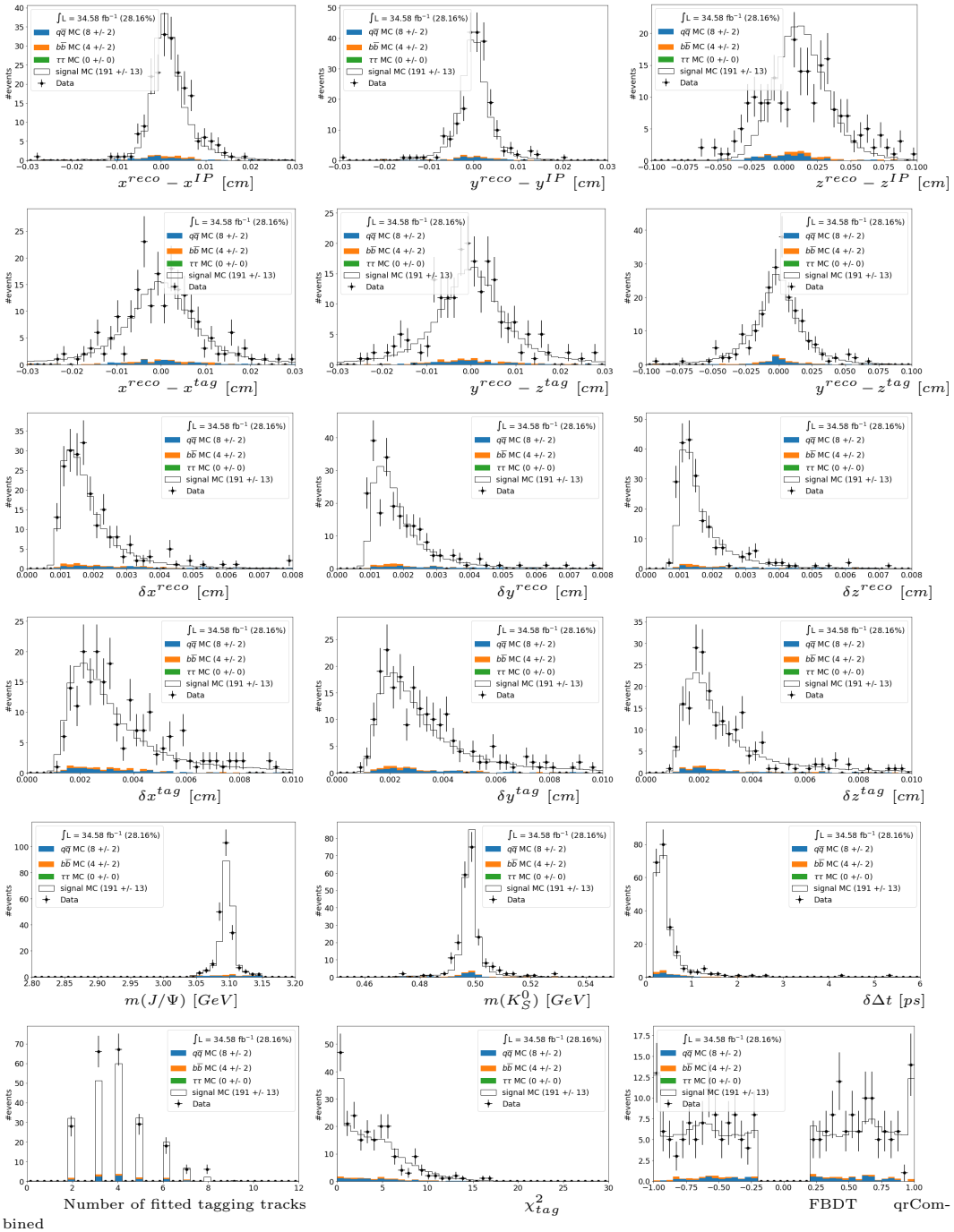

Figure A.5: Distribution of several variables after selection for the $B^0 \to J/\psi(\to \mu^+\mu^-)K_S$ channel for the real data and simulation samples.

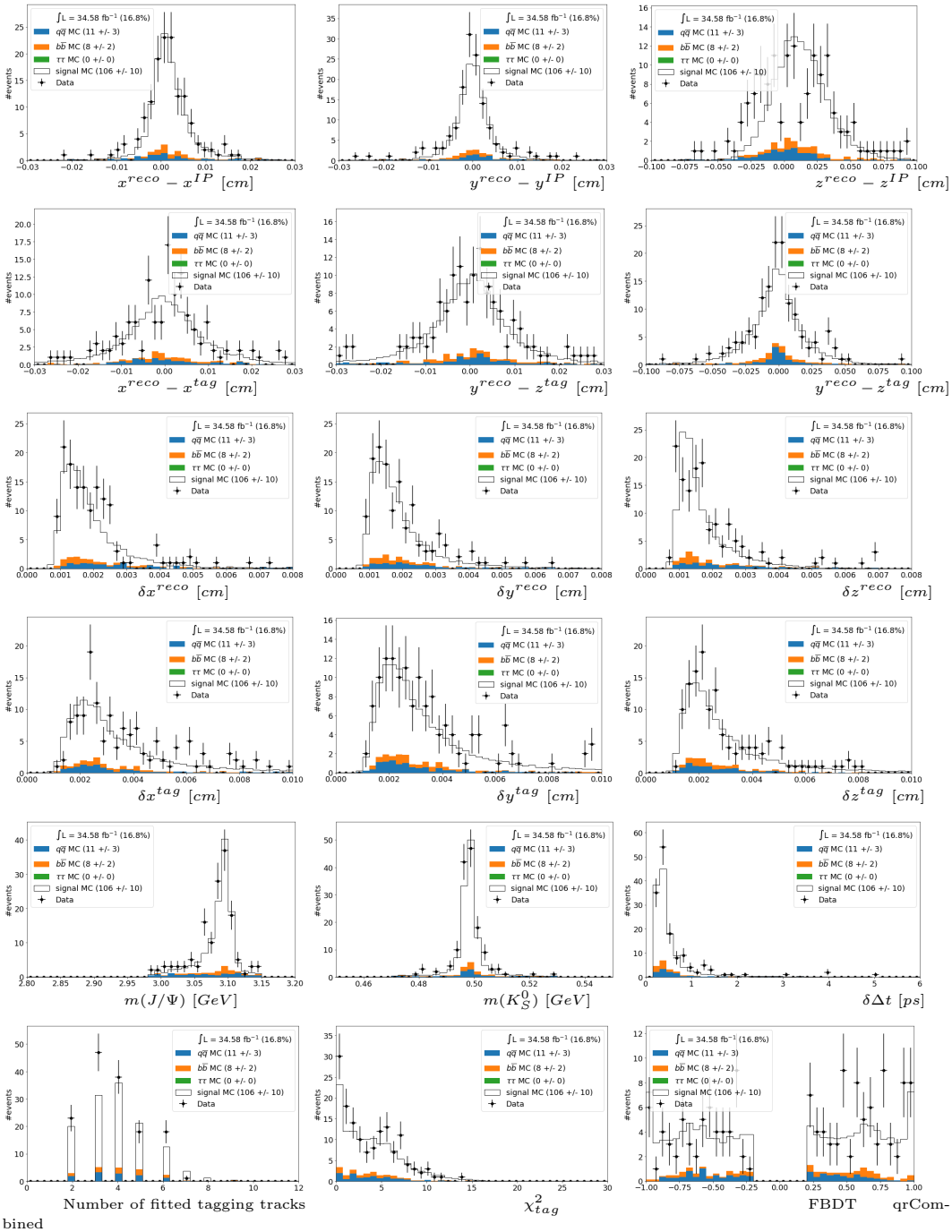

Figure A.6: Distribution of several variables after selection for the $B^0 \to J/\psi(\to e^+e^-)K_S$ channel for the real data and simulation samples.

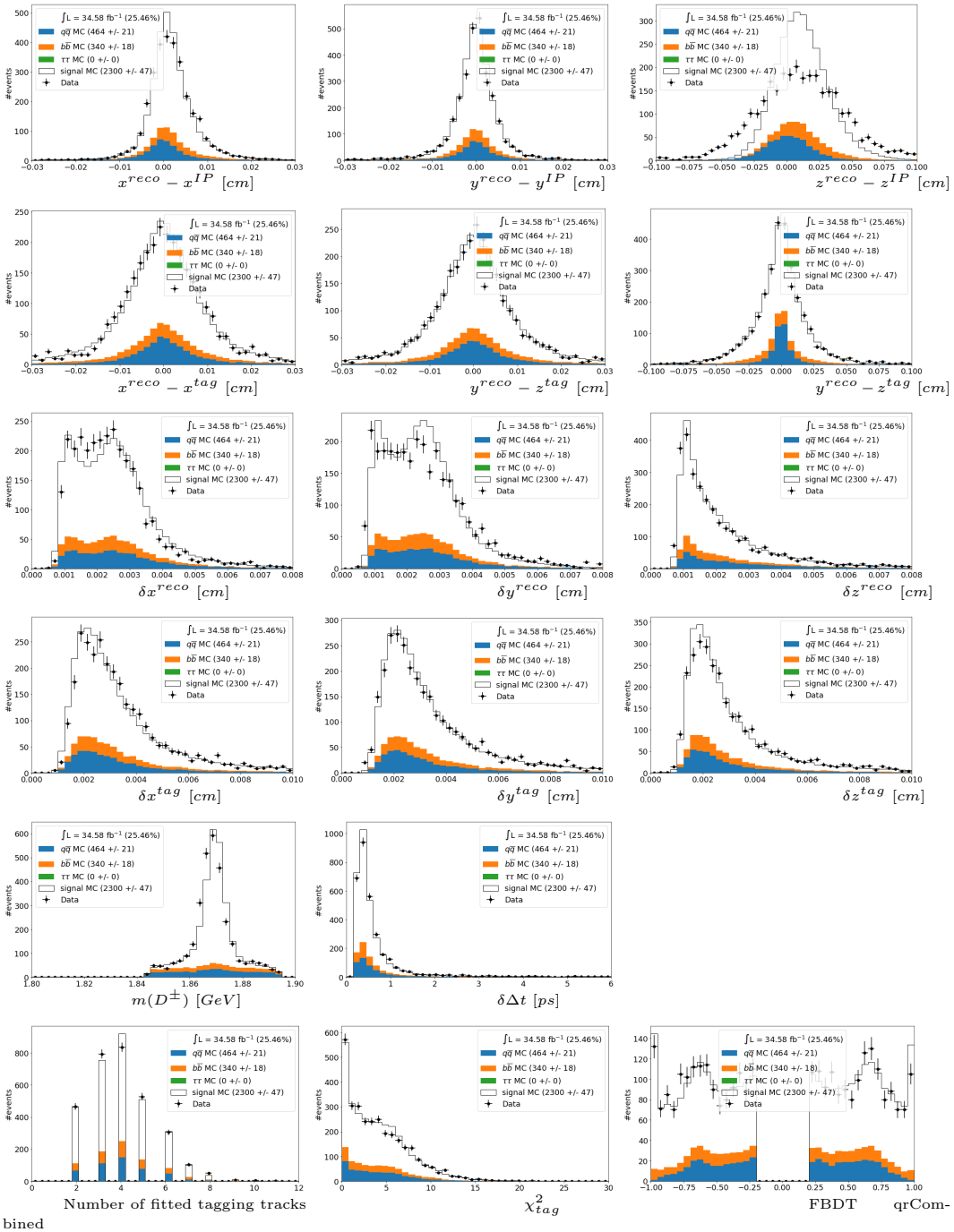

Figure A.7: Distribution of several variables after selection for the $B^0 \to D\pi$ channel for the real data and simulation samples.

Acknowledgments

I thank everyone who helped me during development of the presented analyses and writing of my thesis.

I particularly want to thank Frank Simon for introducing me to the Belle II experiment, welcoming me into into the Future Detector group at the MPP and his supervision. I also want to thank Hans-Günther Moser for welcoming me into the Belle II group at the MPP and his help and advise. I thank Allen Caldwell for agreeing to be my supervising professor.

In addition, I want to thank every member of the Future Detector and Belle II group for the lively discussions and the great time at the Institute. I especially thank Thomas Kraetzschmar for his supervision during the study of the electron identification efficiency. I also want to thank Thibaud Humair for introducing me to the wonderful world of time dependent CP violation and for his patience in answering countless of my questions.